Dissertation

submitted to the

Combined Faculties for the Natural Sciences and for Mathematics

of the Ruperto-Carola University of Heidelberg, Germany

for the degree of

Doctor of Natural Sciences

presented by

Diplom Physiker Diethard Peter

born Trier, Germany

Oral examination: 12 November 2008

Massive Star Formation at High Angular Resolution

Pyramid Wavefront Sensing and the Search for Massive Binaries

Referees:	Prof. Dr. Thomas Henning
	Prof. Dr. Andreas Quirrenbach

Zusammenfassung

Anders als bei Sternen niedriger Massen ist die Entstehung von Sternen mit Massen oberhalb von $10M_\odot$ noch nicht geklärt. Die Gründe sind, daß diese Sterne tief in Staub eigebettet, im allgemeinen weit entfernt ($\geq$ 1kpc) und äußerst selten sind.

Eine Möglichkeit die Entstehung massereicher Sterne zu entschlüsseln, liegt darin, die Parameter massereicher Doppel- und Mehrfachsysteme zu untersuchen, da diese Parameter Informationen über den Entstehungsmechanismus enthalten.

Um dieses Projekt durchzuführen, braucht man Aufnahmen hoher Winkelauflösung wie sie z.B. mit Hilfe adaptiver Optik erzielt werden können. Zu deren Verbesserung wurde der im Infraroten arbeitende Pyramiden Wellenfront Sensor PYRAMIR entwickelt. Es konnte gezeigt werden, daß dieser Sensor eine Verbesserung gegenüber dem konventionellen Shack-Hartmann Sensor darstellt. Das Instrument konnte leider wegen technischer Schwierigkeiten nicht für unsere Zwecke eingesetzt werden.

Stattdessen wurden mittels Lucky Imaging 150 Targets in den Cep OB2 und OB3 Assoziationen beobachtet. Das aus den Daten abgeleitete Entstehungsszenario zeigt einen ursprünglich weiten, massearmen Doppelstern der durch Akkretion zu einem engen massereicheren heranwächst. Es ergeben sich große Unterschiede zwischen Sternen leichter und schwerer als $10M_\odot$ in Zahl und Masse der Begleiter. Dieser Befund bestätigt Resultate aus anderen Sternentstehungsgebieten.

Abstract

In contrast to the situation for low-mass stars, the formation mechanism of massive stars i.e. stars with masses of $\geq 10\ M_\odot$ is still unclear. The reason is that these stars are highly embedded, on average far away ($\geq$ 1 kpc) and much rarer than their low-mass brothers.

One way to approach the matter of massive star formation is to look at the binary parameters as imprints of the formation process.

In order to provide sufficiently high angular resolution the pyramid infrared wavefront sensor PYRAMIR has been developed. The commissioning showed that in principle this sensor is superior over the conventional Shack-Hartmann sensor. However technical peculiarities of the system made it not suitable for our observational campaign.

In stead we used Lucky imaging to observe 150 targets in the Cep OB2/3 associations at high angular resolution.

The data implies a scenario in which accretion processes transform an originally wide binary into a close one. We detected a strong difference in the number and the masses of the companions between stars on both sides of a border of 10 $M_\odot$. This result confirms previous findings in different star forming regions.

Contents

Chapter 1

Introduction

Massive stars are the primary source of heavy elements. They produce elements up to iron within their cores and feed them into the ISM by their strong winds. Even heavier elements are produced through neutron capture processes during the supernova explosion that ends the life of the object as a massive star leaving behind a neutron star or a black hole. These heavy elements are important for the formation of planets and, finally, for life. Their impact on their surroundings makes the massive stars a key issue in the formation and evolution of galaxies.

The regime of massive stars ranges from a lower mass between 8 $M_\odot$ and 10 $M_\odot$, to the most massive stars found up to date like the Pistol star of $\approx$ 100 $M_\odot$. These stars don't have a pre-main sequence (PMS) phase i.e. accretion does not stop before they start to burn Hydrogen. The surface temperature of such massive stars can reach up to 50 000K, their luminosities reach up to 10^6 times the luminosity of our sun. Their strong UV-flux dissociates the dust in the surrounding interstellar medium (ISM) and ionizes hydrogen, building HII regions.

To understand the formation of stars is one of the fundamental tasks of astronomy. On the side of low-mass stars there exists a standard model of the formation process (Shu et al. 1987). However the model of star formation proposed there cannot directly be applied to massive star formation. The main reason is the property mentioned in the beginning: a large photon flux that can prevent further infall and potentially stop the formation at masses of $\approx$ 10 $M_\odot$ (Wolfire & Cassinelli 1987).

The current theory of massive star formation follows two lines. One line is a modified version of low-mass star formation the other line is based on the fact that massive stars usually form within the dense cores of stellar clusters where dynamical interactions between stars take place. The two main ingredients of the first approach are: 1. accretion rates higher, i.e., $\approx 10^{-3}$ $M_\odot\,a^{-1}$ than the value of 10^{-6} $M_\odot\,a^{-1}$ found in low-mass star forming regions . This value can be reached taking turbulence and high pressure present in massive star forming regions (McKee & Tan 2002,2003). Even higher values have been observed in Orion by Nakano et al. (2000). 2. Nonspherical accretion. Calculations by Yorke & Bodenheimer (1999) and Yorke & Sonnhalter (2002) for example show that the formation of an accretion disk induces a nonisotropic distribution of the stellar radiative flux. The radiative acceleration is concentrated toward the poles and the radiation pressure on the accretion disc above the equator is reduced.

Both effects together can result in a self-shielding of the accretion disk (Jijina & Adams 1996) allowing matter to flow further onto the surface of the star.

The starting point of the second approach is that massive stars near the center of star clusters are at the bottom of the gravitational potential well. There they are fed matter from the entire

cluster rather than their nearest environment only. In this scenario massive stars are the product of collisions between two or more intermediate-mass stars (Bonnell et al. 2005). A prediction of this hypothesis is that massive stars harbor a large fraction of close companions (failed mergers) potentially with another wide low-mass companion. An important condition for this scenario are stellar densities of $\approx 10^6\,pc^{-3}$ as observed in the centers of stellar clusters.
The fact that the second line of theory predicts a high rate of multiplicity for massive stars is a handle to distinguish between the two scenarios. In fact there exist various models of the formation of the binary systems themselves.
The easiest model to come up with, is probably the capture of a previously unbound object by the primary star. Another category of models can be described as results of the fragmentation of the cloud core, i.e., as bound systems from the very beginning. The properties of the result depend on the number of fragments into that the core splits. These fragments can undergo further accretion that can move the companions toward closer separations and more equal masses. A third scenario produces a companion star by fragmentation of a massive disc. The parameters, i.e., separation, mass ratio, asf. of the resulting systems differ between these formation scenarios, and can be used to reconstruct the formation mechanism of the companion star.
Massive star forming regions are far away, their distances are in the range of kilo parsecs (kpc). To be able to detect companions at close physical separations, observations with high angular resolution are essential.

However, due to its optical properties the Earth atmosphere strongly limits the angular resolution to $> 0\overset{''}{.}6$ even at very good astronomical sites. To overcome this limit and exploit the full angular resolution of the telescope the technique of adaptive optics (AO) has been developed. An AO-system counters the disturbances produced by the atmosphere and reconstructs the original information contained in the light from the star.
Fig.1.1 depicts a typical realization of an AO-system. In addition to the science object one usually needs a reference source bright enough for the measurement of the atmosphere. This reference source needs to be close ($\leq 30''$) by the science object because the wavefront aberrations change significantly on scales larger than this separation. One usually refers to this angular separation as 'isoplanatic angle'.

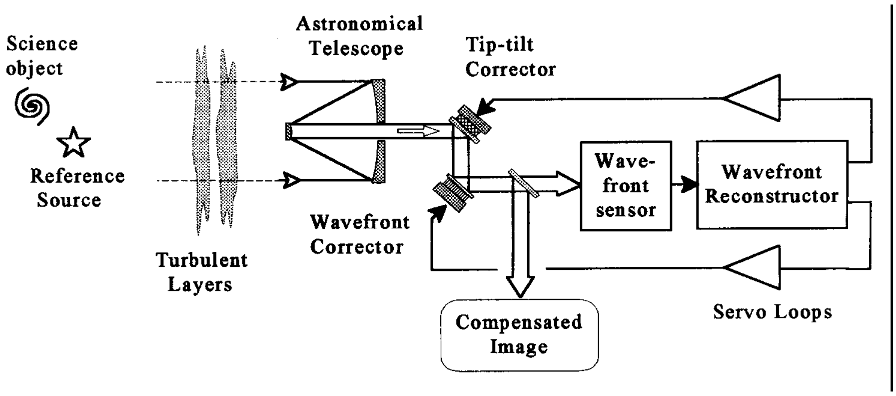

Figure 1.1: *Schematic set up of an AO-system (from Hardy 1998).*

The working principle of the system in Fig.1.1 can be described as follows: the light is collected by the telescope. Downstream of the secondary mirror a steerable mirror for pure image movement correction (TT-mirror) and then a second one, a mirror with a deformable surface (DM), for the correction of the residual wavefront aberrations are placed. After these mirrors the path of the light is split by a dichroic. One part forms the image on the science camera the rest is collected and measured by the wavefront sensor. The signals measured by this sensor are used by the wavefront reconstructor to calculate the shape for the DM, and the image motion. The information on the image motion is sent to the TT-mirror that stabilizes the position of the beam. The calculated shape is sent to the DM which then compensates the residual aberrations produced by the atmosphere. The entire system works in a feedback loop.

Due to the evolution of the atmospheric conditions (wind, turbulence) the feedback loop has to run at frequencies of typically 100 Hz or larger. The result is that the reference source (the guide star) needed for the measurement has to be relatively bright and (remember that it has to be close to the science object) consequently the sky coverage, i.e., the area of the night sky where the technique can be used, is small (a few percent). Therefore, any improvement enlarging the sky coverage is highly valuable.

This improvement does not necessarily need to apply to the whole sky. Imagine an observer interested in the formation of stars as we are. Star forming regions are deeply enshrouded in dust and often do not present a star bright enough for an AO-system using visible light for the measurement[1]. However in many cases this lack of guide stars changes if one uses longer wavelengths, i.e., the near infrared regime (1.2-2.2 μm) where the obscuration by dust is far less severe for wavefront sensing. So in this case a possibility to increase the sample coverage is to change the wavelength regime in that the wavefront sensor measures.

Another increase of the sky coverage can be gained by developing novel wavefront sensing techniques. Both things are applied in the PYRAMIR instrument that senses at near infrared wavelength and uses a novel concept of measuring the wavefront disturbances.

1.1 Aim of this work

This work is split in two parts: part one presents the laboratory and on-sky commissioning of the pyramid infrared wavefront sensor PYRAMIR mounted at the 3.5 m telescope of the Centro Astronómico Hispano Alemán in Spain. The aim of this testing is to detect a proposed superiority in performance over the conventional Shack-Hartmann sensor. To do so we tested the sensor response under various conditions in the laboratory. From the measurements we constructed an analytical model to predict the on-sky performance. In a first step this model was compared to real measurements on-sky. In a second step the model was extrapolated and compared to measurements of the Shack-Hartmann based AO-system NACO mounted at the Very Large Telescope (VLT) in Chile. A further extrapolation led to predictions for the next generation of extremely large telescopes (ELTs).

In part two we present high angular resolution images of massive and intermediate-mass stars

---

[1] The use of a laser projected on the sky as light source will not be discussed here.

to tackle the problem of the formation of massive stars. The aim is to detect differences between the binary parameters (separation, mass ratio, and total number of companions per primary star) of the two samples. The binary parameters are compared to predictions from the different models of the formation of multiple stars. We also performed a comparison to different star forming regions found in the literature to test if our findings are universal.

This entire analysis gives crucial constraints on the binary parameters. It can also strongly hints toward differences between the formation of massive and lower-mass stars. Further investigations to enlarge the sample and improve the statistical significance on one hand, and to increase the minimum and maximum range of separations on the other, will further support these arguments to eventually solve the astronomical riddle of massive star formation.

The remaining part of the thesis is structured as follows: Chapter 2 contains a more detailed excursion over the effects the atmosphere has on astronomical images and the technique of AO. This includes a comparison of different wavefront sensing concepts. The effects of fundamental limitations of a pyramid wavefront sensor (PWFS) on the proposed superiority over a Shack-Hartmann sensor (SHS) are discussed in depth. 'Fundamental' in this case is not meant to be based on natural laws and constants, but on always-present aberrations and nonideal conditions. Thus, the fundamental limitations discussed here can be eased by careful alignment and set-up of the system, but they can never entirely be removed. In this context, we explore the effect of static aberrations, different calibration light sources on the response of the system, and present detailed measurements of diffraction and scattering on the pyramid edges. Chapter 3 presents the PYRAMIR instrument in detail. The optical path and the implemented detector read out modes are explained. This chapter also accounts for the calibration procedure of the system. Chapter 4 shows measurements of the fundamental limitations to the performance of a pyramid system discussed in Chapter 2. In the same chapter the implications of the modal cross talk, aliasing, and measurement error of the system on the number of modes to be used on-sky, and the residual wavefront error are calculated. In Chapter 5 we compare our laboratory measurements to theoretical predictions and describe the performance model constructed upon them. Chapter 6 presents the results we achieved on-sky. Measurements of TT-jitter are presented and the full high order (HO) performance curves are compared to our model. In the following chapter we use the model to compare PYRAMIR to measurements performed with the NACO infrared sensor and predict the behavior of a PYRAMIR-like system on an ELT. Chapter 8 contains the discussion and conclusion of this instrumental part.

The thesis continues with the observations of massive and intermediate-mass stars in the Cepheus OB2/3 association. After an introduction about the contemporary state of binary theory and observations in chapter 9, we present details about the two associations in Chapter 10. The observational technique and the data reduction are subject of the following chapter. In Chapter 12 we present the results of the observations. Binary parameters like companion star fraction (CSF), the mass function (MF) of the companion stars and correlations between mass and separation are derived, and compared between a sample of intermediate-mass stars and a sample of massive stars. In Chapter 13 we discuss the results in comparison with the theoretical models presented in Chapter 10. To get a more general picture we also compare them with measurements from other star forming regions found in the literature. This part of the thesis is then concluded in Chapter 14 with a summary of the findings. The final chapter contains a summary of the most important results of the investigations of both, the instrumental part and the observations.

Chapter 2

Adaptive Optics Background

In this chapter we will see the drawbacks from observations through the atmosphere and how to overcome them. In section 2.1 the standard model of the atmosphere as a turbulent medium is presented and important atmospheric parameters will be introduced. In section 2.2 the focus is set on the way, how to describe the aberrations of the light collected by the telescope. Following is the presentation and discussion of different 'wavefront sensor' (WFS) concepts. Two different kinds of WFS, i.e., the so called 'Shack-Hartmann sensor' (SHS) and the pyramid wavefront sensor (PWFS) will be described in detail. The prediction of superior performance of the PWFS over the SHS will be examined carefully. Within this discussion we will see a number of error sources or effects that can reduce the performance of the system. Each of them will be discussed in depth.

2.1 The Turbulent Atmosphere

Everyone who has flown in an airplane can confirm that Earths atmosphere is a turbulent medium. The reason for this turbulence are solar heating and wind. The result is that the atmosphere consists of eddies with different sizes and temperatures moving in different directions. The difference in temperature entails variations in the refractive index that means observing through the atmosphere is like looking through layers of moving lenses of different sizes and refraction powers. For an observer this means that the light from celestial objects is distributed over a large area. This so called 'seeing disk' is much larger than the diffraction limit of the telescope. This means that the resolution of the telescope is strongly reduced. In the same time the height of the peak, i.e., the intensity in the center of the image is reduced. This entails that we need much longer integration times compared to the case without atmosphere.

To describe the scenario in more physical terms the light from a star on the boundary of the atmosphere has a flat wavefront, i.e., the phase of the electromagnetic field does not change orthogonally to the direction of travel. This is changed during the way through the atmosphere and the wavefront arriving at the telescope is bend many times. The goal of an adaptive optics system, therefore, can be stated as reflattening of the wavefront. For a more detailed discussion see for example Hardy (1998).

2.1.1 The Kolmogorov Model of the Atmosphere

In 1941 Kolmogorov developed a model to describe the processes in a turbulent fluid medium. It treats the fluid as consisting of turbulence eddies of different sizes ranging from the largest size L_0, the 'outer scale', to the smallest size l_0, the 'inner scale'. In the case of the atmosphere $L_0 \approx$ 10-100m and $l_0 \approx$ a few cm.
The basic idea behind this model is that the turbulence first introduces eddies of size L_0 that then break down to smaller and smaller parts until, when the size of the eddies reaches l_0 where the energy of the turbulence is dissipated as heat, the flow becomes laminar.
To describe the effects of the atmosphere Kolmogorov developed so called structure functions, i.e., generalized correlation functions. The structure function of phase fluctuations ϕ of an electromagnetic wave traveling through the turbulent medium for example is given by (Hardy 1998),

$$D_\phi(\rho) = \langle|\phi(r) - \phi(r+\rho)|^2\rangle_r \tag{2.1}$$

where r is a position on sky, ρ is the spacial distance from this position and $\langle\rangle_r$ is the ensemble average. This function can be expressed by (Hardy 1998),

$$D_\phi(\rho) = 6.88 \left(\frac{|\rho|}{r_0(\lambda)}\right)^{5/3} \tag{2.2}$$

where $r_0(\lambda)$ is the so called 'Fried-parameter', the coherence length of the atmosphere that depends on the wavelength of the light as (Hardy 1998):

$$r_0(\lambda) \propto \lambda^{6/5} \tag{2.3}$$

At the scale of r_0 the wavefront root mean square (rms) reaches approximately 1 rad as has been shown by Fried (1966),

$$\sigma^2 = 1.03 \left(\frac{D}{r_0}\right)^{5/3} \tag{2.4}$$

Here σ^2 is the wavefront aberration of the electromagnetic wave in rad^2 and D is the diameter of the telescope used for observation. For visible wavelengths r_0 is approximately 5 to $\geq$ 20 cm. Using equation 2.3 in the near infrared (nir) at 2.2μm this formula yields a coherence length between 20 and 80cm.
The resolution R of large telescopes is limited by the astronomical seeing and given by

$$R = 1.22\lambda/r_0 \tag{2.5}$$

Therefore, in the optical (λ = 500nm) it is limited to $\approx 0''.6$. In comparison: for an 8m class telescope the full diffraction limited resolution at this wavelength would be $0''.015$. Therefore, a way to compensate the effects the atmosphere causes on the electromagnetic waves has been looked for and, in 1953, the so called adaptive optics (AO) has been proposed by Babcock and was first realized in 1977 by Hardy et al.

2.2 Modal Decomposition

After the discussion of what causes the disturbance of the light arriving at the telescope, we need to derive a scheme how to compensate these wavefront aberrations. To do so an approach how to describe the wavefront disturbance must be derived.

There are two main approaches how the DM of an AO system can correct the wavefront errors: one is the so called 'zonal correction' the other is the 'modal correction'. Here we will focus on the second approach.

For the modal correction the wavefront $\phi(x, y)$ is decomposed into a series of orthonormal functions f_i with amplitudes a_i ,i.e.,

$$\phi(x, y) = \sum_{i=0}^{\infty} a_i f_i(x, y) \tag{2.6}$$

A widely used set of functions are the 'Zernike polynomials'. This set of modes is basically an extension of the 'classical' optical aberrations found for lenses or mirrors, i.e., focus, astigmatism, and coma, to an infinite set of modes. These functions have the property that one can arrange them in an order of increasing power in the dependence on the radial direction, i.e., r, r^2, r^3 asf. This power will be referred to as 'radial order'.

To define the most appropriate set of modes for a correction of the aberrations produced by the free atmosphere, one chooses the modes in such a way that, after the correction of a given number of modes, the residual wavefront error is minimized. These modes can be constructed from the condition,

$$\sigma^2_{n-res} = \int_{Pupil} \left(\phi(x, y) - \sum_{i=0}^{n} a_i f_i(x, y) dx\, dy \right)^2 = min \tag{2.7}$$

where σ^2_{n-res} is the residual wavefront error after the correction of the first n modes and the pupil is the (usually annular) telescope pupil. The a_i are varied. The solutions are the eigenvectors to the eigenvalues of the matrix M_{ij} in decreasing order,

$$M_{ij} = \int_{Pupil} f_i(x, y) f_j(x, y) dx\, dy \tag{2.8}$$

For the Kolmogorov turbulence and a circular telescope pupil this set contains the so called 'Karhunen-Loeve-functions'. In this case the residual error after correcting N modes for N > 10 is slightly smaller than that for the Zernike polynomials given by (Hardy 1998),

$$\sigma^2_{fit}(N) = 0.2955 \left(\frac{D}{r_0} \right) (N + 1)^{-\sqrt{3}/2} \tag{2.9}$$

where D is the diameter of the telescope and r_0 is again the Fried parameter.

2.3 Different Wavefront Sensing Concepts

Now we have a concept how to decompose the wavefront. But to do so we need to measure it in the first place. The appropriate device to perform this measurement is the WFS. Various types of WFS have been contrived. But only three of these types of WFS are actually in use on astronomical telescopes: SHSs, PWFSs and curvature wavefront sensors (CWFS). The discussion will focus on the first two sensor types. For a description of the CWFS and other sensors see for example Hardy (1998), for the newest developments of the CWFS technique see Guyon et al. (2008).

In the following we will describe the working principles of the SHS and the PWFS and compare their qualities for AO application in terms of error propagation.

2.3.1 Shack-Hartmann Sensor

he SHS is the most intuitive of the sensor types. It originates from an idea of Hartmann (1900) to test the quality of lenses. For this test he employed an opaque mask with holes. These holes act as subapertures each of them forming an image. The relative positions of the images with respect to a reference position represent the local wavefront slopes.

Shack later exchanged the mask by a lenslet array that he used to measure wavefront aberrations. T Fig.2.1 shows a sketch of such a SHS in an astronomical application.

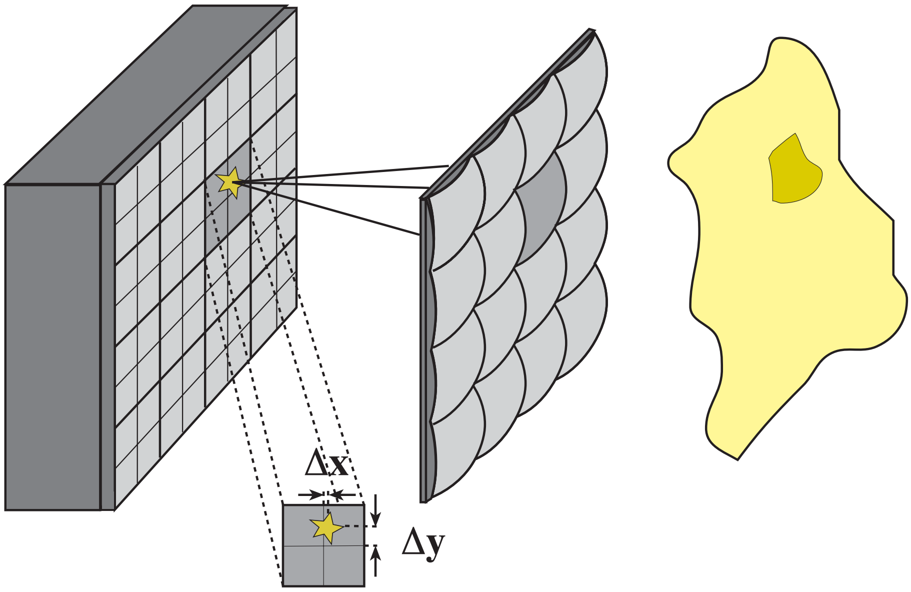

Figure 2.1: *Setup of a SHS (Courtesy of S. Hippler). Due to a local wavefront tilt the spot is displaced by an amount of Δx and Δy in x- and y-direction respectively.*

The pupil of the telescope is imaged onto an array of small lenslets. These subapertures have the size of the median Fried-parameter r_0 in the science wavelength. Each lenslet images the target onto the detector. From the displacement of the single images with respect to a pre-defined reference position the average local wavefront slope $\int_{sub} dxdy \frac{\partial \phi}{\partial x}$ is measured. The integral is taken over the subaperture and ϕ is the phase of the electromagnetic field. The angular displacement $\Delta\alpha$ of a spot at wavelength λ with respect to a pre-defined reference position can be calculated to be

$$\Delta\alpha = \frac{\lambda}{2\pi A_{sub}} \int_{sub} dxdy \frac{\partial \phi}{\partial x} \tag{2.10}$$

where A_{sub} is the area of the subaperture.
The dependence of the measurement error σ^2_{meas} on the number of corrected Zernike modes can be described as (see Rigaut & Gendron 1992),

$$\sigma^2_{meas} \propto (S/N)^{-2} \sum_{q=1}^{Q} 0.590(q+1)^{-2.05} + 0.174(q-1)(q+1)^{-2} \tag{2.11}$$

where q is the radial order of the modes, Q$\propto \sqrt{N_{sub}}$ is the maximum radial order to be corrected (approximately equal to the square root of the number of subapertures N_{sub}), and (S/N) is the signal to noise per subaperture. For larger Q the second summand is the leading term. It is proportional to Q^{-1} and, thus, the sum is rising logarithmically with the radial order of the modes.

2.3.2 The Pyramid Wavefront Sensor Concept

In contrast to the SHS where the sensing of the wavefront is done in the pupil plane, the PWFS is a focal plane WFS.
Wavefront sensing based on the pyramid principle has its origin in the Foucault knife edge test. This test is designed to examine the quality of optical surfaces in terms of aberrations. A knife edge is inserted into the beam near the focal plane and then moved slowly toward the focal point. If the optics are perfect the light is blocked suddenly when the knife edge reaches the focal point. Aberrations in the beam cause the shading to appear continuously.
An extension to larger mirrors is the 'Zonal Foucault Test'. This test is designed to find the focal point of determined zones of a large mirror. Here a mask with holes (for the zones) is placed on the mirror that leaves only two corresponding zones uncovered. Doing this for different zones one can check the variation in focal length between these small zones of the mirror and determine the quality of the entire mirror.
Until 1948 the results of the test were interpreted in terms of ray optics only. Linfoot (1948) showed that these calculations yield erroneous results. He constructed a diffraction theory of the knife edge test. Still up to the 1970s the test was merely of qualitative nature until Katzoff (see reference in Wilson 1975) managed to invert the description. Now there was a theory where the irradiance in the pupil plane could be used to describe the wavefront errors on the surface. This method was used by Wilson (1975) to test a 20 cm mirror very successfully with the Foucault test. However, an extension for the 2 dimensional problem of the pyramid has never been constructed.
The use of a rotating knife edge or a pyramid has been known since 1937 (see Babcock (1957) and references therein), but it was used exclusively for tip tilt (TT) correction. Horwitz (1994) was the first to have the idea of a pyramid like system for high order (HO) wavefront correction. He used two orthogonal filters with position dependent reflection and transmission. One year later Pugh (1995) used two bi-prisms for wavefront sensing. The 'true' pyramid principle, using a prism that has the shape of a four-sided pyramid, was invented by Ragazzoni (1996). After Ragazzonis publication there has been the discussion about the necessity of "modulating" the pyramid, i.e., the need to move the beam around the pyramid tip during a single integration

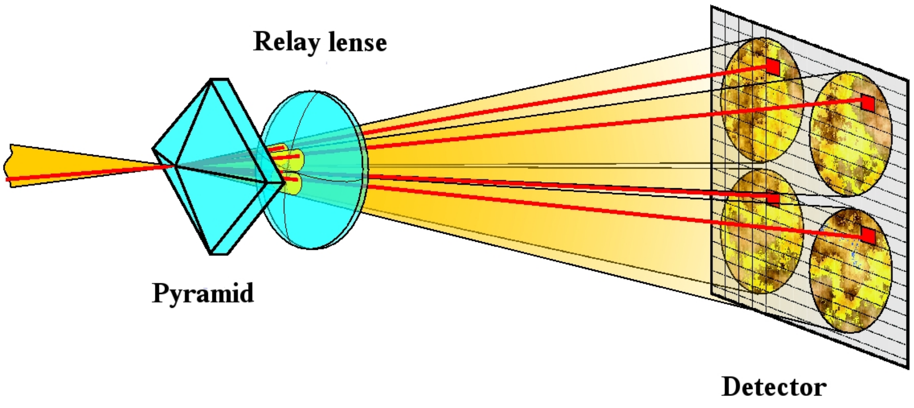

Figure 2.2: *(Courtesy of S. Egner) Pyramid principle. An example of corresponding pixels is marked.*

cycle (see Sec. 2.3.3). The modulation causes an extension of the linear regime of the sensor at the expense of sensitivity to small wavefront errors. For a modulation amplitude of $\frac{\lambda}{r_0}$ the sensor is equivalent to a SHS. Later it was shown theoretically by Costa (2003) and demonstrated on the sky by Peter et al. (2008) that this modulation is not necessary.

2.3.3 The Pyramid Principle

For a further comparison between the SHS and PWFS we need to understand how a PWFS works and what the measurement error of such a system is.
The optical setup of a PWFS is shown in Fig. 2.2.

The transmissive, four-sided pyramid prism is placed in the focal plane. In the nonmodulated case the focus is placed on the tip of the pyramid. Modulation displaces the beam circularly around the tip. After the pyramid a relay lens images the pupils onto the detector.

The signal a this PWFS system uses are the intensities inside four pupil images. The illumination of these images depends on the aberrations of the wavefront. The signal S one extracts is the difference in intensities $I_{1,2,3,4}$ between corresponding pixels in the four pupils, i.e., the pixels at the same optical position in the pupils as shown in Fig.2.2. This signal is given by,

$$S_x(x,y) = \frac{I_1(x,y) + I_3(x,y) - [I_2(x,y) + I_4(x,y)]}{I_1(x,y) + I_2(x,y) + I_3(x,y) + I_4(x,y)} \tag{2.12}$$

$$S_y(x,y) = \frac{I_1(x,y) + I_2(x,y) - [I_3(x,y) + I_4(x,y)]}{I_1(x,y) + I_2(x,y) + I_3(x,y) + I_4(x,y)} \tag{2.13}$$

for the x- and y-direction respectively. These signals S are what we will refer to as gradients, even if they might not exactly represent wavefront gradients. Using a modulated PWFS with a

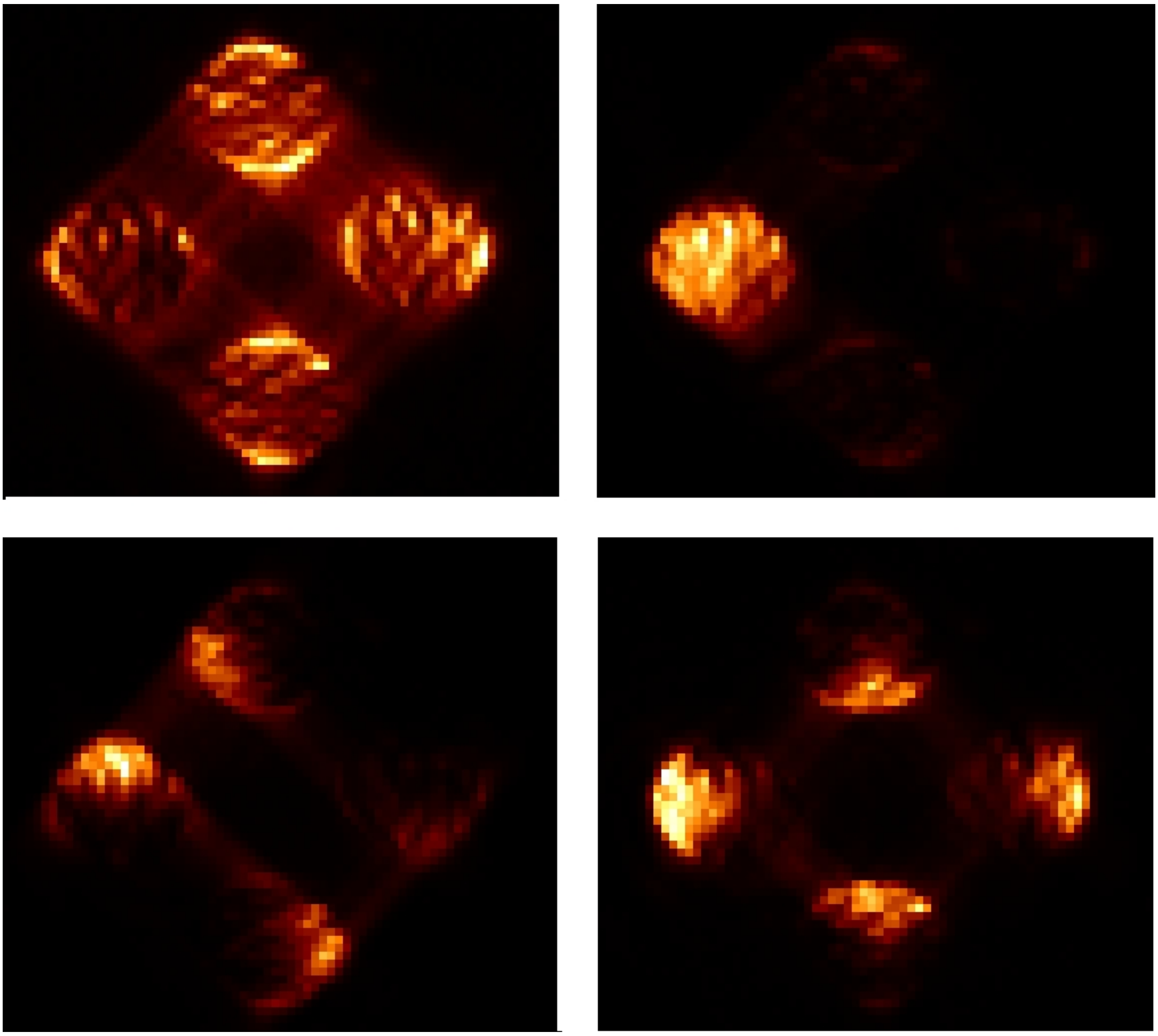

Figure 2.3: *Examples of wavefront aberrations as measured by PYRAMIR. Upper left: reference (almost) flat wavefront, lower left: astigmatism 1, upper right: tip, lower right: astigmatism2 (45° rotated wrt. to astigmatism1)*

large enough modulation amplitude α the signal measured by the sensor for small wavefront perturbations is given by (Verninaud 2004),

$$S_x = \frac{\lambda}{\alpha\pi^2}\frac{d\phi}{dx}. \tag{2.14}$$

This shows clearly that the sensor is working as a wavefront slope sensor, equivalent to a SHS as already stated above. In general, the expression for a sensor with an arbitrary modulation angle α (here for simplification the modulation is done linearly) is given by (Verninaud 2004):

$$S_x(x,y) = \frac{1}{2\pi\alpha} \times \int_{-\alpha}^{\alpha} d\alpha' \int_{-B(y)}^{B(y)} dx' \times$$

$$p.v.\frac{sin\left(\phi(x',y)-\phi(x,y)+\frac{2\pi}{\lambda}\alpha'(x'-x)\right)}{x'-x} \tag{2.15}$$

in the x-direction, where $p.v.$ means principal value and $\pm B(y)$ are the borders of the pupil in the y-direction. For no modulation and in the limit of small perturbations and a telescope with infinite aperture the equation yields a frequency spectrum of (Verninaud 2004),

$$\widetilde{S_x} = isgn(u)\widetilde{\phi}(u,v). \tag{2.16}$$

Here $\widetilde{()}$ means Fourier transform and $sign$ the sign-function (see Costa 2003). Thus, the sensor is working as a phase sensor in this regime. In real life however we have neither an infinite telescope nor small perturbations what means calling the measured signals wavefront gradients is not far from the truth.

The error propagation of a PWFS is different from that of the SHS. Due to the fact that it uses the full telescope diameter for the sensing (without any division into subapertures), the measurement error from the SHS has to be corrected for that to yield the measurement error of the pyramid (see Ragazzoni et al. 1999),

$$\sigma^2_{meas} \propto (S/N)^{-2} \sum_{q=1}^{Q} \left(\frac{q}{Q}\right)^2 [0.590(q+1)^{-2.05} + 0.174(q-1)(q+1)^{-2}] \tag{2.17}$$

Again the second term is the leading one. So obviously for larger Q the measurement error becomes independent of Q, i.e., constant.

2.3.4 The Prediction of Superiority

From the different expressions of the measurement error for the SHS and PWFS (see Eq.2.11 and 2.17) Ragazzoni et al. (1999) predicted a gain in sensitivity – and, thus, in limiting magnitude, i.e., the magnitude where the systems correction starts to degrade the image rather than to improve it – for a nonmodulated PWFS over a SHS. This prediction has been made for a system working in closed-loop conditions and with a well corrected point source. The definition of this gain is that, to achieve the same correction quality, the PWFS needs less signal than the SHS. This gain in sensitivity results basically from the fact that the accuracy of the measurement and the resulting reconstruction error σ^2_{SH} of the SHS depends on λ/d_{sub}. λ is the sensing wavelength and d_{sub} is the size of a subaperture size. This size is typically chosen of the order of the Fried-parameter r_0 at science wavelength for typical site seeing. In contrast to this accuracy measurement error of a PWFS σ^2_P of a PWFS depends on λ/D where D is the telescope diameter ($D >> r_0$). The difference in stellar magnitudes that are needed to achieve the same Strehl ratio (SR) for the exemplary case of the TT-mode only can be derived for both sensors as $\Delta m = -2.5log\,(\sigma^2_P/\sigma^2_{SH}) \approx -2.5log\,(r_0^2/D^2)$. If we include HO-modes in the calculation we have to use Eq. 2.11 and 2.17. From the calculation the gain in sensitivity including all modes up to radial order 20, for a 4 m class telescope and a seeing of $0.''5$ ($r_0 = 20\,\text{cm}$), is predicted to be 2 magnitudes (see Fig. 2.4 with $Q = D/r_0$). This prediction for a system working at diffraction limit was later extended to partial correction only (Esposito et al. 2001). In the case of a

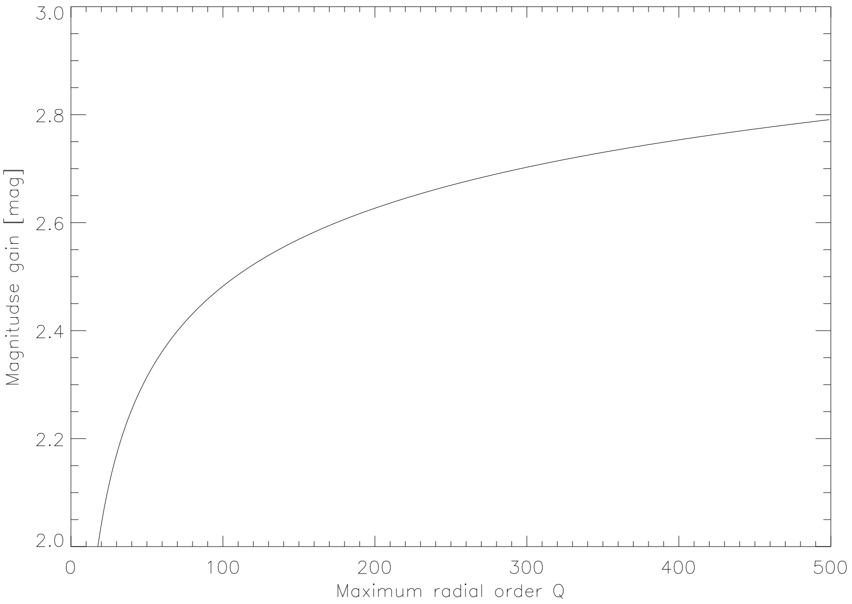

Figure 2.4: *Gain in limiting magnitude of the PWFS over the SHS. The gain is calculated from Eqs. 2.11 and 2.17.*

nonmodulated pyramid and a wavefront with 3.3 rad^2 residual variance, there should still be a gain in sensitivity. This wavefront amplitude is beyond the theoretical end of the linear regime of the sensor as derived below (see Sec. 2.5). In the case of a modulated PWFS, the gain in sensitivity is present for even larger wavefront errors, but of course it is generally smaller.
In the following we will quantitatively discuss various effects that potentially reduce the gain in sensitivity a pyramid system has over a SHS.

2.4 Fundamental Restrictions

The fundamental properties of a PWFS system that can strongly influence the performance are fundamental not so much in the sense of natural laws and/or constants, but they can be mitigated by appropriate design and alignment procedures. However, they can never entirely be removed! These properties include the diffraction and scattering effects on the pyramid edges, a not-well centered beam on the pyramid tip, read out noise (RON) of the camera, a nonhomogeneous illumination of the pupil during calibration, and noncommon-path aberrations. The impact of each of these possible sources of reduced performance will be discussed below. Measurements of these quantities will be given in Chapter 4.

2.4.1 Impact of the Pyramid Edges

There are two effects of the pyramid edges that yield a loss of light in the pupil images. One is the diffraction at the edges of the pyramid. Even in the case of a hypothetical perfect pyramid some light will be diffracted out of the pupils. The second reason of light-loss is the finite size of the edges. Here, the light will be scattered anywhere, but it will not produce a useful signal in any of the pupil images. In the case of a perfectly flat wavefront, there is up to 50% of the light (0.75 mag) diffracted outside the pupils (see Sec. 2.4.1) and, therefore, unavailable for the reconstruction. Of course, in real closed-loop conditions, the loss of light due to diffraction is much less due to partial correction only. The strength of the effect of the finite size of the edges depends on the ratio of the full width at half maximum (FWHM) of the beam on the pyramid tip and the size of the edges. So this effect depends strongly on the details of the system

2.4.2 Partial Correction

In the regime of partial correction, due to the reduced quality of the wavefront the spot size on the pyramid tip will increase. This has a similar effect as modulation that reduces the limiting magnitude toward the value for the SHS.
The spot on the pyramid produced with a signal with wavefront error σ^2 consists of a diffraction limited core with width a_C and height H_C (see Hardy 1998)

$$a_C = 1.22\frac{\lambda}{D},\ H_C = exp(-\sigma^2) \tag{2.18}$$

and a halo of width a_H and height H_H

$$a_H = 1.22\frac{\lambda}{D}\left[1+\left(\frac{D}{r_0}\right)^2\right]^{\frac{1}{2}},\ H_H = \frac{1-exp\left(-\sigma^2\right)}{1+\left(\frac{D}{r_0}\right)^2}. \tag{2.19}$$

The true limiting magnitude then depends upon the sum of the two signals weighted by the amount of light of each one. Thus, we assume 50% diffraction at the pyramid edges for the core and no diffraction for the halo. To calculate the expected gain in magnitude for partial correction we use an effective diameter D' of the telescope:

$$D' = 1.22\lambda\frac{0.5a_C H_C + a_H H_H}{a_C^2 H_C + a_H^2 H_H} \tag{2.20}$$

In Fig.2.5, left panel, the loss in limiting magnitude for r_0 = 0.5 m

dependence on the correction quality is shown. Obviously for faint stars the gain drops toward zero.

2.4.3 Read Out Noise

The early simulations that led to the prediction of PWFS' superiority also always assumed that there was no RON in the system. But of course, in the regime of faint stars RON is quite important. Here we should recall that the "gain" in sensitivity basically means that one needs a lower photon flux for the PWFS in order to achieve the same SR as for the SHS. Consequently, the RON will effect a PWFS stronger than a SHS, because the number of photons per subaperture

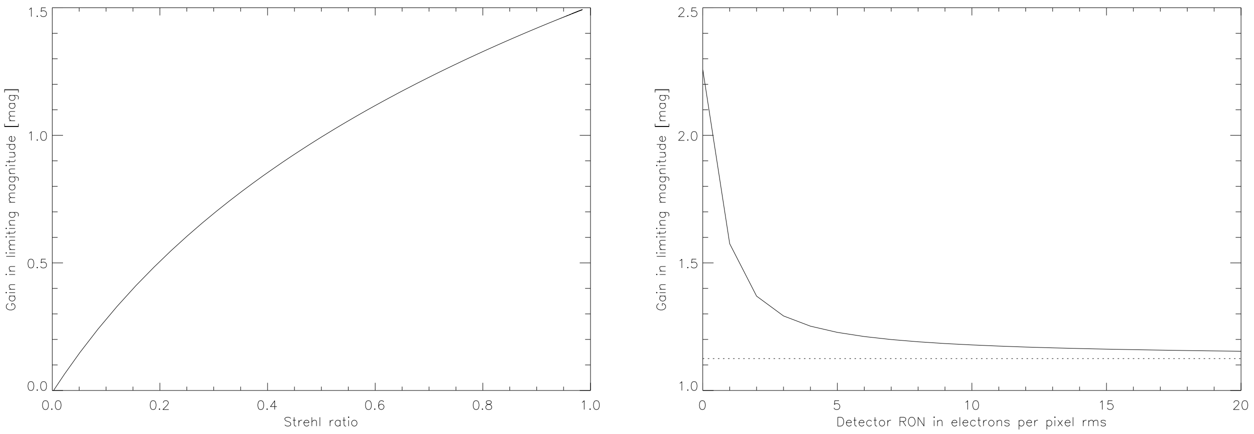

Figure 2.5: *Left: gain in limiting magnitude for the PWFS over the SHS. In contrast to Fig.2.4 we included the effect of diffraction on the pyramid edges and degradation of the wavefront toward low SR. Shown is the gain in limiting magnitude for partial correction versus the SR ($r_0 = 0.5m$). The predicted gain for a perfectly corrected wavefront in this case is 2.25 mag.*
Right: gain in limiting magnitude for a PWFS dependence on the detector RON. The S/N for the pyramid is 1 for the predicted gain in sensitivity of 2.25 magnitudes. For larger RON the number of magnitudes we gain drops to half its size (dotted line).

can be smaller in the case of the PWFS. This can be seen from the calculations of the photons needed for a given S/N,

$$N_{ph} = S/N \left(\frac{1}{2} S/N + \sqrt{\frac{1}{4}(S/N)^2 + 4RON^2} \right). \tag{2.21}$$

Therefore, the higher the S/N of the photon flux alone, the less important the RON. Note that here we use quad-cell detectors as subapertures of the SHS.

From the above equation one can easily derive the magnitudes we lost to RON as,

$$\Delta m = 2.5 \log \left(0.5 + \sqrt{0.25 + 4RON^2/(S/N)^2} \right). \tag{2.22}$$

Taking a S/N of 1 per subaperture for the pyramid, and starting from a predicted magnitude gain of 2.25 mag versus the SHS, and a RON of 1 e^- root mean square (rms) (as can be reached using EMCCD (see Mackay et al. 2001)) the RON is exceeding the photon noise and the flux by a factor of 2. Therefore, the signal to noise ratio is reduced from about 1 to $1/\sqrt{5}$ or even less. This reduction will have severe consequences for the correction because the measurement error is inversely proportional to $(S/N)^2$.

We can estimate this loss in magnitude gain by calculating the number of photons needed to achieve again the old S/N of 1, and the corresponding S/N of the SHS, now with RON included. Fig.2.5, right, shows the gain in magnitude dependence on the RON. In the case of 1 e^- RON rms we already loose 0.7 mag of the gain. The curve asymptotically reaches half of the original gain in magnitude.

Additionally to light loss and RON, there is a predicted loss of 0.5 mag in the gain due to the finite sampling size of the detector (Verinaud 2004).

2.4.4 Centering on the Pyramid Tip

The centering of the beam on the pyramid tip is important in order to evenly distribute the light between the four pupil images. A decentered beam has two effects reducing the performance:

1. The calibration of reduced quality
2. The noise of the gradients is increased

Both effects enter the measurement error $\sigma^2_{meas} = tr(RR^T)\sigma^2_{grad}$ where R is the reconstruction matrix, constructed from the calibration of the system, and σ^2_{grad} is the error of the gradients. This measurement error determines the limiting magnitude of the system, i.e., the faint limit of the regime in which the AO system can improve the image. The two effects described above, thus, reduce the limiting magnitude of the system.

2.4.5 Pupil Illumination Flatness

In the case of a PWFS the wavefront is measured in the focal plane. Due to this fact it is important that the illumination of the pupil is as uniform as possible. The problem that can arise here results from the fact that the output of a (singlemode) fiber, frequently used in AO systems as a calibration light source, has a Gaussian intensity profile. Imagine a system with the following properties: a F/10 output beam, the pupil image has a diameter of 0.1 m, the calibration fiber has a numerical aperture of 0.2 and the FWHM of the beam in the fiber has a diameter of 5 μm. At the pupil plane of this system the FWHM of the beam is 0.1 m. This means we have an intensity drop of 50% from center to edge. Simulations show that calibrating under these conditions and then changing to a star, that, disregarding scintillation, has a flat intensity distribution, will reduce the linear regime of the sensor (that is already small; Peter et al. 2006). To be more quantitative: for an illumination with a FWHM of σ the signal S on the pyramid tip will be,

$$S \propto \int_{Pupil} exp\left(-\frac{r^2}{2\sigma^2}\right) exp[i\psi(r,\phi)] exp[ikrcos(\phi)] r\, dr\, d\phi. \tag{2.23}$$

where r, ϕ are polar coordinates, $\psi(r, \phi)$ is the phase of the electromagnetic wave and k is the wave number. The effect is a smearing of the frequencies in the focal plane in radial direction. For a flat wavefront the intensity distribution S on the pyramid is calculated as

$$S \propto exp\left(-\frac{\sigma^2 k^2}{2}\right). \tag{2.24}$$

Thus, the spot has the larger diameter of $1/\sigma$. It is easy to see the influence on the TT-mode: if the intensity distribution has a FWHM σ, then the spot in the focal plane (on the pyramid tip) will have the size $1/\sigma$. It is, therefore, wider than for an evenly illuminated flat wavefront. If it is for example twice as wide then the TT-signals from the star will be overestimated by a factor of 2.

2.4.6 Noncommon-path Aberrations

For AO observations the pathes of the light to the science camera and the wavefront sensor differ. The result are noncommon-path aberrations, i.e., a difference in the static aberrations of the path to the wavefront sensor and the science path. To provide the best possible science image these aberrations are, at least during observation, offloaded into the wavefront sensor path. Therefore, in the following the terms noncommon-path aberration and static aberration will denote the same. The noncommon-path aberrations are unavoidably present in every AO system. They can have strong effects on the regime of linear response and the modal cross talk. The linear regime is important because in the linear regime the sensor will work with the best performance. The orthogonality of the modes are best in the linear regime. It should lie symmetrically around the zero point. The modal cross talk, i.e., the nonorthogonality of the modes is a potential error sources and, thus, should be as small as possible. This also induces that the mode set we use for the decomposition of the wavefront should be chosen well adapted to the geometry of the total system including telescope, DM, and atmosphere. An optimization in particular of the linear regime is crucial for a good performance of the system.

Due to the small linear regime of a PWFS it is of high importance to find a good way to deal with the noncommon-path aberrations.

Combining all the effects discussed above the resulting gain in limiting magnitude is strongly reduced. Still, the optimum way to achieve a performance superior to a comparable SHS system is to operate in the regime where the highest gain is predicted: the case of no modulation and a well corrected wavefront, i.e., the sensor should operate at a wavelength where the wavefront correction of the AO system is effective.

2.5 Testing the Prediction

There has already been an attempt to test the gain in limiting magnitude by Ghedina et al. (2003). They compared the same PWFS in the modulated (mimicking a SHS) and nonmodulated mode on the sky. As their PWFS operated at visual wavelengths, the wavefront in the sensing wavelength was, however, only partially corrected (Costa 2003). Unfortunately they do neither state the wavefront error nor the SR on the pyramid or science camera in any reference.

When they compared their measurements for the runs with modulation with those performed without modulation they found a gain in limiting magnitude of 0.12 mag for the system without modulation. Still some of their error bars are quite large and it is also not clear if this gain arises from some other effects in the system itself rather than from the mode how they operate the sensor. Therefore, their result has to be taken with care. We have discussed above that the regime where the highest gain is actually expected is that of a well-corrected wavefront. This means the quality of the wavefront should be sufficiently good to keep the sensor signal inside the linear regime of the sensor. For, e.g., the TT-modes, this regime can be derived as follows: the signal is the difference of flux of two opposite sides of the pyramid. In diffraction limit the function describing the signal in one dimension for a displacement of size a is

$$S = \frac{2}{\pi}\int_{-a}^{a}\left(\frac{sin(x)}{x}\right)^2 dx. \tag{2.25}$$

The resulting signal is shown in Fig.2.6. The linear regime reaches roughly up to $\frac{\lambda}{2D}$. This means a path difference in the pupil of $\pm\frac{\lambda}{2} = \pm\pi\, rad$ peak to valley (PV). This PV of $\pm\pi\ rad$ corresponds to a wavefront mean square of

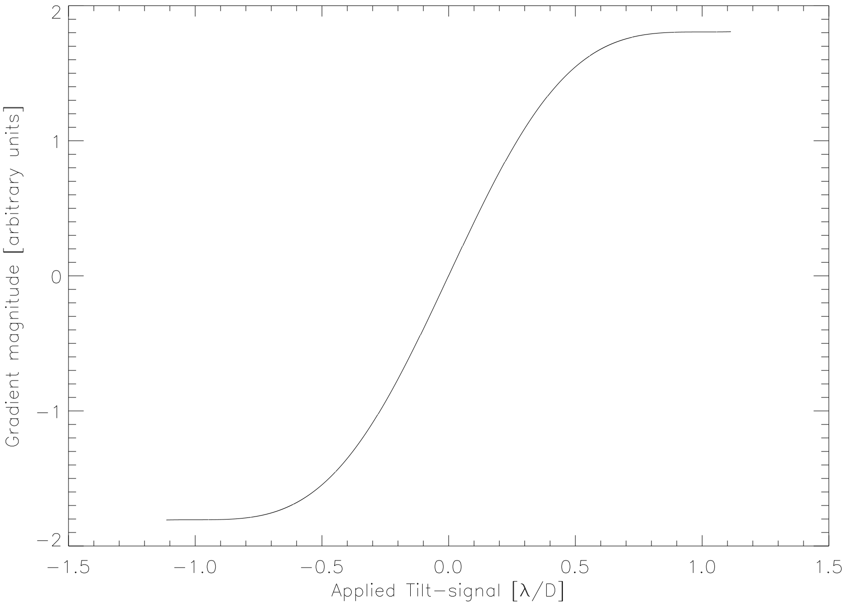

Figure 2.6: *Theoretical TT-signal. Shown is the length of the gradient versus applied signal in* λ/D*.*

$$\sigma^2 = \frac{1}{\pi r^2}\int_{-1}^{1}\left(\frac{\pi}{2}x\right)^2\left(2\sqrt{1-x^2}\right)dx = \frac{\pi^2}{16}. \tag{2.26}$$

Thus, we have a rms of $\pm\frac{\pi}{4} = 1.5rad$. This wavefront error corresponds to a SR of 10%.

The corresponding wavefront in K band has 525 nm rms wavefront aberration. We can easily see why it is beneficial to use an infrared WFS such as PYRAMIR in order to verify the prediction of superiority: the wavefront rms in R band for example would have to be about 125 nm or better to keep the signal inside the linear regime, a value still difficult to achieve by contemporary AO systems. We have seen that the SR ($SR = \exp(-\sigma^2)$ where σ is the wavefront rms in radians) depends on the wavelength of observation. σ^2 of course depends on many things but two of the most important are the fitting error due to a finite fitting of the wavefront σ^2_{f-N} and the temporal error on sky σ^2_{temp} . This temporal error consist of two parts,

1. the error due to finite bandwidth of the system σ^2_{band}

2. the error due to pure time delay σ^2_{delay}.

These errors can be written as (Roddier 1999),

$$\sigma^2_{fit}(N) = 0.3\left(\frac{d_{sub}}{r_0}\right)^{\frac{5}{3}} = 0.335\left(\frac{D}{r_0}\right)^{\frac{5}{3}}(N+1)^{-\frac{\sqrt{3}}{2}} \tag{2.27}$$

$$\sigma^2_{temp} = \sigma^2_{band} + \sigma^2_{delay} = \left(\frac{f_G}{f_S}\right)^{\frac{5}{3}} + 28.4\,(f_G\tau_S)^{\frac{5}{3}} \tag{2.28}$$

with

$$\begin{aligned} d_{sub} &= size\,of\,subapertures \\ r_0 &= Coherence\,length \propto \lambda^{\frac{6}{5}} \\ D &= Telescope\,diameter \\ N_m &= Number\,of\,free\,parameters\,(modes) \\ f_G &= Greenwood\,frequency \propto \lambda^{\frac{-6}{5}} \\ \tau_S &= Time\,delay \\ v &= Averaged\,wind\,speed \\ f_S &= Loop\,bandwidth \approx 1/15 loop\,speed \end{aligned}$$

Thus, $\sigma^2 \propto \lambda^{-2}$.

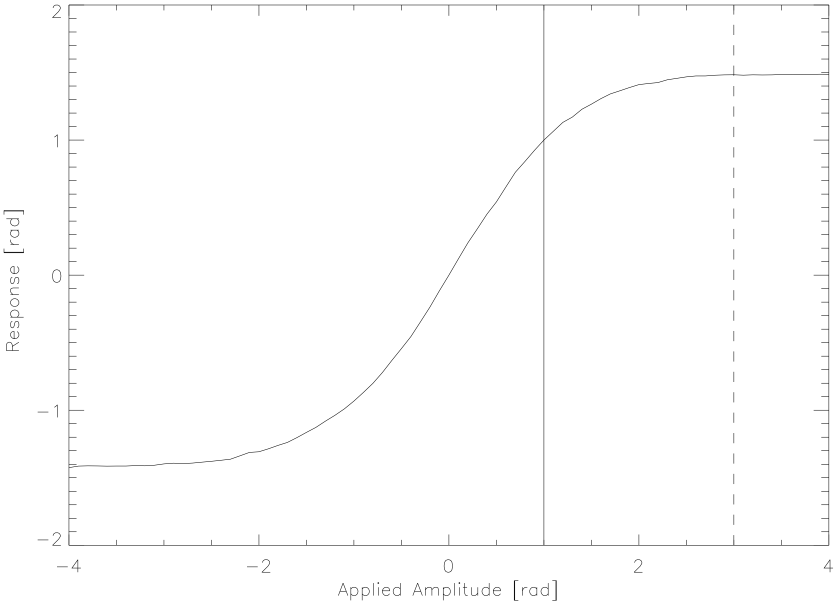

Figure 2.7: *Working point of the PWFS. The curves mark the response of the system in rad (K band) for the first 10 HO-modes. The vertical lines mark the working points for a correction with 37% SR in K band. The solid line corresponds to the correction in K band, the dashed line to a correction in the visible.*

For simplicity we (reasonably) assume the three major errors (fitting, measurement, temporal) to be of the same size, using three times the fitting error. With this assumption we can derive an expression for the number of Zernike modes we need to achieve a specified SR dependence on the wavelength:

$$N = \left(\frac{D}{r_0}\right)^2 (\sigma_{tot}^2)^{-1.2}. \tag{2.29}$$

For $r_0 = 0.7m$, a typical value for the K band, the formula yields 10 modes needed for correction to be in the linear range of the sensor. In the visible (628 nm) under the same conditions $r_0 = 0.15m$, therefore, we need $N = 210$ modes. Additionally assuming a wind speed of 3 ms^{-1} the frequency of TT changes is 4.2Hz for K band and 20 Hz in the visible. The speed of the higher modes of radial order N scales roughly like N (see Conan 1995). Taking into account that the bandwidth of the correction loop must be about 10 times as wide as the frequency of the modes to be corrected, we can derive a loop speed of 130 Hz for the infrared and 4400 Hz for the visible case. Therefore, it is clear that PYRAMIR can reach into the linear regime but for a WFS working in the visible it will be hard to even leave the saturated regime (see Fig. 2.7). Therefore, the prediction can **only** be verified on sky when sensing is done in the **near infra-red**!

Chapter 3

The PYRAMIR System

In the last chapter we learned that to test the prediction of superior performance of a PWFS over a SHS we have to go to infrared wavelengths. To do so we constructed the pyramid infrared WFS PYRAMIR (see Fig. 3.1).

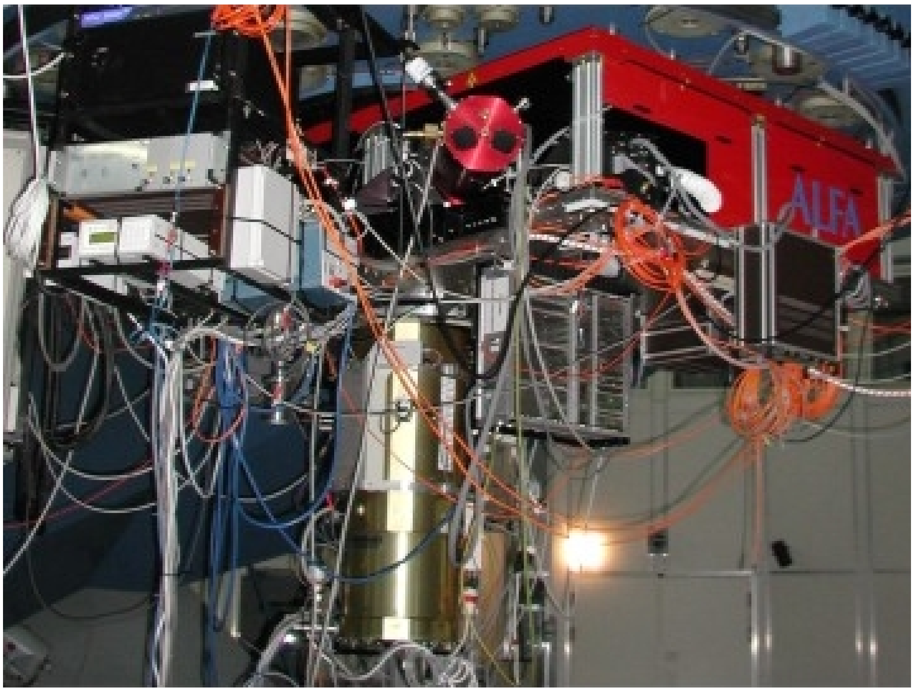

Figure 3.1: *PYRAMIR as built into the ALFA AO bench at the 3.5m telescope of the Calar Alto observatory.*

The system will be described in detail in this chapter. The path of the light, as well as technical details on the possible configuration to run the system will be specified. With a description of the calibration procedure and its peculiarities we will end the chapter and start with the results of the measurements in the next chapter.
PYRAMIR is a PWFS working in the effective wavelength regime between 1.26 and 2.4 μm (J, H, K bands).

It is integrated into the ALFA-AO-system (for details on ALFA see Kasper 2000) at the 3.5m telescope of the Calar Alto observatory.
The properties of the system are shown in Table 3.1. The beam splitter can be exchanged manually. Here, the choice is between 90% light on PYRAMIR 10% on the science camera (P90O10), 20% on PYRAMIR and 80% on the science camera (P20O80), or K band on PYRAMIR and J

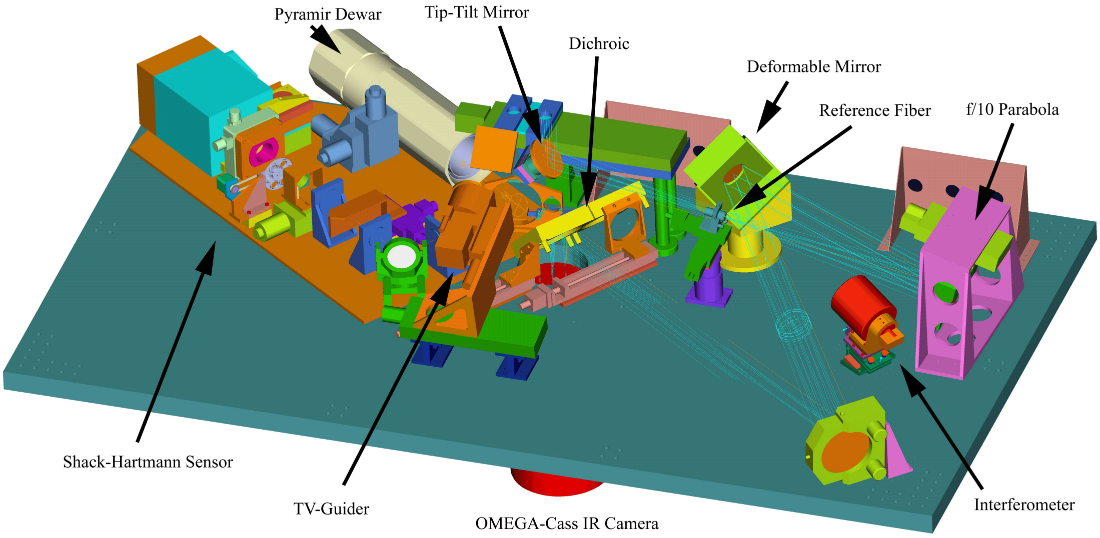

Figure 3.2: *Setup of the AO bench ALFA.*

band on the science camera.
The optical path in the ALFA-system is shown in Fig. 3.2. Coming from the telescope, the beam passes the mirror for TT-correction. The position of the telescope focus is downstream from the TT-mirror. At the telescope's F/10 focal plane a calibration fiber can be introduced into the beam. An off-axis parabola (F/10) is used to produce a collimated beam for the illumination of the deformable mirror (DM) (*Xinetics* 97 actuator).

The light is again focused by another off-axis parabola (F/25) and, then, divided into the science and WFS paths by the beam splitter of choice (see Table 3.1). In the PYRAMIR arm (Fig. 3.3) first a compensator plate compensates the static and chromatic aberrations introduced by the beam-splitter in the noncollimated beam. Then the light enters the PYRAMIR system. A warm lens doublet together with a corresponding cold doublet inside the dewar transforms the F/25 into a F/100 beam focused onto the tip of the pyramid. The tip size of the pyramid is about 20 μm and the diffraction limited point spread function (PSF) in K band has a FWHM of $\approx$ 220 μm. The wavelength of the measurement can be chosen according to Table 3.2. Additionally a spatial filter is introduced in front of the pyramid to reduce aliasing effects, to minimize the

Table 3.1: *Properties of the PYRAMIR system*

length	1.1m
diameter	0.21 m
weight	35 kg
Detector temperature	78 K
Temp. stability	$\geq$ 24h
mount	xyz-stage moved by stepper motors
step size	10μm
beam splitter	P90O10, P20O80, K/J

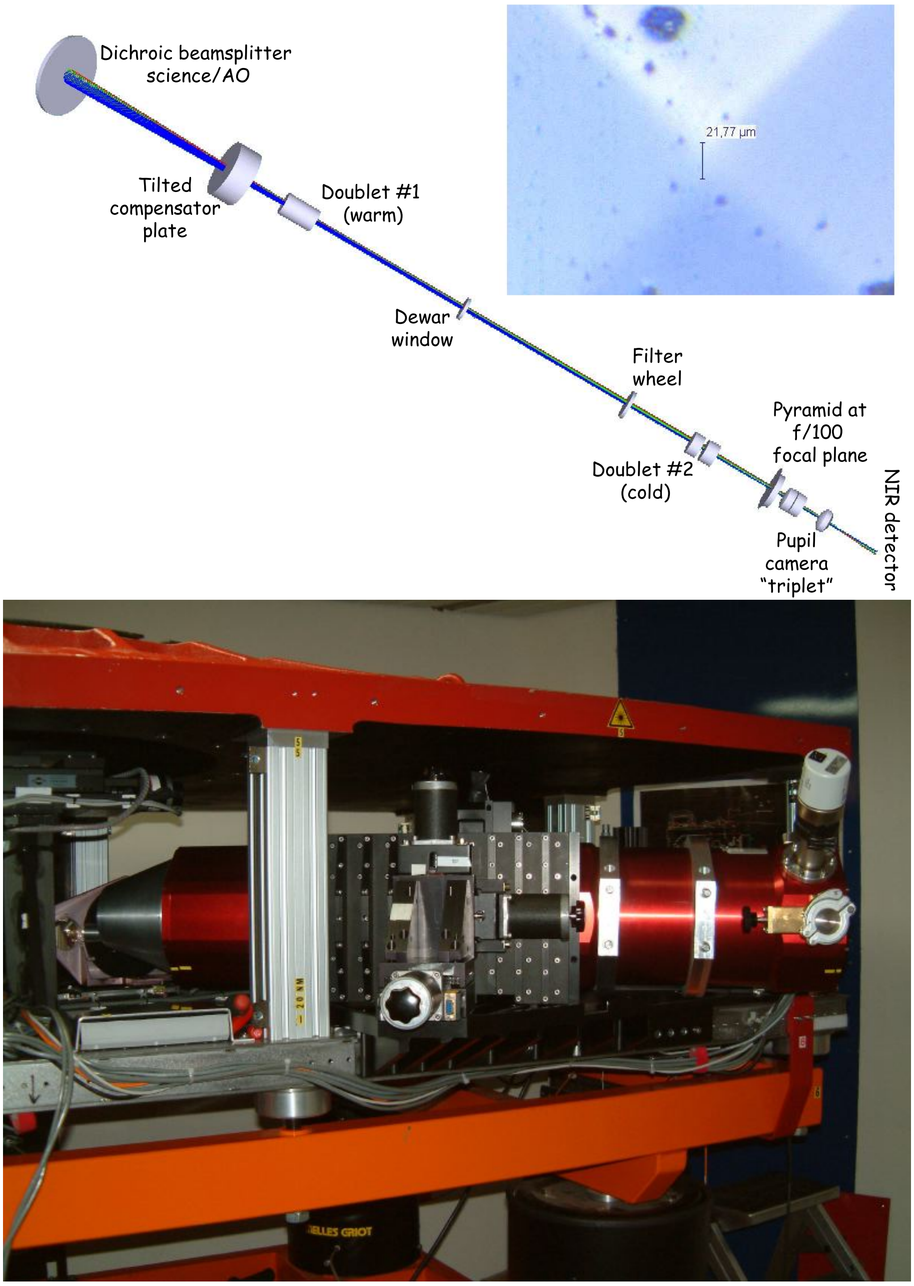

Figure 3.3: *PYRAMIR arm of the system. Upper panel: sketch of the optics, lower panel as comparison: PYRAMIR built into ALFA in the laboratory. The black structure in the middle of the image are the xyz-stages that move the dewar to position the beam on the tip of the pyramid. The warm optics sit on top of the silvery pot at the front end of the red dewar. The entrance window lies at the beginning of the dewar and the detector is placed roughly at the height of the right border of the black structure. At the rear end of the dewar one can see the pressure sensor aboce the vacuum valve.*

sky background, and to enable sensing on reasonably wide binaries. The possible sizes of this field stop are also given in Table 3.2. The final image is formed by a lens triplet onto the IR detector. The pupil diameter on the detector is about 320 μm which corresponds to 18 pixels. In order to place the detector in the pupil plane while keeping the focus on the tip of the pyramid,

Table 3.2: *Properties of the PYRAMIR camera*

Number of subapertures	224
Detector	Hawaii I
Pixel size	18 μm
maximum frame rate	$\approx$ 330 Hz
frame size	4 $\times$ 20x20 pixel
field stops	$1'', 2''$
Filters	J, H, K, $H+K$
system gain	3.8 e^-/ADU
RON	20 e^-

one can move the detector in the direction of the optical axis by about 2 mm. The details of the PYRAMIR detector are shown in Table 3.2. A description of further details of the system is given in Costa (2003).

3.1 Read Out Modes

The detector, a Rockwell Hawaii I device, can be read out with three different read out modes. Only two of these three modes are used during operation: the line interlaced read (lir) and the multiple sampling read (msr). For specifications see Table 3.3.

The lir mode is a line oriented mode with the read out pattern read-reset-read. In this mode one line is read then reset and read again. This procedure is then continued for the next line until the whole array is read. The integration time for the image is the time between the second read of one pattern and the first read of the next (see Fig. 3.4). With this scheme almost 100% of the cycle time can be used as integration time.

Table 3.3: *Read out modes of the PYRAMIR system*

name	pattern	eff. int. time	max. speed	comments
rrr	reset-read-read	50 %	165 Hz	lab use only
lir	read-reset-read	100 %	165 Hz	–
msr	reset-read-read-read-...	100 %	330 Hz	loose frame

The other read out mode, the msr mode, is frame oriented i.e. one resets the whole array, reads the whole array, reads again the whole array asf. The pattern also differs from the lir mode. First the detector is reset and then one only reads out until it is eventually reset again: reset-read-read-read-... as shown in Fig. 3.5.

The signal is accumulated and the images used are difference images between two neighboring read out frames. Thus, the images I_i are produced by resets Res_i and reads R_i as follows:

$$I_1 = R_1 - Res_1,\ I_2 = R_2 - R_1,\ I_3 = R_3 - R_2,\ I_4 = R_4 - R_3 ... \tag{3.1}$$

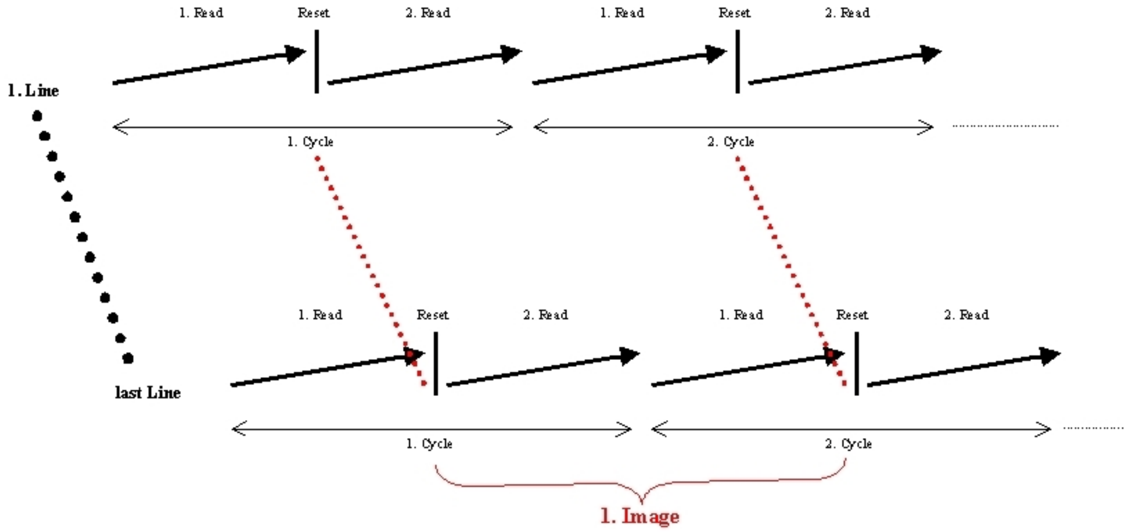

Figure 3.4: *Read out pattern for the lir mode. Each line is read, reset and read again before the next line is started. The image is built by the difference between the first frame of the second read and the second frame of the first read.*

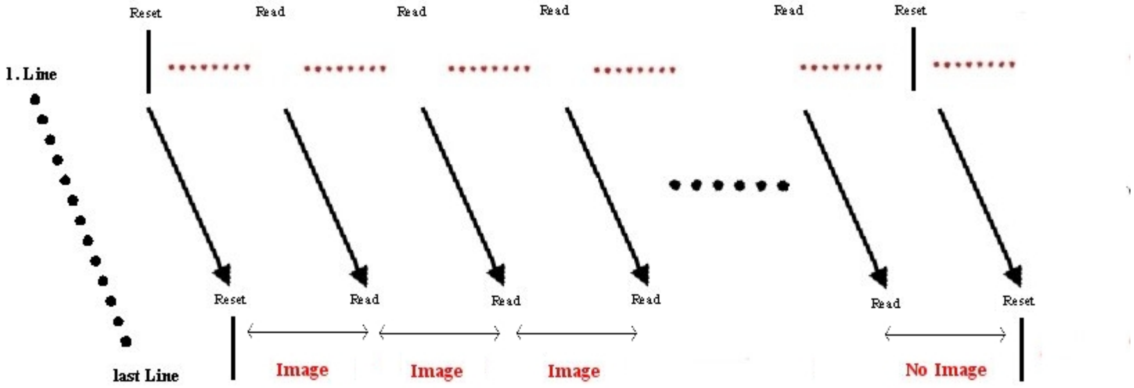

Figure 3.5: *Read out pattern for the msr mode. The first image is constructed as difference between the first read and a reset frame, the following images are built by the difference between two neighboring reads. The total signal on the detector is accumulated. The Image between the second reset and the last read is lost.*

In order not to saturate the detector while accumulating signal one has to specify a maximum number of frames. For a star of fifth magnitude at 100 Hz this maximum number is of the order of 100 frames (≈ 1s operation). The pattern runs up to the maximum frame R_n and then starts again. Two features are obvious here: first one can read out twice as fast as with the lir mode because each image needs one read only, secondly one looses the image between the last read and the reset of the following pattern $Res - R_n$. This means one performs one step with half the applied loop frequency.

3.2 Calibration

Now that we presented the most important characteristics of PYRAMIR we can start preparations for the measurement. This means we have to calibrate the system.
This calibration procedure will be described in detail in the next two subsections.

3.2.1 Tip Tilt Calibration

Because the TT-mirror is located **upstream** of the calibration light source, the TT-modes and the HO-modes are calibrated differently. For TT-calibration a 'star simulator', which mimics the light coming from the telescope is used as light source. This 'star simulator' is placed above the entrance of the ALFA system. It was originally introduced for the visible WFS and is optimized for visible light. Unfortunately in the IR we face some strong static aberrations. The basic effect is that the pupils on the detector become smaller which introduces higher noise on the measurement. However, these aberrations do not strongly affect the TT-calibration.
The 'star simulator' cannot be used at the telescope. Therefore, our TT-calibration is done in the lab only. It should be noted that care has to be taken to achieve a good TT-performance, because TT-errors in closed loop (CL) will yield low light levels in at least one of the four aperture images, thus, affecting the limiting magnitude of the system (see discussion in Sec. 2.4.4). Vice versa, a bad HO-performance will clearly affect also TT-correction, because the effectively enlarged spot size flattens the curve shown in Fig. 3.6. Because the flattening occurs in closed-loop only when during calibration a diffraction limited spot was used, TT-signals will always be measured too small and correction will, thus, be slowed down, effectively lowering the TT-bandwidth.

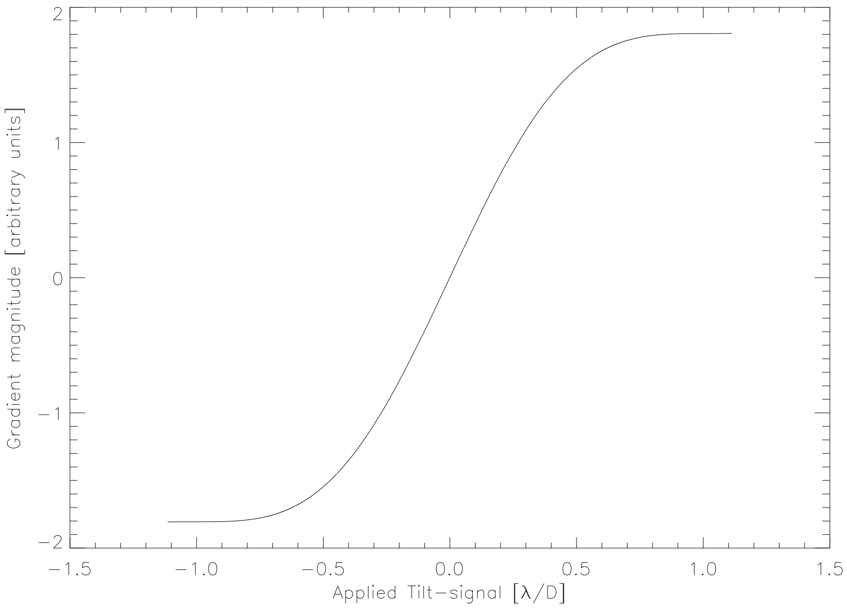

Figure 3.6: *Theoretical tilt signal. Shown is the length of the gradient versus wavefront tilt in* λ/D.

3.2.2 Phasing PYRAMIR

The HO-calibration is basically done with the usual procedure. First we shape the DM with the desired offset (dmBias) to guarantee a flat wavefront on PYRAMIR in order to get the best possible calibration. To do so, the following procedure is implemented: first the wavefront is flattened as much as possible by applying aberrations to the DM and a check of the pupil images by "eye". From this starting point a calibration of 20 modes is done. After the calibration the mode offset is put to zero (which resembles not exactly a flat wavefront but within an error of $\lambda/200$ rms (private communication with M. Feldt). With this offset we close the loop and flatten the wavefront on PYRAMIR. This is the starting point for the true calibration with the desired number of modes.

Chapter 4

Measurements of the Fundamental Restrictions

In Chapter 2 we discussed the fundamental properties of the PWFS system that can strongly influence the performance of the system. In this chapter we present measurements of the effects of these error sources for the PYRAMIR system and show the best way to manage them. Most effects will go into one of the following errors: Measurement error σ^2_{meas}, Aliasing error σ^2_{alias} and cross talk error σ^2_{cross}. Measurement error and cross talk we have already encountered. Aliasing will be discussed in Chapter 4.6. To give an idea for the moment what aliasing is, imagine we have a system that samples the pupil with spatial frequency f. Any mode with higher spatial frequency will not only not be measured it will be mistaken as a mode with lower spatial frequency leading to an erroneous signal.
the two exceptions that will not explicitly enter the discussion of the error budged of the system are the impact of the pyramid edges and the flatness of the pupil illumination. These two effects yield systematic errors that will be treated separately.
All the measurements presented in this chapter were performed during open loop operation. However, they can be used to quantify the performance of the system during CL operation. This will be done in Chapter 4.6.

4.1 Impact of the Pyramid Edges

In Sec. 2.4.1 we saw that the diffraction at the edges of the pyramid and the light loss due to the finite size of the edges can significantly reduce the amount of useful signal for the measurement.

In Fig. 4.1 we compare the measurements of the light diffracted from the edges (crosses) versus the amplitude of the mirror eigen modes applied to the DM with predictions of simulations (solid and dashed curves). The measurement are averaged over the modes 0-4. The dashed curve shows the effect of diffraction only. We measured the total amount of light on the detector and the amount inside the pupils. For a (nearly) perfect wavefront the measurement matches the simulation. Of course it is not possible to deduce from this measurement the ultimate cause of the light ending up outside of the pupil images. However, it is clear that apart from the regime of very good wavefronts, we suffer additional losses that cannot be explained by diffraction alone. From microscopic measurements we know that the finite edge of the prism is at least in one direction more than 20 μm across. A simple calculation assuming all light falling on an edge of this size to be scattered out of the pupils additionally to diffraction yields the solid curve in Fig. 4.1. It appears that scattering on other optical elements is

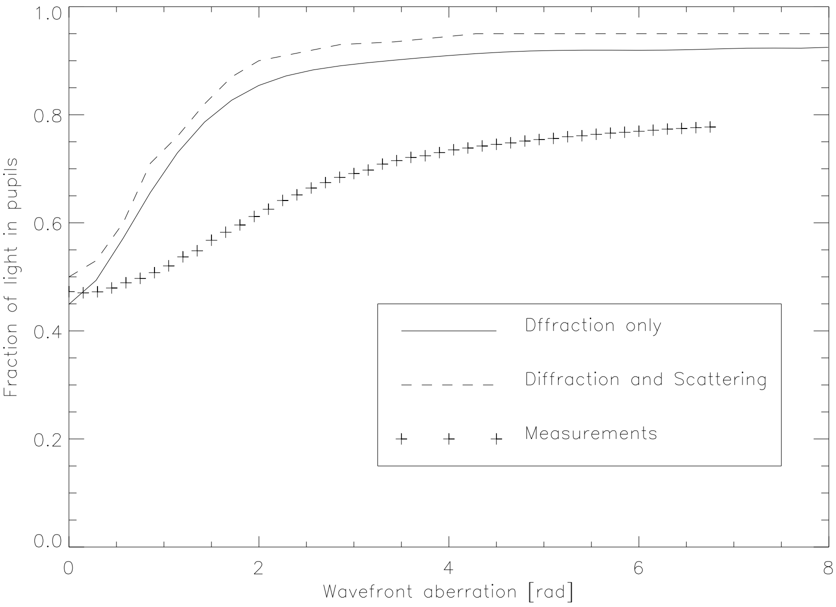

Figure 4.1: *Light 'lost' due to the effect of the pyramid edges. The dashed curve is the simulated 'loss' due to diffraction only. The solid curve includes the effect of light lost due to finite edge sizes of 22 μm. The crosses mark the measurements averaged over the first 5 eigen modes of the DM.*

non-negligible for our system in the case of moderately well to badly-corrected wavefronts.

4.2 Pupil Illumination Flatness

In Section 2.4.5 we emphasized the importance of a well illuminated pupil.
The original fiber in use for PYRAMIR (fiber 1 in Table 4.1) has a FWHM of the beam in the **pupil** plane of less than the pupil diameter (18 pixel). To provide a more equal illumination one can try two things: Use a fiber with a higher numerical aperture (NA) or try a fiber with a larger core, i.e., a multi-mode (MM) fiber. A MM fiber that produces a much more uniform illumination has a much larger core diameter and might, therefore, be resolved by the sensor. Indeed this happens in the case when PYRAMIR is illuminated by fiber 2 in Table 4.1. The result should have a similar effect as modulation of the pyramid during calibration: The linear regime becomes larger but the sensitivity drops. A change in the fiber between calibration and measurement should reveal this fact.
In the case of PYRAMIR we have the choice of three different fibers with the characteristics shown in Table 4.1. The FWHM mentioned there is the width of the illumination in the pupil plane, **not** the focal plane. Note that the pupil diameter is 18 pixel. The multimode fiber can be resolved by PYRAMIR: The entrance beam from the fiber has a F/10 optics, the PYRAMIR output a F/100. In K band the cor of the fiber must, therefore, be smaller than 22μm in order not to be resolved.
In the following we will address two important questions:

1. What is the effect of a resolved fiber or a Gaussian illumination on the on-sky performance

Table 4.1: *Properties of the fibers in use.*

Fiber	core diameter	NA	cut off (λ)	FWHM in K
1	9.5 μm	0.13	1400	16 pixel
2	50 μm	0.22	-	$>>$ 18 pixel
3	4.0 μm	0.35	-	$>$ 18 pixel

of the system ?

2. How does an extended light source during the measurement only effect the performance of the system ?

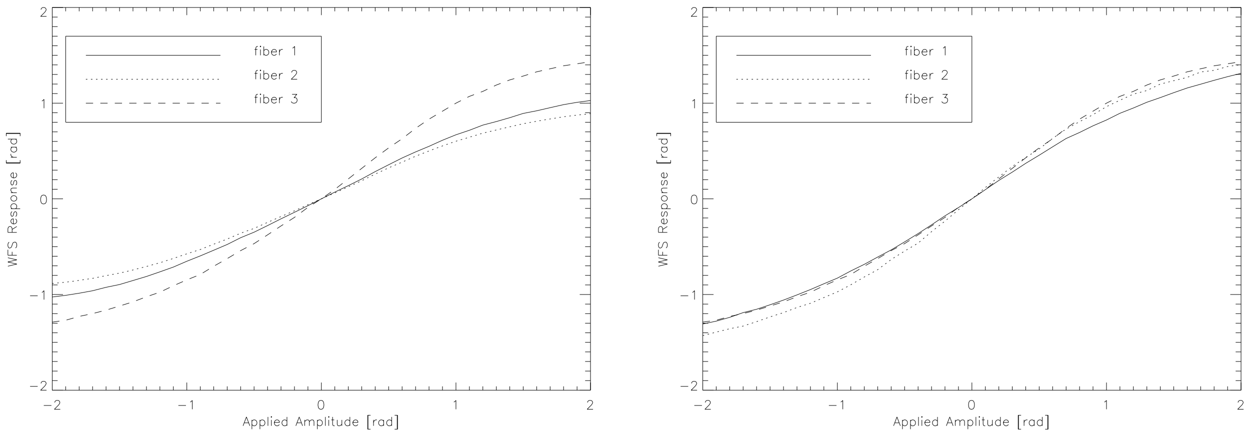

Figure 4.2: *Left: effect of different illuminations during calibration. The figure shows the linear regimes after changing the fiber between calibration and measurement. During measurement the pupil was illuminated by fiber 3. The dashed curve corresponds to the response with fiber 3, the solid curve to fiber 2 and the dotted curve to fiber 1. The sensitivity is reduced in the case of a calibration with fiber 1 and 2.*

Right: response of the system with an extended target as light source (fiber 2). The response of the system is almost independent of the fiber used for calibration.

Fig. 4.2, left panel, addresses question 1. There the response of the system for different illuminations during calibration is shown. The fiber with high NA (fiber 3) was used as light source during measurement because of the three fibers it best resembles a point source. The sensitivity after a calibration with fiber 1 or 2 is reduced with respect to the calibration with fiber 3 the 'true' point source. This shows that an extended calibration fiber, as well as a Gaussian illumination during calibration reduce the sensitivity of the system.

The effect of an extended object as target during measurement is shown in Fig. 4.2, right panel. The response of the system is slightly better for a calibration with the MM fiber than for the other two cases but the difference is much smaller than in Fig. 4.2. Therefore a calibration with a perfect point source and a flat illumination of the pupil during calibration will be the best choice even for the use of an extended object as target for the CL operation.

4.3 Read Out Noise

A very important and fundamental source of reduced performance for a wavefront sensor is the RON as has been widely discussed in Section 2.4.3. The special importance of this error source for our application arises from the fact that infrared detectors have large RON in comparison to CCDs. In the regime of faint stars the RON will be the main source of noise on the measurement and, thus, set a lower limit to the flux a guide star must have. The effect of the RON has been derived quantitatively in Chapter 2.4.3, Eqs. 2.21 and 2.22.

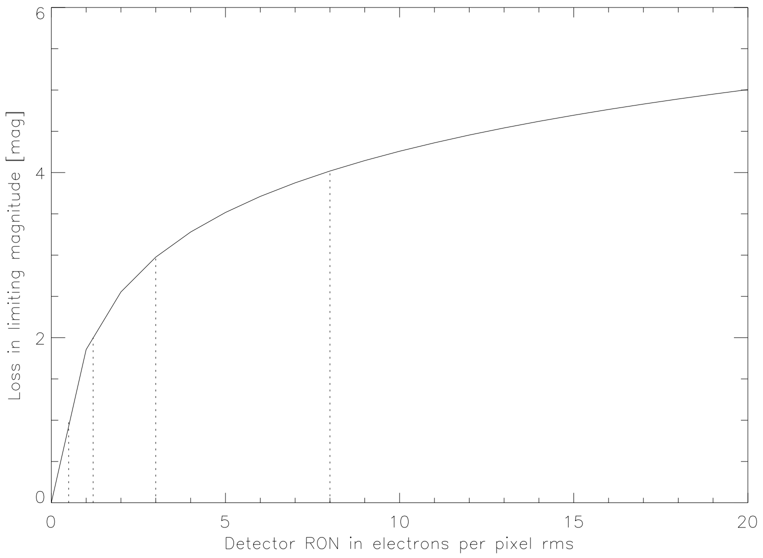

Figure 4.3: *Loss in limiting magnitude due to RON. The dotted lines mark the losses in 1, 2, 3, and 4 mag. At the position of PYRAMIR with 20 e^- RON we lose 5 mag.*

On the sky we have shown PYRAMIR to operate well down to S/N ratios of 0.4 per subaperture (Peter 2008). Taking this value as limit, the loss in limiting magnitude for a fixed Strehl ratio is shown in Fig. 4.3. So for 1 e^- noise only, we already loose about 1.5 mag. At our level of 20 e^-

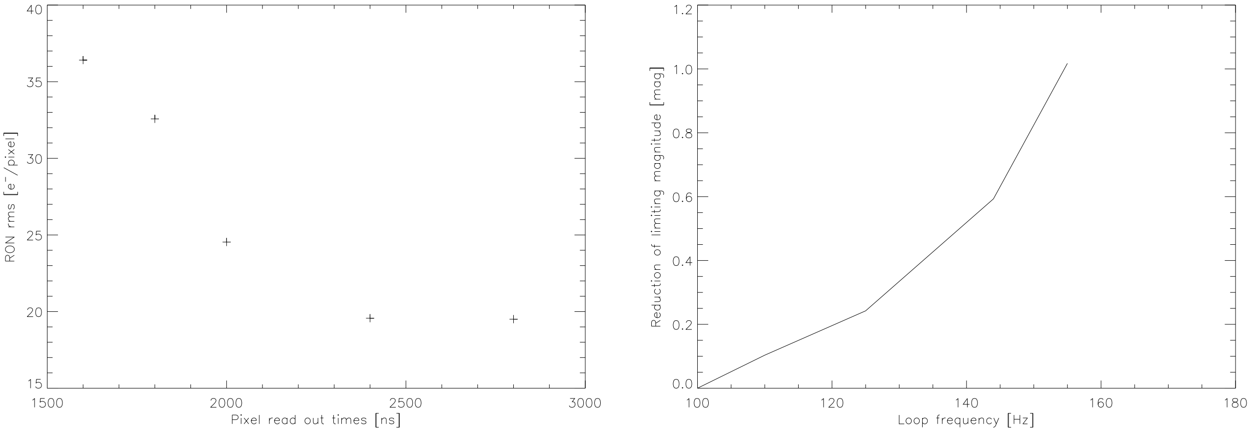

Figure 4.4: *Left: dependence of the RON on the pixel-read times on the detector.*
Right: limiting magnitude effected by loop speed and RON compared to the 'standard' 100 Hz loop.

the loss is 5 mag.
Infrared detectors have also the disadvantage of a slow read out compared to CCDs. Therefore they strongly limit the bandwidth of the correction loop.
One possibility to increase the read out speed is to reduce the pixel-read times. In our case this increases the combined noise of detector and read out electronics.

In Fig. 4.4, left panel, we show the dependence of the RON measured with the PYRAMIR detector in on the pixel-read times. The limit for 'slow' read out is $20e^-$. With decreasing pixel-read time it strongly rises. If we increase the loop bandwidth by decreasing the pixel-read times the limiting magnitude is reduced by the combination of faster loop speed and increase in noise. Fig. 4.4, right panel, shows this combined effect.

4.4 Centering on the Pyramid Tip

In Sec. 2.4.4 we explained how a decenter of the beam on the pyramid tip can enlarge the measurement error of the system and, thus, reduce its limiting magnitude.
In the case of PYRAMIR, the beam is centered onto the pyramid tip during calibration via motorized xyz-stages. Due to the finite step size of these stages, the beam is not perfectly centered on the tip of the pyramid during HO-calibration. When the software ignores this fact, as was the case during our early runs, the beam will have the same decenter during CL operation. This decenter was measured to be small in one direction but about 40 μm in the other. In Fig. 4.5, left panel, we present the effect on the reconstruction matrix R. The trace of RR^T that enters the measurement error is plotted versus the strength of the displacement. The working point of PYRAMIR is marked. The effect on the noise of the gradients is shown

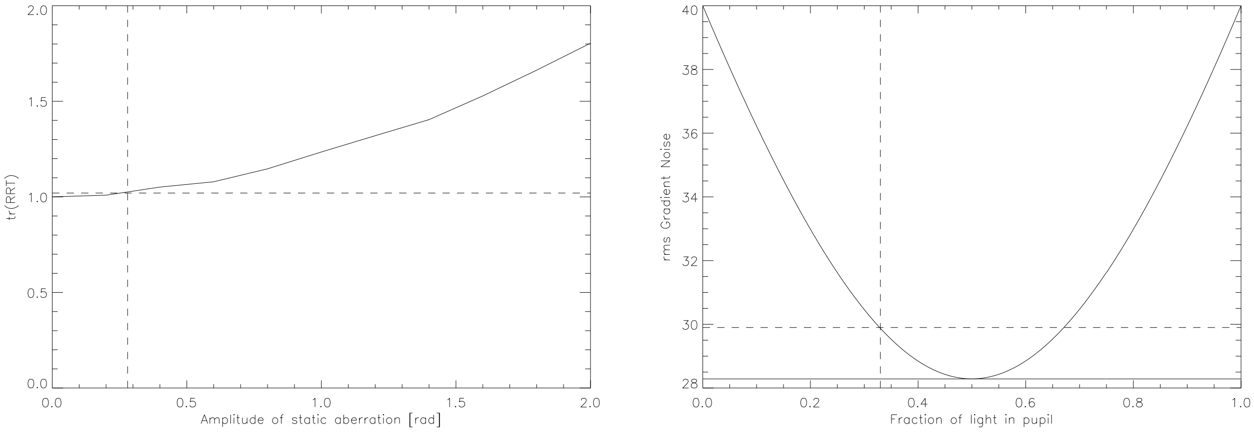

Figure 4.5: *Left panel: dependence of $tr(RR^T)$ on the amplitude of static aberrations. The solid line shows the dependence averaged over different modes, the dashed lines mark the value for our application. In the case of a displacement of the dewar 0.1 rad aberration correspond to $\approx 14.2\mu$m displacement. Right panel: effect of a displacement of PYRAMIR wrt. the optical axis on the gradients. The figure shows the dependence of the rms noise of the gradients on the fraction of light in one of the pupils for a simplified model of a roof prism. The dashed line marks the momentary working point of PYRAMIR.*

in Fig. 4.5, right panel. Here we show the increase in noise per gradient versus the fraction of light in two neighboring pupils for TT-motion. This was calculated here with the use of a simplified model (a roof prism). In our case the noise on the gradients increases from 28.2 to 29.9 that corresponds to an increase in detector noise from 20 e^- per pixel to 21.1 e^- per pixel. Both effects together reduce the limiting magnitude by 0.13 mag. So the decenter of the beam is not a crucial point for the performance.

4.5 Noncommon-path Aberrations

In Section 2.4.6 we laid out why investigations into the effect of noncommon-path aberrations and a way to deal with them is essential. In the following we look into the dependence of two of the three most important properties of PYRAMIR on these static aberrations: The regime of linear response and the modal cross talk.

Before we csn describe the series of measurements we performed to characterize the behavior of the sensor under various conditions, we have to explain how a measurement is actually laid out:

Before we can start to measure we have to calibrate the system, i.e., apply modes to the DM and measure the gradient pattern on the sensor. These measurements give us the interaction matrix, i.e., gradients for modes. Then the (pseudo)inverse of the interaction matrix is calculated which is called the reconstruction matrix.

A "measurement" is now done simply by multiplying the measured interaction matrix with a reconstruction matrix, where the latter is possibly taken under different circumstances, e.g. with different static aberrations applied.

Further on the measurements showed that there is only a marginal difference regarding the important properties of the sensor, e.g. linear regime etc., between the use of the gradients that are measured directly and the mode coefficients that are calculated using the reconstruction matrix of the system. Therefore, in the following, we will exclusively use the mode coefficients for characterization.

4.5.1 Different Mode Sets

As we discussed in Sec. 2.4.6 the mode set of choice to use on-sky has a strong influence on the cross talk of the system. In order to get a preselection of the most appropriate set of modes for the sensor we performed an extensive series of measurements (Dorner 2006). Three different sets of modes were under examination in simulation: Normalized Karhunen-Loève (KL) modes, eigen modes of the DM and eigen modes of the PYRAMIR system. The correction of atmospheric aberrations with these modes were examined in a simulation. This simulation showed that the PYRAMIR eigen modes are a bad choice for CL operation. The reason is that one needs a high number of these modes to construct even low-order atmospheric modes. The other two mode sets were similar in their performance. Due to the fact that the eigen modes of the DM yield lower condition numbers we planned to use those for CL correction. Nevertheless the effect of static aberrations and the linear regime of the sensor was measured for both mode

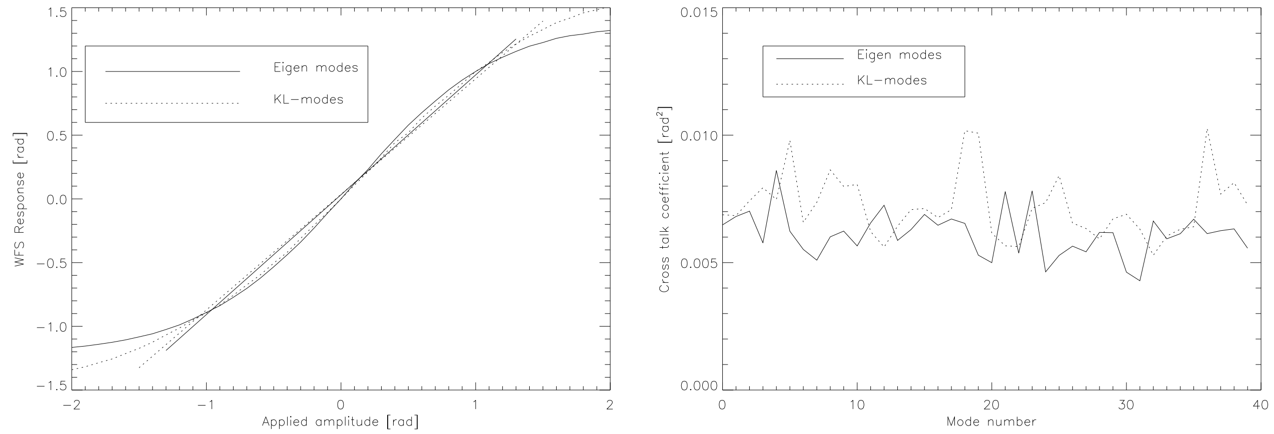

Figure 4.6: *Left: linear regime without static aberrations for DM eigen modes (solid line) and KL modes (dotted line). Shown is the linear regime averaged over 40 modes. The linear fit is done with a* χ^2 *of 0.1. The linear regime of the KL modes is 15% larger than that of the eigen modes.*
Right: modal cross talk averaged over all modes and amplitudes for each applied mode from -2 to +2 rad*. The dotted line belongs to the KL modes, the solid line to the eigen modes of the DM.*

sets, the DM eigen modes and KL modes. The amplitude of calibration varied between -2 and +2 rad (in exceptional cases from -4 to +4 rad) in steps of 0.1 rad in K band. Several static aberrations were applied with amplitudes ranging from 0 to +2 rad rms in steps of 0.2 rad. From this characterization we will find the best mode set to characterize the sensor's dependence on static aberrations.

Here we compare the response of the system for the two different mode sets. Both sets are normalized to a rms of 1 rad in K band of the wavefront. The criteria for comparison are linear regime and modal cross talk. The linear regime is the regime in that we can perform a linear fit to the data with a χ^2 of 0.1 or better. The modal cross talk is the residual rms of the wavefront after subtraction of the ideal response. Fig. 4.6, left panel, shows the linear regime averaged over 40 modes for both sets.

Surprisingly, the KL functions have a larger linear range than the eigen modes. Additionally averaged over the whole range of calibration amplitudes from -2 to +2 rad both mode sets have the same modal cross talk (see Fig. 4.6, right panel).

However, there are some modes in the set of KL functions that naturally yield a high modal cross talk with others. The future task will be to optimize the mode set further in order to minimize the total modal cross talk of the entire set of basis functions and still have an acceptable performance on sky.

In the following, for laboratory purposes, we used the eigen modes unless stated otherwise. The reason for this choice is that the smaller linear regime helps to see the effects of static aberrations better.

4.5.2 The Linear Regime and Modal Cross Talk under the Influence of Static Aberrations

In the last section we discussed the linear regime and cross talk in the absence of static aberrations (statics). But these aberrations are ever present in any AO-system at least to some extent. So in this subsection we will discuss the measurements of the system's behavior under statics. In order to keep things simple and still see the general properties, static aberrations will be represented by one single mode with variable strength.

There are differences of the effect of the static modes depending on if they are applied during calibration only, measurement only or both.

1. Static aberration during calibration only: This case is rather of academic interest.

In this case one would expect little effect on the modes without statics during the measurement as long as the static mode is within the linear regime. If it is beyond the linear range there will be enhanced modal cross talk. The exception is the mode with a static part. If the total amplitude of this mode exceeds the linear range then the response curve during measurement should become less steep because during calibration the applied modes will be underestimated.

2. Static aberration during measurement only: This will happen if one wants to have the best possible calibration and a perfect science image, moving the noncommon-path aberrations entirely into the sensor path during observation only.

Here one would expect little effect on the modes without static pattern unless the strength of the static mode is beyond the linear range. For the modes with static pattern the center of the response curve will be shifted. The amount of the shift should be just the amplitude of the static mode. Additionally one would expect the modal cross talk to increase.

3. Same static aberrations during calibration and measurement: This will be the case if we flatten the wavefront on the science detector and start calibration afterward.

Here we will expect little effect on the modes without static pattern as long as the static mode stays inside the linear range. The modes with static parts will differ only slightly in the direction of the calibration amplitude. When the signal has amplitude either 0 or equal to the calibration amplitude, the response for the mode will be equal to the optimum response. In between the difference will not be large. In the other direction the measured response will diverge from the curve of optimum response. This divergence will depend on the strength of the static mode and the calibration amplitude. If those have for instance opposite sign then we will calibrate in the linear range and end up with the case of statics during measurement only. When they have the same sign, we will have a similar behavior as statics during calibration only and thus an underestimation of the amplitude in this direction.

After this short discussion of the expectations we will compare the theoretical considerations with the actual measurements. Fig. 4.7 shows the averaged linear regime for the three cases in comparison with the ideal case. The calibration amplitude was 1 rad, the static aberrations are applied with amplitude 0, 1, and 2 rad. Only in the case of the strongest static aberration during measurement only the response differs significantly from the other curves. This finding matches the expectations quite well. The divergence arises from the mode with static part as we will see in the following.

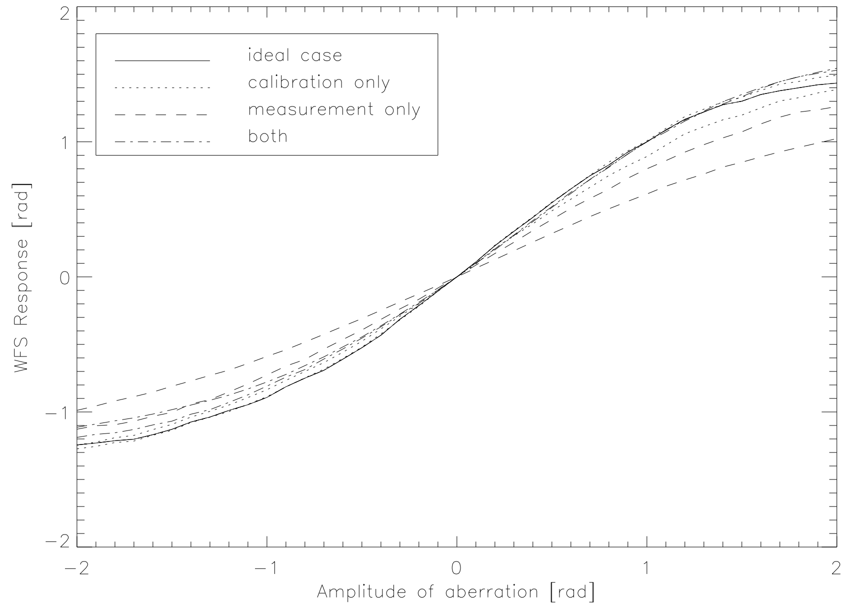

Figure 4.7: *Linear regime of PYRAMIR in K. The linear regime is averaged over all modes. The static aberration amplitude is +1 and +2 rad. Shown are the ideal case without aberration (solid line), statics during calibration only (dotted line), statics during measurement only (dashed line) and statics during the whole process (dash-dotted line). The divergence from the ideal case goes with the strength of the static aberration. Only the dashed and dotted curves in the case of +2 rad static aberration differ significantly from the ideal case.*

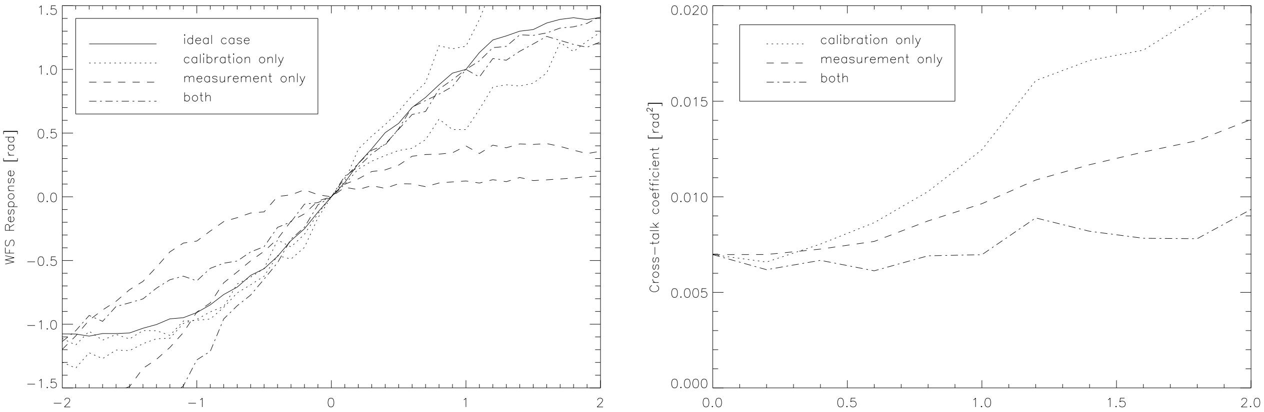

Figure 4.8: *Left: response of the mode with static aberration is shown. The line styles are the same as in Fig. 4.7. The difference between the cases can be seen clearly. Here again the strength of divergence from the ideal case goes with the strength of the statics. The case closest to the ideal one is that with static aberrations during the entire procedure.*
Right: modal cross talk coefficient averaged for all applied amplitudes from -2 to +2 rad versus amplitude of static aberration. The higher the amplitude the stronger the modal cross talk In the case of the same static aberration during calibration and measurement the modal cross talk is rising only very slightly.

The response of the special mode with static part is shown in Fig. 4.8, left panel.

All curves differ from the ideal case exactly as expected. However, the response of the system with statics applied during both, calibration and measurement, is closest to the ideal case. This property should also have an effect on the modal cross talk between the modes as we will show immediately.
In Fig. 4.8, right panel, the dependence of the averaged modal cross talk coefficient of the system on the amplitude of the static aberration is shown. It rises as expected for the cases with static aberration during measurement or calibration only. In the case of statics during both the modal cross talk is nearly independent of the static mode. Therefore, we can conclude that in the case of noncommon-path aberrations and the aim for a perfect science image it is best to move the aberrations all into the sensor path before calibrating the system.
The real noncommon-path aberrations for the system were measured to be maximum 0.4 rad rms for a single mode or added quadratically for all modes around 0.6 rad in K. Thus one is still in the linear regime (see Fig. 4.6) of PYRAMIR and comparing these numbers with our result from above (see Fig. 4.8) we see that we can happily use this shape of the DM (dmBias) as starting point for calibration and measurement.
An even better way to treat the noncommon-path aberrations would be to use two different calibrations: One calibration with positive amplitude and one with negative. Then in CL the modes with positive and negative amplitudes will be corrected by the corresponding reconstruction. This should reduce the errors on the modes with a static part significantly. However, up to now this scheme did not run stably on the sky. Therefore in the following we will always use the same statics during calibration and measurement and one calibration only.

4.5.3 Dependence on the Strength of Static Aberrations

Imagine we want to construct an AO-system including science camera. In the planning we have to estimate how strong the noncommon-path aberrations will be.

To enable us to place some tolerances on the design of the system we have to measure how the system performance in particular the error budged of the system depends on the strength of the static aberrations. Thus, in the following we will discuss the measurements of the dependence of the measurement error σ^2_{meas}, the aliasing error σ^2_{alias} and the cross talk error σ^2_{cross} on the strength of the static aberrations.
We have already seen in Section 2.4.4 that the measurement error depends linearly on the strength of the static aberration. This dependence, however, is small. In Section 4.5.2, Fig. 4.8, right panel, we showed that there is no dependence on the averaged modal cross talk on the statics. The same is true for the aliasing: Fig. 4.9 shows the dependence of the aliasing coefficient on static aberrations up to a strength of +2 rad. The response is averaged over all numbers of calibrated modes. Note that this dependence will be different when the static mode is only present during closed loop.

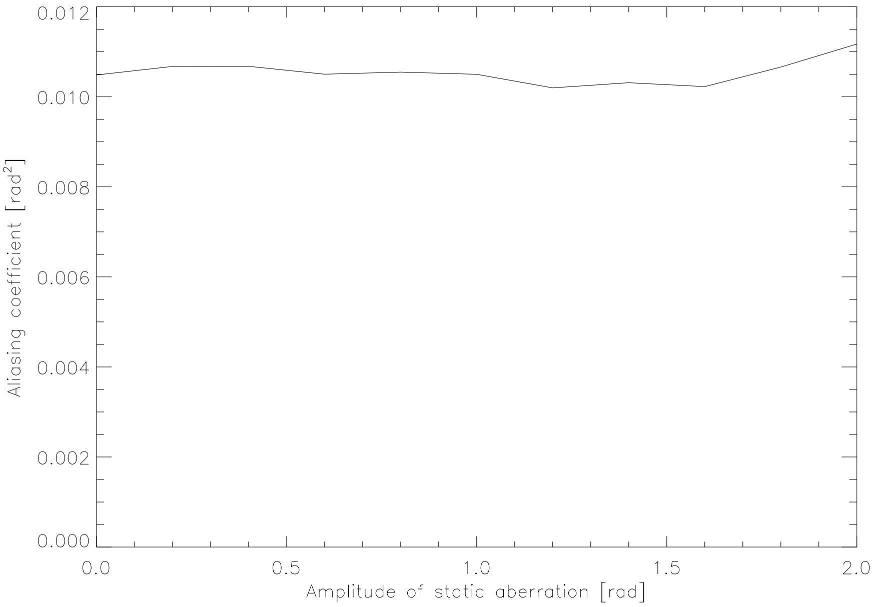

Figure 4.9: *Dependence of the aliasing coefficient on the strength of the static aberration.*

4.5.4 Dependence on the Calibration Amplitude

Up to now we measured the potential influence of error sources in the system itself. But we have also to determine the specifications of the calibration procedure. In Sec. 4.5.1 we already showed the influence of the modal basis has on the error budged of the system. Here we investigate into the dependence of relative modal cross talk, aliasing and the measurement error on the amplitude of calibration.

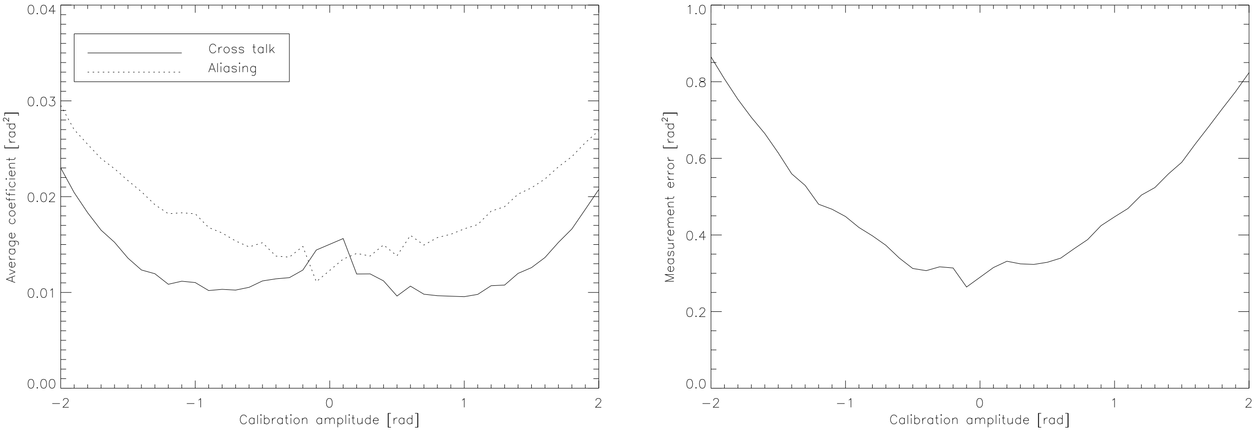

Figure 4.10: *Left: average modal cross talk (solid line) and aliasing (dotted line) coefficient for 20 calibrated modes in dependence on the amplitude of calibration.*
Right: same as the left panel but for the measurement error in the case of S/N=1.

For small calibration amplitudes the strength of the mode signal is comparable to the noise on the detector and we, therefore, expect the errors to decrease with rising calibration amplitude at least within the linear regime. Outside the border of the linear range the errors will increase again because of a rising nonorthogonality of the modes.

Fig. 4.10, left panel, shows the dependence of the modal cross talk and aliasing coefficients on the amplitude of calibration. The expectations are matched quite well. The modal cross talk is high for small calibration amplitudes and drops toward the border of the linear regime at about 1.2 rad, then it rises again. The aliasing error rises almost parabolic with calibration amplitude but stays within 10% difference in the linear regime. The measurement error is almost constant within the regime of -0.6 to +0.6 rad and then rising more steeply as shown in Fig. 4.10, right panel. Therefore we conclude that a calibration amplitude of about 0.6 rad will minimize the total reconstruction error.

4.6 The Effect of the Errors in Closed Loop Operation

After we measured the different ingredients of the error budged under various conditions one general question arises: How many modes are appropriate to calibrate to achieve a specific performance? We will see that from the dependence of the total residual wavefront error on the number of calibrated modes. There are several errors that depend on this number:

1. The modal cross talk between the calibrated modes σ^2_{cross}
2. Aliasing σ^2_{alias}
3. The measurement error σ^2_{meas}
4. The temporal error σ^2_{temp}
5. The fitting error σ^2_{fit}.

Before solving the total problem we have to investigate into the nature of the single errors. To derive these we have to take the strength of the atmospheric modes as given by Eq. 2.9: The equation describes the residual wavefront error after a perfect correction of the first N modes. Thus, the difference between the results for N+1 and N modes describes the error connected to mode N alone. Also we have to include the correction of the modes in CL operation. This is the point where the temporal error comes in during this investigation, because the band width of the modes increases with mode number.
Modal cross talk and aliasing:
In the literature there is some confusion about these effects so we will state here what we mean with we use these expressions. In fact both are quite similar effects but not identical. As already mentioned in the beginning of the last chapter aliasing describes HO-modes that turn up as lower order modes. We will explain the specific difference in an example: Imagine that we calibrated the system with the first 40 modes of the mode set of choice. The modes we did not calibrate (41+) will give erroneous signals on the calibrated modes. These signals will be referred to as 'aliasing'.

Modal cross talk, however, arises between modes we calibrated. Imagine that the arriving wavefront has no other aberration than focus of some amplitude. PYRAMIR, however, will measure not only focus (possibly with a different amplitude) but also some other modes. The mean square error of the difference between the real aberration and the measured one yields then the cross talk error.

The important point why we discuss the two effects so deeply is that in contrast to aliasing the amplitude of the modes that cause cross talk is strongly reduced during CL operation. The reason is that these modes were calibrated and are corrected during CL-operation. So the amplitude of the modes themselves shrinks. The amplitude of the cross talk is correlated to the amplitude of the modes. Thus, the cross talk is also reduced. Obviously this is not the case for the amplitude of the modes that cause the aliasing.

The aliasing error strongly depends on the geometry of the system. For a PWFS it is proposed to be much smaller than for the SHS (see Verinaud 2004). Here we have measured the aliasing for calibrations of 2 modes to 39 HO-modes. Due to the fact that our measurements have been performed for 40 modes we can only use the residual 38 modes to 1 mode respectively that are not calibrated to derive the aliasing error.

Fig.4.11, left panel, shows the dependence of the average aliasing error coefficient E^2 on the number of modes calibrated in the system. The coefficient decreases with the number of calibrated modes for up to 10 modes then stays constant and then drops again after approximately 30 modes. These drops are conected to the fact that the number of contributions to the averaging is small. So for our purposes we will assume that the behaviour of the coefficient between 10 and 30 modes is typical and it is sufficient to assume the coefficient to be constant for all calibrations without making a too large mistake. To derive the total aliasing error on sky we still have to account for the modes not measured in the lab (No. 41 and so on). To include these we just assumed the aliasing coefficient to be constant for all modes. We then only had to weight every mode with its strength on-sky. We can derive the total error due to aliasing for N calibrated modes from:

$$\sigma^2_{alias} = \sum_{i=N+1}^{\infty} < a_i^{\perp T} R^T R a_i^{\perp} > \tag{4.1}$$

Here $a_i^{\perp}$ denotes the mode vector orthogonal to the set of calibrated modes and R the reconstruction matrix. If we use the formula (Eq. 2.9) for the fitting error to account for the total strength of each mode and the assumption of a constant coefficient E^2 we can explicitly write down the error in dependence on the number of modes N we calibrated:

$$\sigma^2_{alias} \propto 0.3 \left(\frac{D}{r_0}\right)^{\frac{5}{3}} E^2 N^{\frac{2-\sqrt{3}}{2}} \tag{4.2}$$

The error is rising slowly with the number of calibrated modes.

The modal cross talk of the modes does not only depend on the system geometry but also on the mode set chosen for calibration. The set should be close to the KL modes. The reason is that the strength of these modes falls off as quickly as $\approx N_m^{-(\sqrt{3}+2)/2}$ with mode number and one does not want to lose the advantage of a good correction with a relatively low number of modes. For the higher order modes this is not so crucial because the fall off becomes almost

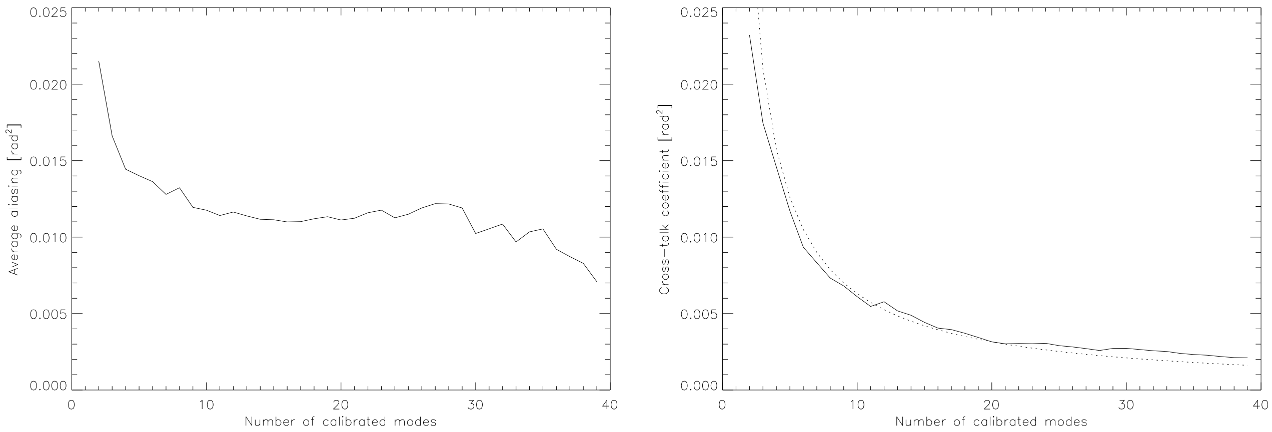

Figure 4.11: *Left: development of the average aliasing coefficient with the number of calibrated HO-modes. First it drops steeply then stays almost constant.*
Right: dependence of the averaged modal cross talk coefficient on the number of modes (solid line). The dotted line is a x^{-1} *profile.*

flat. But still we have a bit of freedom here to reduce the total amount of modal cross talk for a given system by the optimization of the mode set.
In general the formula for modal cross talk is given by:

$$\sigma^2_{cross} = \sum_{i=1}^{N} < a_i^T R^T R a_i > \tag{4.3}$$

Fig.4.11, right panel, shows that the averaged modal cross talk coefficient falls off with the number of calibrated modes. The best fit with a simple model yields a dependence for N calibrated modes of N^{-1} as can be seen in Fig.4.12. If we again include the atmospheric weighting as done for the aliasing error the total measured error due to modal cross talk in open loop can be derived to be:

$$\sigma^2_{cross} \propto 0.3 \left(\frac{D}{r_0}\right)^{\frac{5}{3}} E_0'^2 (1 - N^{-\frac{\sqrt{3}}{2}}) \tag{4.4}$$

Here $E_0'^2$ denotes the error for one calibrated mode only. Therefore the modal cross talk will become independent of the number of modes for a higher number of calibrated modes. The additional benefit here, as already discussed, is also that the strength of the modal cross talk will be strongly reduced when we close the loop because only the residuals of the corrected modes will give rise to modal cross talk.
To find the best number of modes to be calibrated we have to include the measurement error given by Eq. 2.4.4 as well. The dependence of the trace of $R^T R$ on the number of calibrated modes is shown in Fig.4.12. This trace is the sum over the squares of the entries of the reconstruction matrix. Therefore a perfect linear dependence will arise from a diagonal matrix $R^T R$. Modal cross talk is the reason for any departure from this behavior. The departure is, however, very small. Thus we can write the dependence as

$$\sigma^2_{meas} \propto N \tag{4.5}$$

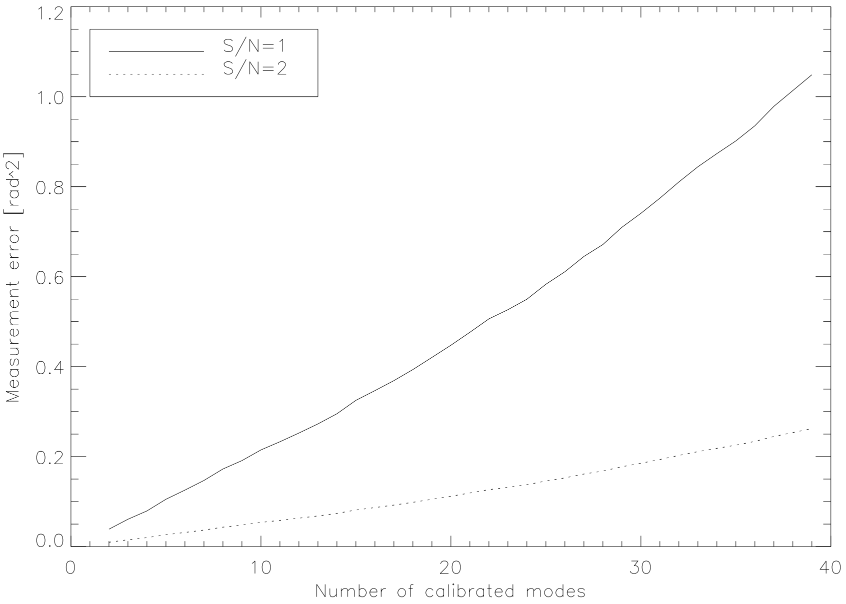

Figure 4.12: *Dependence of the measurement error on the number of calibrated modes for two values of S/N in the subapertures. The solid line denotes a S/N of 1 the dotted line a S/N of 2.*

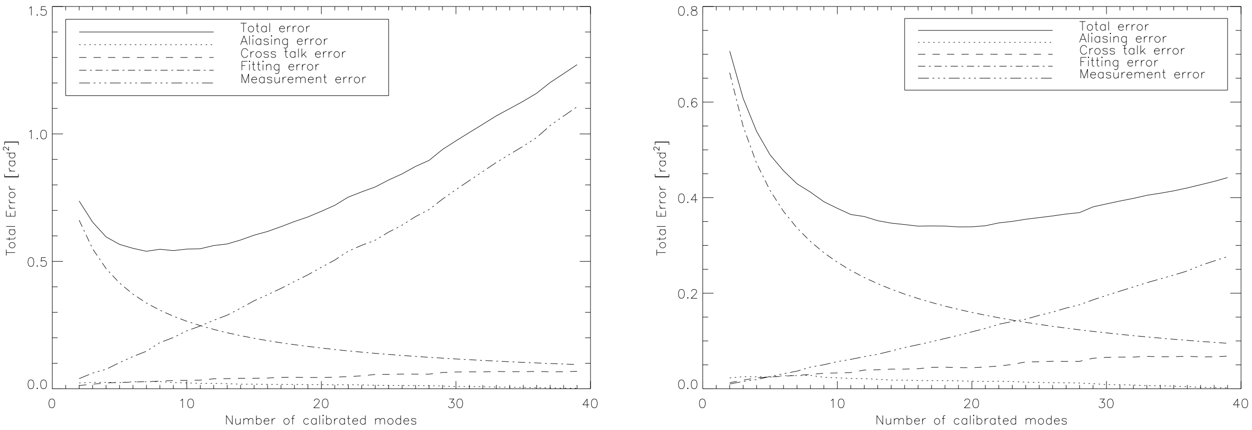

Figure 4.13: *Dependence of the different errors on the number of calibrated modes. Left panel: S/N = 1, right panel: S/N = 2. The dotted line shows the aliasing error, the triple dot-dashed lines the measurement error, the dash-dotted line the fitting error, and the solid lines the total error. The cross talk is below the aliasing error and cannot be seen on this plot.*

Fig.4.13 compares all the errors in open loop we derived. The aliasing and modal cross talk are of the same order and quite small. The measurement error is shown for S/N=1,2. For S/N=1 the measurement error matches the fitting error at 8 calibrated modes. The point of best correction (minimum of solid curve) is at 5 modes. For a S/N of 2 the largest contribution arises from the fitting error up to 16 modes. The best correction is given for a number of 13 calibrated modes. This curves are very helpful because we are able to change the number of modes we use for reconstruction on the fly, adapting to the actual situation.

Chapter 5

Modeling the On-sky Performance

Since our ultimate goal in this work is to compare the on-sky performance of a PWFS working under closed-loop, high-Strehl conditions to that of a conventional SHS, we face a rather tricky problem: since ALFA is no longer equipped with a SHS, we need to compare to other, existing AO systems with SHSs. One of the best described systems here is NAOS at the VLT Rousset et al. (2003). Since the two systems obviously didn't run in parallel, we needed to convert the performance we observed under certain conditions, to the performance that we *would have* observed, had we run the system under the conditions that NAOS was characterized under. The same conversion is needed when we finally predict the performance of an alleged PWFS on an ELT.

In order to extrapolate our measurements to such arbitrary conditions, we need to perform three steps,

1. Characterize PYRAMIR in the laboratory and compare the results regarding the measurement error to theory

2. Build a model on the laboratory measurements to predict the on-sky performance

3. Show that the model reproduces the on-sky performance of PYRAMIR

If the tests implied in steps one and three are positive, we can use the model to also predict PYRAMIR's performance under new circumstances, i.e. different atmospheric conditions and even telescopes.

5.1 The Measurement Error: Comparison of PYRAMIR to Theory

As described above, we will first compare our laboratory measurements to the theoretical predictions of the measurement error by Ragazzoni & Farinato (1999). They showed that when a wavefront is expanded into a set of basis modes, the measurement error of the PWFS for each mode is related to the *radial order* of the mode, i.e. to the number of nodes in the radial direction, and the S/N in each subaperture of the sensor as Eq. 2.17

Fig. 5.1 shows the predicted total measurement error for corrections up to radial order q with a maximum radial order Q of 7 (dashed line) compared to our measurements (asterisks). The measurements were taken simply by calibrating the system with the pupil sampling binned

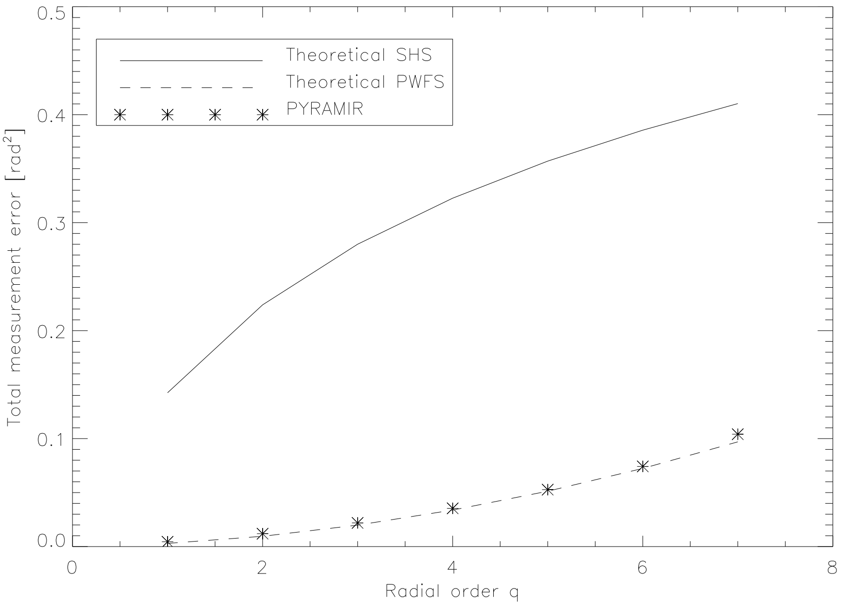

Figure 5.1: *Measurement error coefficient for a correction of radial order r with maximum radial order Q=7. The dashed line denotes the predictions by Raggazzoni & Farinato (1999). The asterisks show our measurements. The solid line marks the theoretical error of a SHS under the same conditions.*

to 7×7 subapertures using the DM's eigen modes with a maximum radial order of 7. Then the measurement error was computed as apertures

$$\sigma^2_{meas} = Tr(RR^T)(S/N)^{-2} \tag{5.1}$$

where σ^2_{meas} is the measurement error, R is the reconstruction matrix derived from the calibration procedure, and S/N is the signal to noise in each subaperture. Note, however, that since we used the DM's eigen modes as basis, and these do not have a clear radial order still the maximum radial order is increasing with increasing mode number. Additionally the behavior of the reconstructor with rising mode number does not differ from that constructed from KL functions. Furthermore the dependence on the number of calibrated modes is perfectly linear (see Peter et al. 2008). Therefore, we combined the modes between mode number n(n+1)/2 and mode number (n+1)(n+2)/2-1 to 'radial' order n.

Over plotted is the measurement error of the SHS (solid line) calculated following Rigaut & Gendron (1992), i.e. Eq. 2.11. The agreement between measurement and theory is excellent.

5.2 Description of the Model

From the laboratory measurements presented in Peter et al. (2008) we have built a model in order to predict the on-sky performance of PYRAMIR. Here we shortly describe its properties: the input parameters of the model are: the detector RON, the wind speed at ground level v_{wind}, the sampling frequency of the loop f_{loop}, the telescope diameter D, the number of subapertures N_{sub}, and the static aberrations and seeing conditions i.e. the Fried-parameter r_0. Actual laboratory measurements - i.e. calibrations - were performed using various binnings of subapertures, calibration amplitudes between +2 and -2 rad and deliberately introduced static aberrations between 0 and +2 rad.

The model calculates measurement, cross talk, aliasing, temporal and fitting errors. The temporal error and fitting error are given in Eq. 2.28 and Eq. 2.27 respectively. We used the atmospheric model from the paper of Greenwood (1977) that implies that the Greenwood frequency is approximately $1.22 v_{wind}/r_0$.
For the second part is the temporal error ,i.e. the one due to the finite bandwidth, we assumed a bandwidth of 7% of the loop speed.
The fitting error under the correction of N modes (Eq. 2.27) will also be used to weight the modes from the sky. This fitting error gives the mean square of the residual wavefront after the correction of N modes. Thus, to the contribution of mode N to the error is given by,

$$w_N = \sigma^2_{f-(N-1)} - \sigma^2_{f-N}. \tag{5.2}$$

The crosstalk and aliasing errors were measured by applying single modes with an amplitude of $1\,rad^2$ mean square and analyzing the response of the system. Their weight in open loop is then given by equation 5.2.

Under CL conditions the weight of the cross talk has to be changed because the modes that cause the cross talk are reduced in their amplitudes with respect to the open loop case. Their weight is changed to the residual p,

$$p = (\sigma^2_{meas} + \sigma^2_{temp} + \sigma^2_{alias}) \tag{5.3}$$

The cross talk should also be included on the right hand side of Eq. 5.3. However, compared to the to other errors it is small. Therefore we neglect it.
The cross talk σ^2_{cross}, aliasing σ^2_{alias} and measurement errors σ^2_{meas} in CL operation can then be expressed by the following formulas,

$$\sigma^2_{cross} = p \sum_{i=1}^{N} \sum_{j=1}^{N} (RI_{\parallel})^2_{ij} \tag{5.4}$$

$$\sigma^2_{alias} = \sum_{i=N+1}^{\infty} \sum_{j=1}^{N} w_i (RI_{\perp})^2_{ij} \tag{5.5}$$

$$\sigma^2_{meas} = tr(RR^T)(S/N)^{-2}_{subap} \tag{5.6}$$

where R is the reconstruction matrix of the system, $I_{\parallel}$ is the interaction matrix of the system and $I_{\perp}$ is the orthogonal to the interaction matrix. The SR is then derived from the total error

$$SR = exp\left[-(\sigma^2_{temp} + \sigma^2_{cross} + \sigma^2_{alias} + \sigma^2_{meas} + \sigma^2_{f-N})\right]. \tag{5.7}$$

Eq. 5.7 now contains the full model and allows to predict the final performance of PYRAMIR from a set of input parameters given at the top this section. The next step is a verification of this model using actual on-sky measurements, before we apply it to compare PYRAMIR to other systems and predict the performance of a pyramid system at other sites.

Chapter 6

On-sky Performance

To verify the model introduced in the previous section, we first introduce the following terminology:
SR and seeing are measured in K band unless stated otherwise. The SR is measured on the science camera and is computationally corrected for static aberrations in the science path. The wind speed is measured at ground level. The term "limiting magnitude" is applied to the faintest magnitude for that the loop could be closed.
For the on-sky measurement this quantity was deduced for the correction of 12 modes at a loop speed of 100 Hz.

The data presented here was taken during two runs of PYRAMIR in February/March 2007 and September 2007.

During the run in February/March the seeing was variable ranging from 0.6–2″. The wind speed varied between 4 ms^{-1} and 10 ms^{-1}. Parts of the measurements were performed through a thin layer of clouds. Under bad seeing conditions we experienced the benefit of the facts that the pupil in the sensor does not move and we use the full telescope aperture: in the past there have been doubts if one can bootstrap the sensor under extremely bad seeing conditions (see Ragazzoni & Farinato (1999) for example). Here we were able to check if this is really a limitation: we closed the loop on PYRAMIR even under a seeing of 2″in K band, a wind speed of 10 ms^{-1} and through a layer of clouds!
The seeing and weather conditions during the September 2007 run were excellent that means a seeing of 0.5-0.″6 and a wind speed of 3-4ms^{-1}. The results of the two runs are presented in the following sections.

6.1 Different Tip-Tilt Correction Methods

For TT correction we can choose between two different methods. The first method is to measure the gradients in every subaperture and build the corresponding reconstruction matrix. In this way (TT-N), the tip and tilt modes are sensed and computed just like any other mode in the basis set. For the other method (TT-QC), the intensity is averaged over each pupil and the system is run like a quad cell. At first sight these two might seem to yield the same results: the total error on the WFS σ_{wf}^2 due to photon and detector noise per subaperture σ_{sub}^2 with N_{ph-sub} photons per subaperture is

$$\sigma_{wf}^2 = tr(RR^T)\sigma_{sub}^2/N_{ph-sub}^2 \qquad (6.1)$$

under the assumption of independent gradients and modes. In the case of TT-QC the total error is given by,

$$\sigma^2_{qc} = \left[N^2_{ph-qc}/(N_{sub}N^2_{ph-sub})\right]\sigma^2_{sub} \tag{6.2}$$

where the subscript 'qc' denotes the values belonging to the QC-method. The values of the reconstruction matrix scale approximately inverse proportionally to the number of subapertures N_{sub}. Therefore, analytically

$$\frac{\sigma^2_{wf}}{\sigma^2_{qc}} = \frac{N_{sub}tr(RR^T)}{tr(R_{qc}R^T_{qc})} \tag{6.3}$$

Measurements show that the factor of proportionality is less than 1. Its magnitude is depending on the calibration amplitude and ranges between 0.45 and 0.59. This implies that the 'normal' TT-N calibration should yield better results.

On the other hand, for the TT-calibration not the entire pupil was illuminated due to peculiarities of our system. In the case of the TT-QC the nonilluminated pixels can be masked out resulting in a smaller average error on the gradients. Measurements will show how these two effects compare.

6.2 Tip-Tilt Stability and Residual Jitter

The stability of the TT signal is important for several reasons. One reason is obviously the quality of the science image with respect to the TT movement and resulting SR. The other is the amount of useful signal for the high order correction. If the TT variation is strong ($\geq 0''.12$), then of course at least one of the pupils has little signal left. This means for the high order correction only the S/N of the order of the residual illumination in the darkest pupil is left. Consequently, a bad TT correction entails a reduced high order performance. The same is actually true vice versa: with decreasing HO correction quality, the FWHM of the stellar image increases, thus, making it more difficult to determine the center position. The (residual) image jitter was measured under open-loop conditions, TT-N correction only, TT-QC correction only, and in HO closed-loop (CL). The TT-jitter was determined by measuring the movement of the guide star's centroid on the science camera on series of 1000 images of typically 0.1 s integration time.

The sky conditions were usually poor: seeing of $0''.8$ or worse and a wind speed of about $8ms^{-1}$. Fig. 6.1 shows the corrected TT-movement versus the seeing. Note that not every measurement series was performed for each of the 4 set-ups.

The TT-jitter is reduced by a factor of about 2 by TT-correction only. The two TT-correction methods seem to perform equally well. As expected, the correction improves further in CL.

The mean residual jitter for TT-only is about 50 mas, for CL it is about 30 mas: less than one pixel and about $1/4$ of the resolution of the telescope. This performance seems to be very stable over the entire range of seeing conditions.

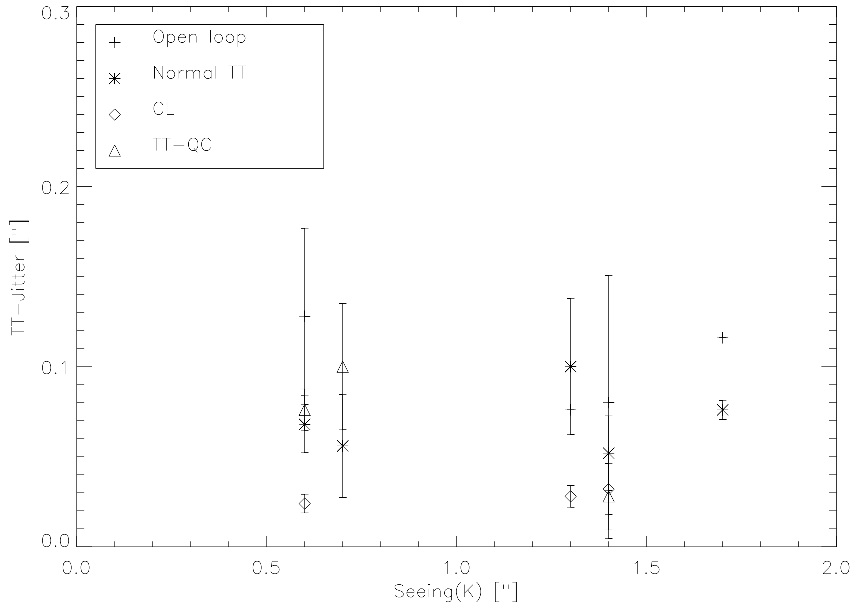

Figure 6.1: *TT-Jitter versus seeing conditions: the points show the median TT-movement versus seeing conditions in open loop, TT-N closed, TT-QC closed, and HO closed. The crosses mark open loop, the asterisks TT-N closed, the triangles TT-QC, and the diamonds CL measurements. Note the small changes in the amplitude of the jitter under CL operation over the range of the seeing.*

6.3 High Order Correction

During several nights we tested the quality of correction for guide stars of different brightness. There are of course many parameters one can examine to optimize the performance of an AO system. For the SR versus brightness curve we tried to optimize them on the fly in order to get the best possible SR on the science image. What was changed was the loop speed and the number of modes used for the measurement. As mentioned above we were able to close the loop even under rather bad (i.e., seeing $\geq 1\farcs3$) conditions. This however yielded SRs below 1% that are not shown here.

In order to serve our ultimate purpose of comparing the performance to Shack-Hartmann-type systems on other telescopes, we will use the signal-to-noise ratio per subaperture per loop cycle (SNAC) on the wavefront sensor detector rather than the guide star magnitude as the independent quantity. This choice makes the results independent from the details of the precedent system (telescope, WFS type, etc.). The signal and noise are both measured directly on the PYRAMIR detector. The noise is taken from a sky image plus additional (theoretical) photon noise of the target. Fig. 6.2 and 6.3 show the correction quality versus the SNAC from the two different runs. Here, we over plotted the predictions derived from the model described in Sec. 5.2. The parameters in use are denoted on top of the image.

Fig. 6.2 shows the measurement under excellent conditions. The seeing was about $0\farcs6$ and the wind speed 3–4 ms^{-1}. We sent 20% of the incoming light to the sensor. We see that we can achieve a maximum SR of 63% in K band. This stays up to a SNAC of about 3.5 (corresponding

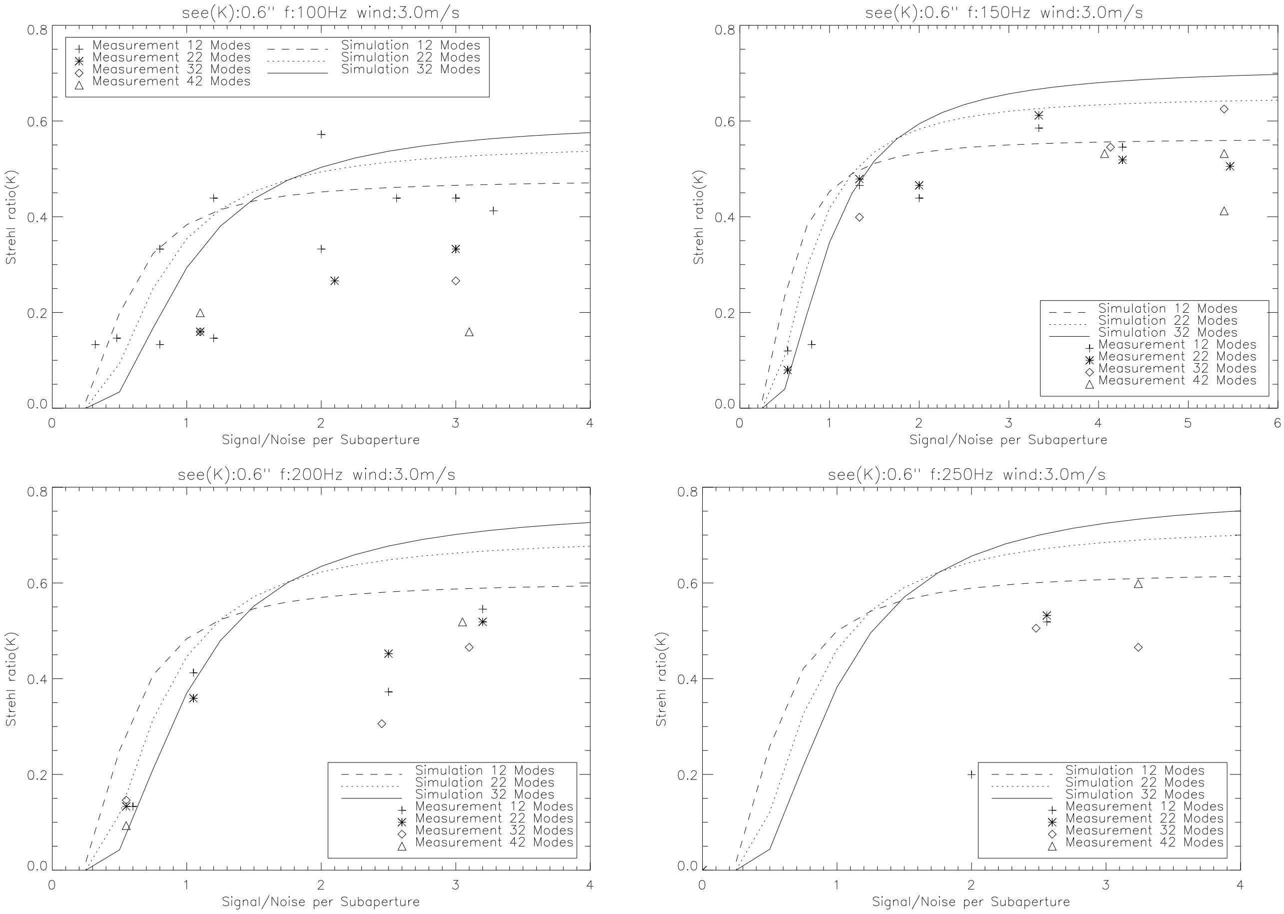

Figure 6.2: *Dependence of the closed-loop performance on the SNAC obtained during our observations in September 2007. The different symbols denote: cross: 12 modes, asterisk: 22 modes, diamond: 32 modes and triangle: 42 modes closed. The four panels show different loop frequencies. We over plotted calculated curves from our model for seeing of 0.″6 and wind speed of 3ms^{-1}. The solid curve denotes 12 modes closed, the dotted 22 and the dashed 32.*

to 4.3 mag), then it drops continuously until a limiting SNAC of 0.4 (6.7 mag) in K band. The model compares well to our measurements for the lower loop speeds. Note that for the loop speed of 100 Hz the correction with a low number of modes performs better than the correction with a higher number of modes. The reason is that the higher order modes are also 'faster' and cannot be corrected at a loop speed of 100 Hz. On the other hand the measurement error increases with the number of modes we want to correct. Thus, the total error is larger if we try to correct a high number of modes than if we correct a low number of modes only at this speed. This effect is however not included in the model.

For the higher speeds the model slightly overestimating the SR, but it still matches the drop toward the limiting SNAC well. The overestimation of the SR for high speeds probably results from an overestimation of the band width of the correction loop.

Fig. 6.3 displays the closed-loop performance under bad sky conditions. The seeing was about 1.″1, the wind speed was about 7ms^{-1}. The beam splitter sent 90% of the light to the

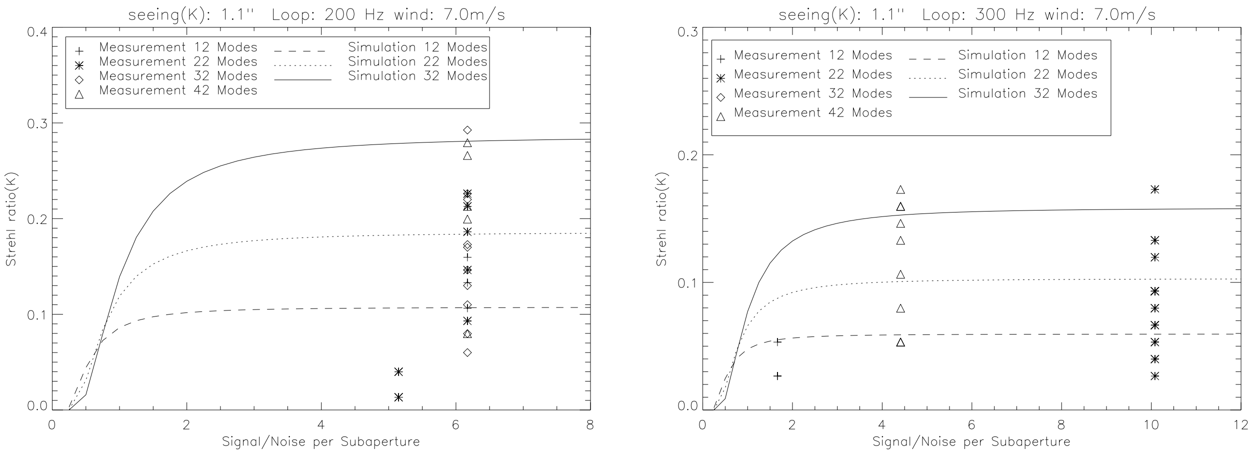

Figure 6.3: *Dependence of the closed-loop performance on the SNAC obtained during our observations in March 2007. Note that the observations in March 2007 used a different beam splitter than those in September 2007. The symbols are as in Fig. 6.2. The measurements were performed with 200 Hz (left) and 300 Hz (right). Symbols and line styles are as in Fig. 6.2*

WFS. The limiting magnitude in this case was again 6.7 mag. The variations in the SR are large probably due to fast changing sky conditions. Due to this variation it is difficult to estimate how well our model matches the result. However, we can state that the model is conform with the range of SR and not overestimating it. For median conditions (seeing 0″.8 and wind speed of 4 ms^{-1} – results not shown here) the SR reached up to 50%.

Regarding the fact that the reconstructor fits quite well to theory (see section 5.1) the performance of the system is excellent. Note that the bright limiting magnitudes result from the fact that we highly oversample the pupil and have a large RON. However, we emphasize again that for a test of the pyramid principle the SNAC on the detector is the quantity of interest rather than the absolute flux from the target star.

Chapter 7

Implications

The measurements done were performed with one special infra red PWFS. The question we want to address here is: is there really an improvement between SHS and PWFS. Now that we know that our laboratory measurements fit the on-sky performance well enough that we can use them to tackle this problem.

7.1 Comparison with NACO

In order to be able to compare PYRAMIR with NACO (Brandner et al. 2002) we have to know the number of photons on NAOS (the AO system of NACO) for a specific guide star magnitude and also the noise on the detector. The first can be calculated by the NACO exposure time calculator under the assumption that the NAOS and CONICA (the near-infrared instrument of NACO) fluxes for a 50/50 beam splitter are identical. The second can be found in the paper by Rousset et al. (2003). We adapt a value of 10 e^- rms for the 7x7 lenslet array and 19e^- rms for the 14x14 lenslet array. Also we find the number of subapertures in the same reference. We then use the values given on top of the figures as input parameters. Unfortunately, the beam splitter in use is not presented in any reference. However, calculations imply that the beam splitter sent 90% of the flux to NAOS and 10% of the flux to CONICA. Also the wind and loop speed were not presented explicitly. Possible loop speeds are given in Gendron et al. (2003). In order to make a reasonable comparison, we adapted the wind speed such that the maximum SR is similar. A comparison between PYRAMIR and laboratory measurements with NACO (see Rousset et al. 2003) where the wind speed is given explicitly supports this approach.

The NACO measurements were also taken from the reference above and magnitudes were converted to S/N. As can be seen, for the low-order case (Fig. 7.1, left) both sensors perform quite similar with a superiority of the pyramid in the regime between limiting magnitude and saturated SR (marked by the vertical lines). The fact that one of the two points belongs to seeing conditions better than assumed for the model confirms this fact. Note also that we assumed a large wind speed.

For the high order case (Fig. 7.1, right) both curves match quite well for the limiting magnitude and in the bright star regime. But in between the pyramid is performing slightly better.

Note that some of the points where the pyramid seems superior belongs to a seeing of $0\farcs5$ or better. Therefore, it is very likely that this superiority is real. This is confirmed by the fact that this regime also exists in the comparison with the laboratory measurements and with the low order sensor.

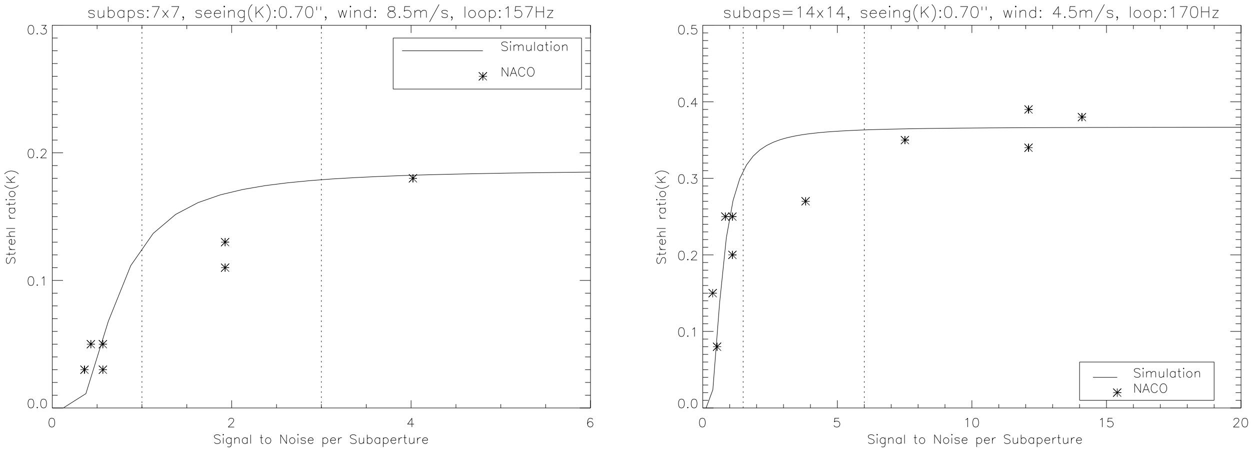

Figure 7.1: *Left: comparison of the model constructed from PYRAMIR measurements with the NACO-IR-sensor using a 7x7 lenslet mask). The asterisks are NACO measurements from Rousset et al. (2003), the solid curve is calculated from our model of the pyramid sensor. The performance is very similar.In the intermediate range between limiting magnitude and maximum SR the pyramid performs better. Right: comparison of the model constructed from PYRAMIR measurements with the NACO IR sensor (14x14 array). The performance is again similar. In the region between limiting magnitude and saturation the pyramid again performs better.*

7.2 Auxiliary Wavefront Correction for a Laser Guide Star System at an ELT

Another possible application for a PWFS is as auxiliary WFS for a Laser Guide Star (LGS) AO system. For an 8m class telescope the auxiliary correction can be kept to very low order modes: TT and maybe focus. For a pure TT sensor the use of a SHS might be preferred because the size of the subapertures is the same as for a PWFS and there is no light 'lost' on any pyramid edges. In the case of an ELT things look different. Under the assumption (se e.g. Dierickx 2001) that the highest radial order to be corrected by the auxiliary WFS scales with the telescope diameter, for a 42m telescope 6 or more radial orders have to be corrected with an auxiliary WFS. The reason is that the cone-effect increases with the size of the telescope. The question is: what sensor should be used ? Again, we will try to extrapolate from our measurements. We assume that the laser system perfectly corrects the wavefront up to radial mode order 41. The corresponding aliasing on the auxiliary sensor must then be treated like cross talk, i.e., with reduced strength due to the correction by the laser system.
Fig. 7.2 shows the behavior under typical sky conditions for a 42m telescope with the first 7 radial orders corrected by the auxiliary sensor. Over plotted is the same for a (theoretical) SHS. To model the SHS we exchanged the measurement errors of the two sensors and assumed the aliasing and cross talk to be of the same order. These two errors are small anyway compared to the measurement error especially in the case of the limiting magnitude. Once again there is a large regime where the PWFS's performance is superior. At 20% SR the gain in magnitude is about 0.7 for a detector with 10 e^- rms noise. Or the other way around: At a S/N of 2 the

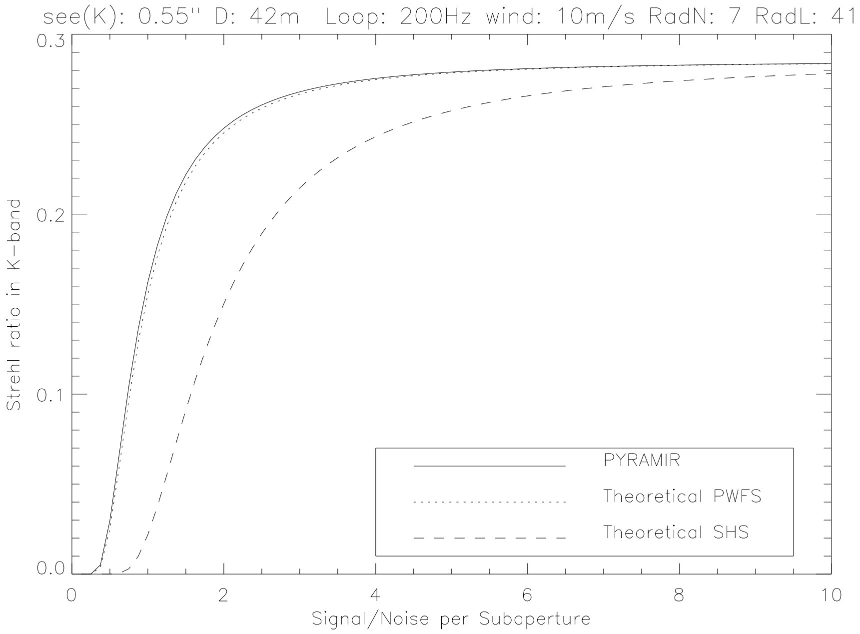

Figure 7.2: *Performance of a 42m telescope with laser guide star. The auxiliary WFS corrects 7 radial orders the laser up to radial order 41. The solid curve shows the extrapolation from PYRAMIR, the dotted curve the theoretical pyramid sensor and the dashed curve the SHS.*

SR is 0.26 in stead of 0.15 . We did not include effects of wavefront degradation toward the limiting magnitude in our model. This degradation will have the effect to equalize the limiting magnitude for both systems. Still from Fig. 7.2 it is clear that there will be a regime of superiority of the PWFS over the SHS.

Chapter 8

Conclusions

In this part of the thesis we presented laboratory measurements performed with the pyramid infrared wavefront sensor (PWFS) PYRAMIR. After a short introduction into the history of PWFS and their working principles, we presented the PYRAMIR system and explained the details of the system especially the possible read out modes of the detector. The system can reach a speed of about 300 Hz with a read out noise (RON) of 20 e^- rms. The calibration procedure of the system was described in detail. The pitfalls of Tip-Tilt (TT)calibration were discussed leading to the conclusion that a static part in TT will reduce the limiting magnitude and enhance TT-jitter. Tis effect, however, is small. Still, we included a static TT-part in the bias pattern of the deformable mirror (dmBias) to perfectly center the beam. Also it has to be guaranteed that the amplitudes of calibration are the same in both axis in order to gain similar performance in both directions.
Some of the fundamental sources of reduced performance were examined. We found that the amount of light diffracted out of the pupil images is 50% for a flat wavefront decreasing non-linearly up to 2 rad wavefront error where it becomes almost stable at 20%. A comparison with simulations shows that in our case this loss results from diffraction at the pyramid edges and imperfections in the optics. The latter outweighing for aberrations stronger than about 1.5 rad. The effects of a Gaussian illumination of the pupils, as well as the effect of an extended calibration light source were investigated. Both have strong influence on the sensitivity of the system and should be avoided. On the other hand an extended target during the measurement does only slightly affect the performance. Thus, the calibration light source should be as point like as possible for all applications.
The effect of RON on the limiting magnitude of the guide star has been widely discussed. In the case of infrared detectors this noise is quite high. In our case 20 e^- rms. This reduces the limiting magnitude by 5 mag. We investigated into the best possible mode set between the eigen modes of PYRAMIR, the eigen modes of the deformable mirror (DM), and the Karhunen-Loève (KL-)modes. The last two mode sets seem promising for the use on-sky. The latter has a larger linear regime than the eigen modes of the DM. The difference is small and, therefore, the correction error will not vary by much. Still the larger linear regime might help to close the loop under bad seeing conditions.
We tested the best treatment of noncommon-path aberrations by applying artificial modes to the DM. The best treatment turned out to direct these aberrations completely into the path of the sensor. A possible better way using two calibrations one for modes with positive amplitude one for those with negative amplitude was proposed to reduce the error of the mode with static aberrations but put aside due to the fact that it was not running stably during the testing on-sky.

The importance of a small calibration amplitude to minimize the resulting reconstruction error was shown.

After the measurement of these fundamental properties the subject of the best number of modes to calibrate was addressed. To solve this we investigated into the behavior of modal cross talk, aliasing, and measurement error in dependence of the number of modes calibrated. We found that the averaged aliasing coefficient varies only slightly with the number of modes whereas the average modal cross talk coefficient decreases inversely linear with this number and the measurement error rises linearly with this number. Including the (theoretical) contribution of the KL modes in the wavefront error on sky we could show that the contribution of aliasing rises like $N^{\frac{(2-\sqrt{3})}{2}}$, the contribution of cross talk becomes constant for larger N and the measurement error rises linearly with N. In closed loop only the error due to modal cross talk changes with respect to the open loop measurement. It will decrease because the modes that are corrected will contribute less to the modal cross talk than in open loop. The error of the residual wavefront decreases like $N^{-\frac{\sqrt{3}}{2}}$. Altogether we could show that at the border of the limiting magnitude the fitting error surpasses all other errors for a low number of corrected modes but will be overpowered by the measurement error at about the place of the optimum number of modes to be corrected. For the PYRAMIR system this is 5 modes for a S/N of 1. The other errors will become important for brighter stars. Here cross talk and aliasing error are almost identical in strength. In the case of noncommon-path aberrations in the system the modal cross talk and aliasing errors will rise. Modal cross talk linearly, aliasing error stays constant until the static aberration reaches the border of the linear regime of the sensor. Then it increases nonlinearly.

From the entire error budged we could build a model to predict the performance on-sky for various seeing conditions. For a seeing of 1″in K band and a wind speed of $5ms^{-1}$ we can achieve 38% Strehl ratio (SR) in K band but we have to run at about maximum frame rate (300 Hz). The limiting signal to noise ratio per subaperture on the detector is about 0.25 or 6.0 mag in K. For good seeing conditions (0.″6 in K band, wind speed 4 ms^{-1}) and a moderate loop band width the predicted SR will be about 60% for bright stars. Again the limiting signal to noise ratio per subaperture on the detector is about 0.25 that corresponds in this case to 7.2 mag in K.

We further presented a comparison between the measurement error of PYRAMIR and theoretical predictions, and found a remarkable agreement. We presented on-sky measurements of the pyramid infrared wavefront sensor PYRAMIR mounted at the 3.5m telescope on Calar Alto. The system works even under 2″seeing in K band. Under a seeing of 0.″8 in K band we measured a residual Tip-Tilt jitter of < 30 mas rms and a Strehl ratio in K band up to $\approx$ 50%. Under fair conditions the Strehl ratio in K band reaches up to $\geq$ 60% on bright stars. The limiting magnitude under these conditions was about 6.7 mag in K with 20% light on PYRAMIR. Under bad sky conditions we still reach about 30% SR in K band with a loop speed of 300 Hz. We found our model constructed from laboratory measurements fitting the real performance very well. A comparison of the model predictions for the VLT showed high evidence for a superiority of the pyramid over NACO in the regime between limiting magnitude and saturation in the Strehl ratio. For an ELT operated with a laser guide star system the benefit of a PWFS is much larger: At a Strehl ratio of 0.2 the gain in magnitude is about 0.7 mag and, at a Signal to noise per subaperture of 2, the Strehl ratio is 0.26 in stead of 0.15.

Chapter 9

Binarity in (High Mass) Star Formation

As already described in the introduction the formation mechanism of massive stars is still highly debated. The reason why this fundamental astronomical problem is still undecided is, from theory side, the high photon flux of the stars that can in principle stop accretion and set an upper mass border around 10 $M_\odot$. From the observers side the difficulties lie in the large average distance to these objects, the fact that they are deeply embedded during formation, and their low number density.

Two main lines of theory have been developed to overcome the termination of accretion: 1. A modified accretion theory (see for example Yorke 2002) using nonspherical accretion to concentrate the photon flux toward the poles of the star and high pressure and turbulence in the ambient medium to allow for high accretion rates. 2. The so called 'coalescence scenario' where the stars compete for the matter from an entire cluster and the massive stars are formed by mergers of intermediate mass stars (see for example Bonnell 2008).

The stellar populations that result from these different scenarios differ in the way how binaries or multiple systems are formed. For the accretion scenario, especially in regions where the stellar density is low, fragmentation of the pre-stellar core is much more likely the origin of multiplicity and close companions than the capture of a companion. On the other hand in the coalescence scenario close binaries will be often formed by failed mergers i.e. by a capture scenario. This difference can in principle be used to distinguish between the two formation mechanisms.

However due to the fact that the stars involved in this process are young and probably still accreting the stellar systems will undergo some evolution. The two different mechanisms of multiple systems and the way they evolve will be discussed in the following. For a more detailed and complete review of high mass star formation we refer to Zinnecker & Yorke (2007).

Before we start we have to define some important concepts and terms. The term *binary* and related expressions always refers to stars with one companion only whereas the term *multiple* includes one or more companions. In papers on the subject of binary and/or multiple systems there are different measures to describe the property of multiplicity. Some treat multiple systems with more than one companion as a number of binaries (for example Brandner et al. 1996, 1998). A triple system for example is treated as two binaries. The term used within this approach is the *binary frequency* i.e. the number of binaries over the total number of primary stars. Leinert et al. (1993) use the term *multiplicity fraction* that counts the number of systems with at least one companion over the number of total systems.

We will not follow these approaches but rather use the *companion star fraction* (CSF) as a measure of multiplicity (like in Zinnecker & Yorke 2007). This CSF is the ratio between the number of companions and the number of primaries i.e. the average number of companions per primary. If we for example have a single star, a binary and a triple system the CSF numbers ((0)+1+2)/3=1. The binary frequency in this case would have been 3/4, the degree of multiplicity 2/3. To stay coherent we will also convert the binary frequency and multiplicity fraction from the literature to CSF.

9.1 Observations

In contradiction to the long time favored star formation scenario via a monolithic collapse of a pre-stellar core (Shu et al. 1987), observations within the last two decades strongly hint toward a multiple star formation scenario at least of equal importance. Multiplicity seems to be present already in the early phases of star formation. Launhardt (2004) for example found, due to advances in submm interferometry, pre-stellar binary cores with sub-arcsec separations. The sample under investigation was small, however he detected binary cores with separations down to the detection limit. Further studies are necessary to strongly enlarge the sample and confirm these findings.

In the regime of young low-mass i.e. TTauri stars a large range of studies has been performed. Especially the regions of Taurus Auriga (Leinert et al. (1993), Köhler & Leinert 1998), Scorpius (Brandner & Köhler (1998), Kouwenhoven et al. 2007), Lupus (Brandner et al. 1996), and ρ Ophiuchus (Ratzka et al. 2005) have been places of repeated investigations. The CSF in all regions except Taurus Auriga and Orion is comparable to that of low-mass main sequence stars of $\approx 60\%$ as found by Duquennoy & Mayor (1991).

In the Taurus Auriga region Leinert et al. (1993) and Köhler & Leinert (1998) find a CSF of about 100% for TTauri stars. They also report a tendency for close binaries to be equally bright whereas wide companions have smaller brightness ratios. In Orion Köhler et al.(2006) detect a low CSF for low-mass stars (≈ 0.2). This CSF is obviously much lower than for field stars of 60%.

This findings are somewhat contrary to those found in ρ Ophiuchus. Ratzka et al. (2005) find close binaries with small flux ratios to be largely overabundant with respect to Taurus Auriga. This compares again well with the findings of Duquennoy & Mayor (1991) for field stars. They also find an increase in the number of systems toward low mass ratios. A difference in the distributions of separations can be found for the Scorpius region. Brandner et al. (1998) compare the binary separations of TTauri stars in upper Scorpius-A and -B. The difference between these regions is that in Upper Scorpius-B contains almost no massive stars whereas Upper-Scorpius-A contains a significant number of B-type stars. This presence of massive stars seems to affect the binary separation of the TTauri stars: in Upper Scorpius-A the separation is about 90AU whereas in Upper-Scorpius-B the separation distribution peaks at 215AU.

For massive stars themselves Apai et al. (2007) use a radial velocity method to detect very young massive binaries in UCHIIs. They find that $\geq 20\%$ of their targets are in close multiple systems and conclude that after a completion of the sample this finding is consistent with a CSF of 1. The presence of very young massive binaries is confirmed by Comeron et al. (2006). Their observation of G76.188+0.098 also reveals a binary star in the center of an UCHII.

For more evolved stars studies by Kouwenhoven et al. (2007) indicate that the overall CSF between B and A stars in the Scorpius OB2 association numbers 100%. This compares well to the finding in other massive star forming regions. Mason et al. 1998 performed a Speckle survey on O-type stars sensitive to separations $\geq$ 30 mas and brightness differences $\leq$ 3 mag. They found a CSF of $\geq$ 59%. The observations of Outmaijer et al. (2006) increase this number to 81%. In the Orion Trapezium cluster the CSF of the high mass stars is $\geq$ 100% (Preibisch et al. 1999, Schertl et al. 2003, Kraus et al. 2007) arising from mostly hierarchical multiple systems. Preibisch et al. also find a change in the CSF between stars earlier than spectral type B2 and later than B2. In NGC6611 Duchene et al. (2001) find for the 60 high mass stars observed with adaptive optics a CSF of 18 ± 6% in the range of 200-3000AU. They argue that the overall CSF is at least 45% but very likely as high as 100%. Their findings also compare well with other high mass binary surveys when comparing the overlapping separation and brightness regimes. Regarding the distribution of separations however they find a high rate of wide binaries compared to other massive star forming regions.

Altogether we can state that the CSF of massive stars seems to be higher by a factor of $\geq$ 1.5 than that for low-mass stars maybe with exception of the Taurus Auriga region. The fraction of spectroscopic binaries is about 30% for high-mass stars. This compares well to the finding that the median binary separation is smaller in high mass star forming regions (maybe with exception of NGC6611) than in regions of pure low-mass star formation. Any theory explaining star formation has to reproduce these findings.

9.2 Theory of Binary Formation

In the last section we discussed the various observational findings of the results of binary star formation. These results seem to depend on the mass of the primary star, as well as on the initial conditions of the cloud. The evidence of the first is given by the increase of the CSF toward stars with earlier spectral type the second from the comparison of the binary separations between Upper Scorpius A and Upper Scorpius B.

Theoretical models for the formation of close binary stars can be split into two steps: First the original formation of the binary i.e. capture processes or fragmentation of the pre-stellar core and then secondly a possible further evolution of the binary due to interactions and/or accretion processes.

In the following the most important channels of binary formation are presented.

9.2.1 Disc Assisted Capture

The formation of a binary system by capture in most cases forms a wide binary. This mechanism is very unlikely to work for stellar densities as observed in star forming regions due to the small cross section of the stars. However if the stars harbor an accretion discs these discs will strongly enhance the cross sections and make captures much more likely.

Moeckle & Bally (2007) performed a SPH simulation of star-disc encounters. The capture of companions produced a 30% binary frequency at 0.5 Myr for Orion like parameters. Still the frequency is much below the observed one for massive stars.

9.2.2 Fragmentation of the Pre-stellar Core

A possibility to form one or more rather close companions in-situ is by a fragmentation of the pre-stellar core. (For an overview see for example Bodenheimer & Burkert (2001) or Clarke 2001). The binary parameters of the outcome vary widely. However there are agreements but also clear differences between the formation of pure binary stars and that of small stellar clusters.

In both cases a high fraction of binaries is generated. However in the second case the CSF increases with primary mass that is not true in the first case i.e. the probability of a core to split is independent of its mass in this case. Also in the case of the formation of a small stellar cluster the *form* of the mass function of the companions should be independent of the primary mass whereas in the case of pure binary formation the *mass ratio* distribution is invariant for primaries of different masses.

Simulations of pure fragmentation of a massive cloud core are investigated in Krumholz (2006). In his simulation the core fragments into a few parts that each by itself forms a star or stellar system without further interaction between the different fragments. Companions to massive stars are formed via disc fragmentation (Krumholz 2008). Initially the companions have masses around 1 $M_\odot$ and orbit the primary at separations of $\approx$ 100 AU. Further evolution via accretion and interaction between the two stars then forms close ($<$ 10 AU) massive-massive binaries.

9.2.3 Disc Fragmentation

A related channel to form a wide low-mass companion of a massive star is via fragmentation of the massive disc. Kratter & Matzner (2006) explored this mechanism. They found that massive discs are more subject to fragmentation than thin discs usually found around low-mass stars. The fragmentation process results in a low-mass companion of up to about 10% of the mass of the primary star in a wide orbit. This companion will starve the original accretion process of the massive star and constrain the highest reachable mass to $\approx$ 110 $M_\odot$. This mass limit compares well with the apparent upper mass limit for the initial mass function (IMF) in star forming regions.

9.2.4 Accretion onto Wide Binary

Independent of the original formation mechanism the binary will strongly evolve if the companions of the stellar systems still accrete circumbinary matter.

Bonnell & Bate (2005) and Meader & Behrend (2002) performed simulations of the evolution of a wide binary via accretion. They found that this accretion tends to form close equal mass systems. For very close binaries the masses are even more adjusted by a mass transfer between the companions due to shell expansion of the protostars (Krumholz & Thompson 2007). Bonnell & Bate (2005) argue that for the formation from a turbulent medium a relation between the mass of the system and the separation like $M_{sys}^{-2} \approx R_{bin}$ is expected. Their simulations seem to confirm this analytically derived relationship.

9.2.5 Dynamical Processes

The outcome of the capture process within a stellar cluster including further evolution through accretion processes has been modeled by Bate et al. (2002). They used a 3D model of gas rich collapsing proto-cluster. The binaries form via 3 body capture followed by an orbital decay. The exchange reactions usually eject the object with the lowest mass. Further interactions then harden the binary. This processes usually result in a close massive binary with a wide low-mass companion. Further interactions then might eject the wide companion resulting in a pure close binary system.

9.3 Detection Methods for Close Companion Stars

There exist several methods to detect companions of a star. The range of spatial resolution and the dynamical range differs strongly between these methods. In the following these methods and their limitations shall be explained shortly.

9.3.1 Eclipsing Binaries

The search for eclipsing binaries makes use of the fact that an eclipse or tidal distortion of the primary star causes variations in the total flux of the object. This method is also used for the detection of planets. Generally it is sensitive to companions of all separations. However the probability to detect wide binaries (i.e. $r \geq 10\sqrt{M_{primary}/M_{\odot}}$ AU) with this method is small due to their long orbital periods. Due to photometric accuracies of more than 1% the radius of the companion can have a radius as small as 0.1 radii of the primary that for a 50 $M_{\odot}$ star means the ability to detect a $1.7 M_{\odot}$ star.
With this method it is also possible to determine the period of the binary and the sum of the stellar radii. However one has to be careful not to mistake intrinsic luminosity variations caused by cooler regions on the surface of the star with a true companion.
Hilditch et al. (2005) for example observed 40 eclipsing binaries in the small Magellanic cloud. With the use of additional spectroscopic data they could derive the masses, radii, and surface gravities of the stars. Also Gies (2003) compiled a list of 107 known eclipsing double lined spectroscopic O-star binaries.

9.3.2 Radial Velocity Measurements

Radial velocity measurements provide information about potential companions by variations of the velocities determined from spectral lines of the star (see Fig. 9.1). To determine the parameters of a companion a long term monitoring program is needed to follow the variations in the central velocity of the spectral lines. Difficulties for this method arise from contamination

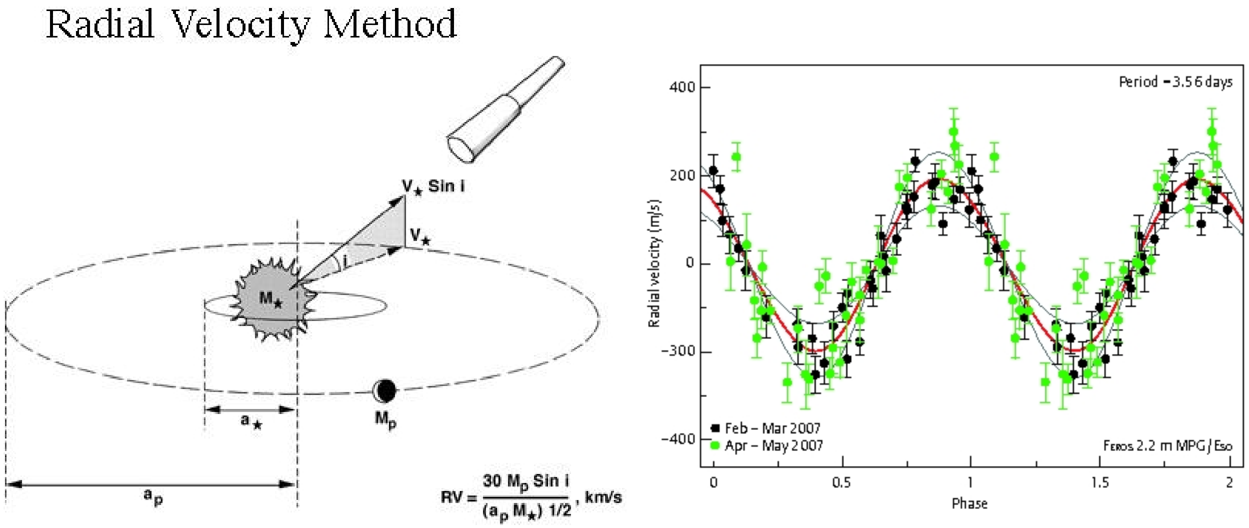

Figure 9.1: *Radial velocity measurement. Left: principle of the method (from http://obswww.unige.ch/ udry/planet/method.html).*
Right: radial velocity measurement of TW Hydrae a young star harboring a planet (Courtesy of J.Setiavan).

by stellar rotations (dark spots mimicking a companion), pulsation, and emission. The method favors close equal mass pairs as can be seen from the following expression for the maximum radial velocity v_{max} of the primary star (Cochren & Hatzes 1996):

$$\Delta v_{max} = 2\sqrt{G}\frac{m}{\sqrt{M a_0}} sin(i) \tag{9.1}$$

where G is the gravitational constant, m is the reduced mass, M is the system mass, a_0 is the semi-major axis, and i is the inclination angle. This velocity must be above the detection limit of the spectrograph. Therefore the detection probability rises toward the maximum of $m = 0.5M$ (i.e. an equal mass binary) and with decreasing separation a_0. Usually the limit of detectable separations is at a few AU. Also an orientation of the orbital plane close to the line of sight is highly favored. Hillwig et al. (2006) for example observed binaries with the radial velocity method in Cas OB6 and found a binary frequency of 50±19%. In NGC 6231 Sana et al. (2007) found a binary frequency of 63 ±20 % with the same method

9.3.3 Spectro-Astrometry

This method uses small variations in spatial profile of spectra to detect sub-psf binaries in the mas regime. It is sensitive only for binaries with differing spectral features. The method is based on the fact that in a binary where both companions have different spectral features i.e. one is a Hα emitter and the other not the spacial position of the centroid of that line is shifted with respect to the continuum. Fig. 9.2 shows a cartoon of the method.

The dynamic range reaches up to 6-7 mag brightness difference (Baines et al. 2006). The detectable separations are of the size of the slid-width. Larger separations result in a reduced signal from the companion reducing the detectability and yielding a too small separation. For

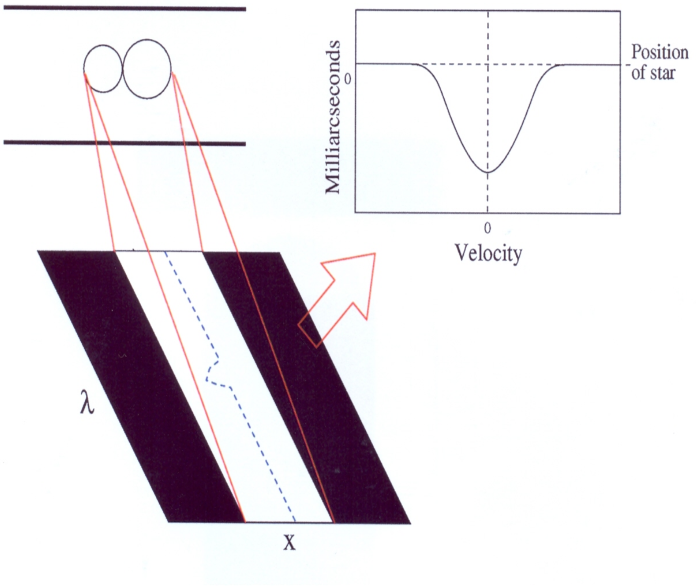

Figure 9.2: *Method of spectro-astrometry (from Oudmaijer et al. 2006)*

a detection the stars also have to have strong lines. Oudmaijer et al. (2006) observed 31 Herbig Ae/Be and detected a 70% binary frequency. This shows how fruitful this method can be.

9.3.4 Long Baseline Interferometry

This method needs at least two telescopes at spatial distance B the so called 'baseline'.

The light of the two telescopes is added interferometrically yielding a pattern of brighter and darker fringes. The signal measured by an interferometer is the so called visibility $V = \frac{I_{max}-I_{min}}{I_{max}+I_{min}}$ where I_{max} and I_{min} are the maximum and minimum intensity of the fringe pattern respectively. The visibility can be expressed from the intrinsic parameters position angle θ, separation ρ, magnitude difference Δm of the binary system, and projected baseline B, position angle on sky of the projected baseline ψ, and wavelength pass-band λ of the telescope as (McAlister 2007),

$$V^2 = (1+\beta)^{-2}\left(\beta^2 V_1^2 + v_2^2 + 2\beta V_1 V_2 \cos\left[\frac{2\pi B}{\lambda}\rho\cos(\theta-\psi)\right]\right) \tag{9.2}$$

where

$$\beta = 10^{0.4\Delta m}, \tag{9.3}$$

and

$$V_{1,2} = 2\frac{J_1(\pi\Theta_{1,2}B/\lambda)}{\pi\Theta_{1,2}B/\lambda} \tag{9.4}$$

J_1 the Bessel function of first order and $\Theta_{1,2}$ the angular diameters of the target stars. The sensitivity of the best interferometers goes down to about 0.2 mas (McAlister 2007). From Equation 9.2 we can see that the visibility depends exponentially on the magnitude difference of the stars. Therefore the system is most sensitive to equal flux pairs. A magnitude difference of 4-5 mag still can be detected at the costs of spatial sensitivity by spatially filtering the interfering

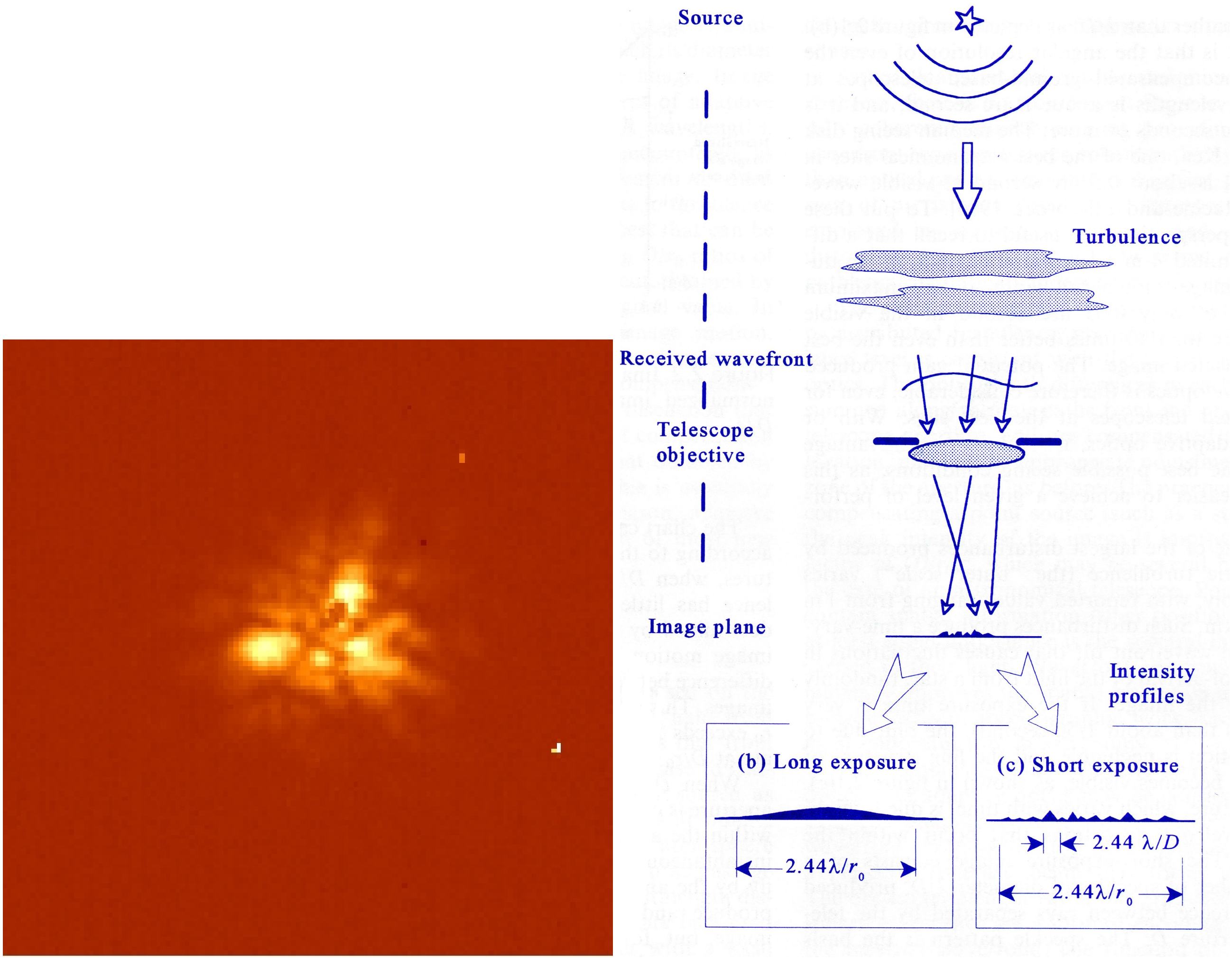

Figure 9.3: *Speckle interferometry. The left panel shows a image with speckles taken in K' band on the Calar Alto 3.5 m telescope.*
The right panel shows the principle outcome of a long and a short exposure. The light from the source is collected by the telescope and yields a Gaussian distribution of width $2.44\lambda/r_0$. On the right side (Hardy 1998) a short exposure image shows speckles of size $2.44\lambda/D$ i.e. with the full resolution of the telescope. From these speckles one can reconstruct the original image unperturbed by the atmosphere.

beams (McAlister 2007). An interferometric technique was used to investigate into the binary frequency of massive stars in the Carina Nebula by Nelan et al. (2004). They used the HST fine guidance sensor. The most prominent object HD93129a an O2f star and one of the most massive stars know up to date has been resolved into a 55 mas binary.

9.3.5 Speckle Interferometry

A related technique named Speckle interferometry has been used for some time to retrieve diffraction limited images from large telescopes. The working principle is presented in Fig. 9.3.

Here many snapshot images are taken that leave the atmosphere basically 'frozen'. The PSF of size $2.44\lambda/r_0$ shows substructures i.e. 'speckles' of size $2.44\lambda/D$. They contain the image with the full resolution of the telescope. With Fourier techniques a full frame real image is retrieved from the speckles. As mentioned above the technique has a resolution of the telescope where it is used. Therefore it is sensitive to separations down to about 30mas at 8m class telescopes. At this separation the method is sensitive to binaries with similar fluxes and for larger separations up to about 3 mag brightness difference. Additionally for the high read out frequency one has to limit the field of view. Mason et al. (1998) performed a search for binaries among O-type stars using Speckle techniques. They found a binary frequency of 23% of visual binaries. Schertl et al. (2003) and Kraus et al. (2007) performed a search for massive binaries in Orion using this technique. They found a high incidence of multiplicity for massive stars with a CSF > 1.5. Preibisch et al. (1999) additionally detected a change in CSF at spectral type B2.

9.3.6 Adaptive Optics

The principle of AO has already been described (see Chapter 1). Therefore we limit the discussion to the sensitivity of the system. For diffraction limited imaging as achieved in the near infra red the resolution is limited to that of the telescope i.e. $0\farcs06$ for an 8m class telescope in K' band. The dynamic range is larger than that for Speckle imaging ranging up to 8 mag or larger because the integration times are potentially long. Note however that this dynamical range close to the target is reduced due to the halo of its PSF.

Due to the benefit of a potentially larger dynamical range, however, one has to be careful about a contamination with background stars. Duchene et al. (2001) performed a binary search on massive stars in NGC6611 they detected $\geq$ 18% binary frequency with more than half low-mass companions (M2/M1$\leq$0.2) Roberts et al. (2007) performed a survey of B-type stars using AO. They detected 23±6 % binary frequency within their detection limits. Turner et al. (2008) observed 116 O stars from the list of Mason (1998) with an AO-system. The dynamic range was extended from the value achieve=d with Speckle techniques of 3 mag to 6 to 9.5 mag. They detected 40 new companions. This highlights the benefit of AO with respect to Speckle interferometry.

9.3.7 Lucky Imaging

Lucky imaging is also a method using short exposure images. In contrast to Speckle interferometry this method, however, produces direct images. The method makes use of the fact that there exists a finite probability P to get a perfect image without atmospheric distortions. This probability is given by (Fried 1978)

$$P \approx 5.6 \exp[-0.1557(D/r_0)^2] \tag{9.5}$$

where D is the telescope diameter and r_0 is the (wavelength dependent) atmospheric coherence length Therefore the method is strongly limited to longer wavelength and smaller telescopes. The final image is then produced by adding the best short exposure images where the definition of 'best' depends on the science case i.e. that resolution etc. is needed. Usually the method is

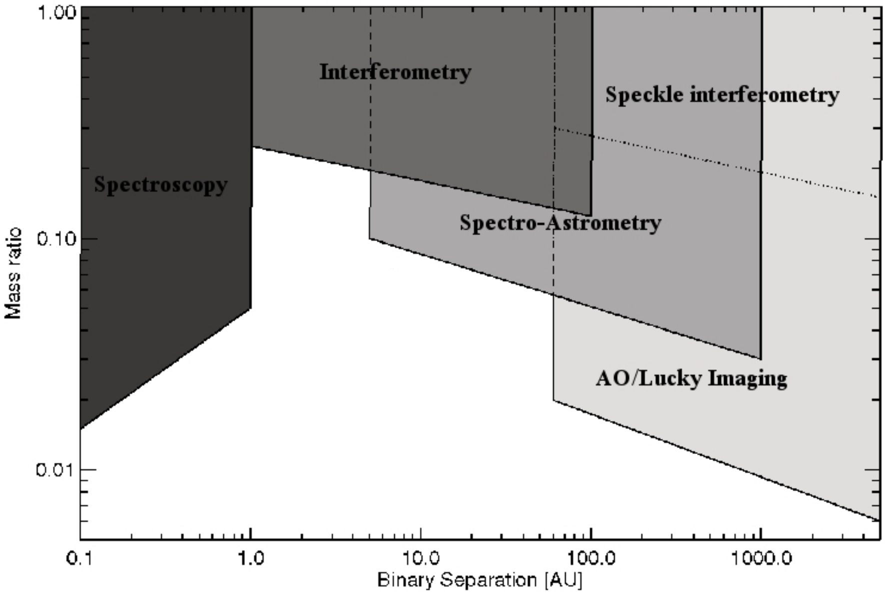

Figure 9.4: *Sketch of the ranges of sensitivity of the different detection methods. Note that in the AO-Speckle frame the minimum mass ratio limit for the Speckle technique is somewhat higher then for the AO imaging.*

used in i' or z' band on 2m class telescopes. Due to almost noise less detectors the use of short exposure images does not result in a big difference compared to long exposures.
Unfortunately the high image frequency entails a small field of view of typically 20″x20″. One thing to note is that up to date infrared detectors are noisy and therefore would strongly limit this application on large telescopes.
Fig. 9.4 summarizes the most important techniques. The spatial resolution is given for a target at a distance of 1 kpc. The given ranges are estimates not exact values. For example one could potentially find spectroscopic companions at separations of 10 AU. But due to the long orbital period other methods are more suitable for the detection of these companions.
As can be seen from the figure in principle all separations could be detected. But many techniques are limited to mass ratios ≥ 0.1. Usually the larger separations enable lower mass ratios to be detected. The only exception here is the spectroscopic technique for that it is opposite. In the field of AO, Lucky imaging and Speckle interferometry, the minimum mass ratio that can be detected using the Speckle technique is somewhat larger then for the other two methods. The AO and Speckle techniques are used on a 8m class telescope in K' band whereas the Lucky imaging is used on a 4m class telescope in z' band. Both yield similar resolutions. For the (optical) interferometry a baseline of maximum 200m was assumed.

Chapter 10

The Cepheus OB2/3 Association

We saw that in order to detect close companions we need high physical resolution. Besides high angular resolution images this requires the proximity of the targets. Further on to provide a statistically significant basis for our sample the number of massive stars in the target area has to be sufficiently large i.e. $\gg 10$. Additionally a low stellar density and a young age strongly reduce the effect of dynamical interactions on the binary parameters.

The Cep OB2/3 associations fulfill these criteria. They are positioned at a distance of ≈ 800 pc (Abraham et al. 1993) to 900 pc (Contreras et al. 2002). We will adapt the closer value of 800 pc. A high number of massive (Simonson 1968, Blaauw 1959) and intermediate-mass (Sicilia-Aguilar et al. 2005, Contreras et al. 2002) stars have been assigned to be members of the two associations.

For associations the stellar density is not higher than that of the field (Jordi et al.1996). The age of the two associations lies between 3 Myr and 10 Myr (Patel et al. 1995, 1998, Sicilia-Aguilar et al. 2004, Blaauw 1964, 1991, de Zeeuw & Brand 1985). The origin of the CepOB2/3 associations and star formation therein will be shortly described in the following.

10.1 The Cep OB2 Association

The Cepheus OB2 association is embedded in the Cepheus bubble. This is a bubble-like structure of atomic and molecular gas (Simonson&van Someren Greve 1976, Patel et al. 1994, 1998) extending about 120pc around the center at RA=$21^h24^m04^s$, dec=$+62°23'18''$. Balazs & Kun (1989), Patel et al. (1995, 1998) derived a model of the bubble and star formation within. From CO emission data and IRAS point sources they modeled the bubble as a shell originating from one or more supernova explosions of the stars of first generation. The next generation star formation triggered by these explosions is taking place on the boundary of the bubble. Already there is a third generation of stars triggered by further supernova explosions. The age estimation based on the expansion of the bubble numbers 7-10 Myr for the center (NGC 7160) and 3 Myr (Tr37) for the rim.

10.2 The Cep OB3 Association

The Cep OB3 association has a similar distance from the sun as Cep OB2 i.e. 800 pc (Moreno-Corral et al. 1993). It covers an area on the sky from approximately 22^h46^m to 23^h10^m in right ascension and +61 deg to +64 deg in declination. It can be divided into two subgroups of different ages (10±2 Myr and 7±2 Myr) by isochrone fitting (Blaauw 1964, 1991, de Zeeuw & Brand 1985). However, these age determinations based on isochrones are model dependent and, therefore, have to be taken with caution. Indeed an age determination from the expansion of the association places it at 0.5 Myr (De Vegt 1966, Garmany 1973, Assousa et al. 1977, Sargent 1979, Trullols et al. 1997). These kinematic methods usually underestimate the age of the association (Brown et al. 1997).

The age difference and spatial separation of 13 pc is the basis of the hypothesis of sequential star formation (Elmgreen& Lada 1977, Sargent 1979). In this model the ionizing radiation from early type stars causes a shock wave to propagate through the cloud. This shock wave makes the cloud gravitationally unstable that results in a condensation into new massive stars.

An alternative model by Assousa et al. (1977) places the origin of the star formation in the younger sub-group to a supernova explosion in the older group. The observational basis of this model was the existence of an HI expanding shell around Cep OB3 first discovered by Simonson & van Someren Greve (1976) from 21 cm line observations. This shell with a radius of approximately 53 pc and an expansion velocity of 35 kms^{-1} was identified as (typeII) supernova remnant with an age of 0.43 Myr. The possible stellar remnant of this supernova is the pulsar PSR 2223+65 with an age of 1.14 Myr. Assousa et al. (1977) proposed supernova induced star formation of the younger subgroup.

However, for the age of a few Myr of the subgroup this event is much too recent to have initiated star formation. Another pulsar, PST 2324+60, with an age of 10 Myr also quoted by Assousa et al. (1977) seems to be a much better candidate to have triggered star formation in both the older and the younger subgroup.

Chapter 11

Observations and Data Reduction

We observed 148 target stars in the Cep OB2/3 region. The list contains high-mass, as well as intermediate-mass targets. The position of the targets on sky is presented in Fig. 11.1.

Observations have been performed at the 2.2m telescope at the Centro Astronómico Hispano Alemán with the AstraLux lucky imaging camera in Johnson z' band. This camera uses an EMCCD as detector that can potentially be used as photon counting device. Therefore the sensitivity for the detection of companions is limited by the flux halo of the primary rather than by read noise effects.

The field of view of the exposures varied between 12″x12″and 24″x24″. Typical single frame integration time was 30 ms. The total exposure time was around 150s. The camera gain was changed such that every target star exhibited approximately the same number of counts on the detector. This makes the samples comparable within the same range of magnitude differences. For the detection of companions at the separation of the diffraction limit we used 1% of the

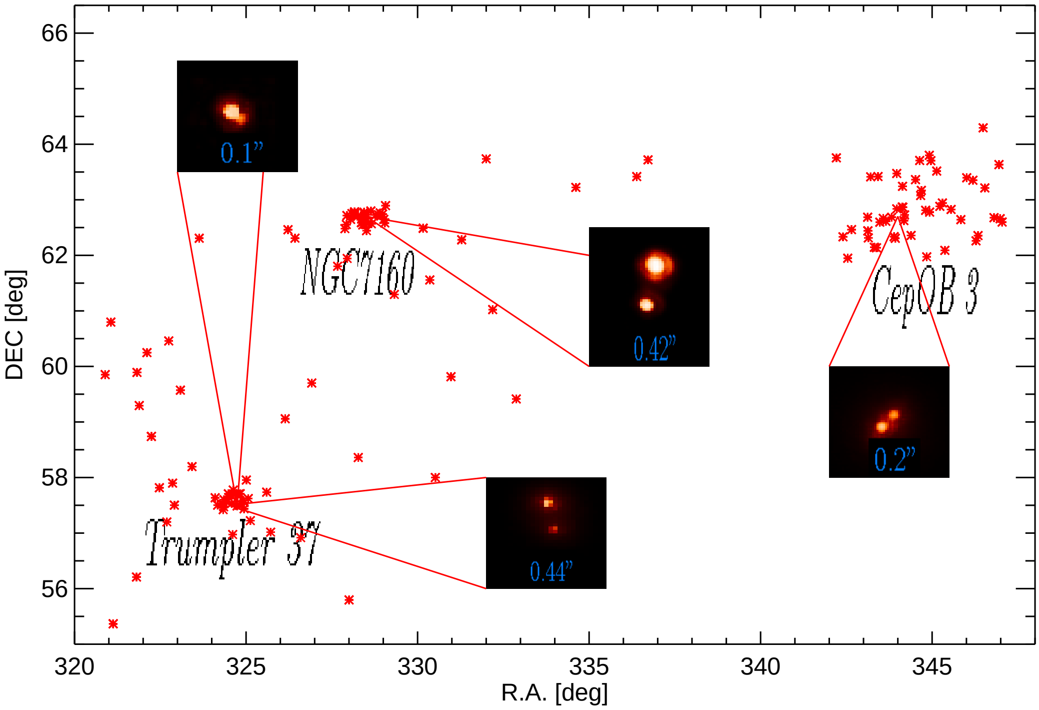

Figure 11.1: *The targets observed with AstraLux. The different regions are shown by name*

single frames to construct the final image. The observed targets are shown in Appendix A, Table 15.

Data reduction was done with standard idl tools. For the sub-arcsecond companions we used a PSF-fitting algorithm. If possible we used a PSF from the same image if not we tried several PSFs and used the best fit. We performed relative photo- and astrometry on the image.The age of the target star was assumed to be 3 Myr for Trumpler 37, 10 Myr for NGC7160, 7 Myr for Cep OB3 and 10 Myr for the rest. Intrinsic B, R, I, V bands of the target stars were derived from the spectral types given in the literature. If the luminosity class was not given we assume the class 'V'. To derive the z' magnitude from standard B, R, I, V bands we used the transformation formula given by Smith et al. (2002)

$$\begin{aligned} r' - z' &= 1.65(R-I) - 0.38 \quad (11.1) \\ r' &= V - 0.44(B-V) + 0.12 \quad (11.2) \end{aligned}$$

We then calibrated the intrinsic brightnesses of the companion stars with these values. To get the relation between the masses of the primary and the secondary we derived the spectral types of the companions by their z' magnitude and took the masses from models (Straizys 1992).

Chapter 12

Binary Parameters

In Chapter 9 we presented different formation channels of binary and multiple stars. Remember that our final goal is to be able to distinguish between the two formation scenarios of stars, i.e. modified accretion and coalescence. This means we have to assign the formation channels presented in chapter 9 to one or the other scenario.

The fragmentation of the pre-stellar core, as well as the disc-fragmentation are assigned to the modified accretion scenario. The same is true for a pure capture scenario without any further evolution. The evolution of an originally wide binary to a close one can only work when both companions accrete from the surrounding medium i.e. for a coalescence scenario. So independent how the companion has been produced in the first place the evolution of the binary due to accretion of circumbinary matter will be assigned to the coalescence scenario. We will however distinguish between global and local coalescence. In a scenario of global coalescence the binaries formed by a capture process before they underwent further evolution whereas in the local coalescence the companions were born by fragmentation of a pre-stellar core before they evolved further. Note that in the disc-fragmentation scenario there is also a potential evolution via accretion of the binary. However, the matter accreted by the two stars has been confined from the beginning within the pre-stellar core itself and we do not count this scenario as coalescence.

So to answer our question how binaries form we have to pin down the channel of binary formation of our targets. In order to do so we will investigate different binary parameters and compare them to the predictions of the models of binary formation:

the CSF can be used to set a border between regimes of potentially different binary formation. Confirmation can be derived from the degree of multiplicity of the objects. We will define this degree of multiplicity as total number of companions over the number of binary and higher order systems i.e. the CSF under exclusion of the single stars. For example the multiple systems of a sample of 10 single stars, 3 binaries, and 1 triple has a degree of multiplicity of (3x1+2)/4 = 1.25.

The mass function (MF) of the companions can be used to test the possibility of a scenario of pure capture without any further evolution of the binary. A comparison of the MF with the Salpeter IMF will decide if this scenario is possible or must be excluded.

The orbital decay via accretion to form a close binary leads to a relation between system mass M and binary separation R (Bonnell et al. 2005) that will be shown in the following:

the angular momentum of a binary in a circular orbit is given by,

$$J \propto M^{3/2} R^{1/2} \tag{12.1}$$

If the in-falling gas has some angular momentum J' then the angular momentum of the binary system as an integral of the angular momentum of the in-falling matter will be proportional to some power of M. For spherical infall the total angular momentum of the binary will remain constant. If on the other hand the in-falling matter has constant angular momentum then the angular momentum of the binary will be proportional to M. Therefore, we can derive a general relation between mass and separation,

$$J \propto M^{3/2} R^{1/2} \propto M^{x} \tag{12.2}$$

and, thus,

$$R \propto M^{2x-3} \tag{12.3}$$

So for spherical infall $R \propto M^{-3}$ and for constant angular momentum of the in-falling gas $R \propto M^{-1}$ as extreme cases. Bonnell et al. (2005) find a relationship of $R \propto M^{-2}$ from simulations that arises from the infall from a turbulent ambient medium adding mass to the growing stars. This model also predicts a correlation between binary separation and mass ratio, as well as between system mass and mass ratio (Bate 2000). These two correlations come to pass : 1. due to Bondy Hoyle accretion and 2. if the amount of matter that is accreted increases the mass ratio becomes more and more independent of the initial conditions. The Bondi-Hoyle accretion rate (see for example Edgar 2004) for a body of mass M moving through a gas with density ρ_∞, velocity v_∞ and sound speed c_∞ (all values taken at infinite distance from the body) is given as,

$$\dot{M} = \frac{4\pi G^2 M^2 \rho_\infty}{(v_\infty^2 + c_\infty^2)^{3/2}}. \tag{12.4}$$

where G is the gravitational constant. In the case of a binary moving through a gas with a sound speed much smaller than the velocity of the stars the ratio of the accretion rates onto the two stars can be calculated to be,

$$\dot{M}_2/\dot{M}_1 \approx \sqrt{M_2/M_1}. \tag{12.5}$$

Therefore, the mass ratio will increase with time and system mass.
Finally the mass ratio distribution of the systems can test a disc fragmentation scenario.

12.1 Individual Objects

Before we turn our attention onto the general binary parameters we present a list of objects with interesting properties in Table 12.1. This includes possible multiple systems from our images, as well as findings from the literature. Potential companions further away than $2\farcs5$ are only reported if they can also be found in the literature.
The first column of the table shows the name of the target. Column 2 and 3 contain the information of the separation and position angle of the companion respectively. Column 4 counts the number of companions to the target. In column 5 we state if this companion is newly detected or already known and if so if we can confirm it.

Table 12.1: *List of multiple systems*

Name	Sp. Type	Sep.[″]	Pos. Ang.[deg]	Comp.	new det.[2]
BHJ5	A0V	0.39	254	1	y
BD+57 2355	A4	0.49	256	1	y
BD+61 2218	B3V	0.46	94	1	y
BD+61 2355	B7IV	0.35	127	2	y
		0.89	3.11		y
BD +61 2357[3],[4]	B0.5-1V			2?	
		4.56	158		nc[5]
BD+61 2397	B9.5V	0.16	9.4	1	y
BD+62 2078	O7V	2.1	101	1	y
BD+62 2125	B1-1.5V	0.1	22	2	y
		2.0	91		y
BD+62 2127[3]	B2IV-V	0.77	193	2?	y
BD+62 2136	B0.5V	1.89	347	1	c[5]
BD+62 2142[6]	B3V			1	
BD+622155[7]	B2IV	1.69	342	2	c[5]
BD+622166	B1V	2.46	17	1	y
Cl* NGC 7160 DG 39	A0	10.19	55.6	0	nc[5]
Cl* NGC 7160 DG 45	A3V	1.64	169	1	y
Cl* NGC 7160 DG 65	A7	2.6	15	1	y
Cl* NGC 7160 DG 682	A2	1.21	291	1	y
HD203025[8]	B2III	0.08	271	2	y
		4.18	275		c[5]
HD203374	B0IV	0.3	298	1	c[9]
HD204827[10]	O9.5-B0V	0.09	184	1?	nc[9]
		3.94	340		nc[5]
HD205329	B5V	0.11	297	1	c[5]
HD206267[6]	O6e	0.11	225	2	c[11]
		1.74	320		nc[5]
HD207538[3]	B0-O9V			1?	
HD208095[12]	B6IV-V			1	
HD208106[13]	B2-3V			1	
HD208392[12]	B0.5-1V	0.1	212	2	y
HD208905	B1-2V	0.42	171.2	1	c[5]
HD208106[13]	B2-3V			1	
HD208392[12]	B0.5-1V			1	
HD208905	B1-2V	0.42	171.2	1	c[5]
HD209339	B0IV	0.97	224	1	c[9]
HD209481[13]	O9V			1	
HD209744	B1-2V	0.36	230	1	c[5]
		14.88, 291	291		nc[5]
		17.51	335		nc[5]

Table 12.2: *List of multiple systems cont.*

Name	Sp. Type	Sep.	Pos. Ang.	Comp.	new det.[2]
HD210478[13]	B1-2V			1	
HD213023	O9V	1.74	345	1	c[5]
HD216629[8],[13]	B2-3IV-V			1	
HD216658	B0-0.5V	0.71	60	1	y
HD216711[13],[14]	B1V	0.76	41	3	y
		1.00	194		y
HD217061[14]	B1V	0.08	324	2	y
HD217174	A1V	0.98	290	1	c[5]
HD217297	B1.5V	0.16	284	1	c[7]
HD217463[13]	B1.5-2V	0.55	14	2	c[9]
HD217966	B7V	0.78	243	1	y
HD218066[12],[13]	B0-1V	0.46	246	2	c[9]
HD218537	B3V	0.2	312	1	c[9]
HD239581	B2V	0.15	343	1	y
HD239649	B3	0.45	328	1	y
HD239675	B5	0.32	54	1	c[9]
HD239676[13]	B2V			1	
HD239767[13]	B0.5V			1	
Cl* Trumpler 37 MVA 497	A1	1.24	42	1	y
Cl* Trumpler 37 MVA 564	A9	1.39	218	1	y
Cl* IC 1396 SBZ 2-46	A0	0.81	76	1	y
Cl Trumpler 37 185	A1	0.08	15	1	y
V497 Cep[8],[13]	B3V+B5V			1	

2: y: new detection, c: confirmation of companion, nc: no confirmation of companion, 3: Elongated PSF, potential unresolved companion, 4: Potential spectroscopic binary (SB) (Blaauw et al. 1959), 5: Dommanget et al. (2002), 6: SB Garrison (1970), 7: SB Pourbaix et al. (2004), 8: SB Hill (1967), 9: Fabricius et al. (2002), 10: Potential SB Mason (1998), 11: Stickland (1995), 12: SB Batten et al. (1978), 13: Eclipsing binary (EB) Samus et al. (2004), 14: SB Doremus (1970)

12.2 Definition of the sample

In order to explore the general parameters of the binary systems we have to define the sample of companions we will assume to be physically bound to the target stars. On the images of the 125 target stars that are members of the Cep OB2/3 association we detect 182 potential companions. To restrain the physical companions we have to limit our sample in both the range of separations and brightness.

To keep the sample as uniform as possible we used the maximum brightness contrast between primary and secondary as criterion rather than an absolute brightness cutoff. This criterion also includes a rejection of all targets where the contrast between primary brightness and back-

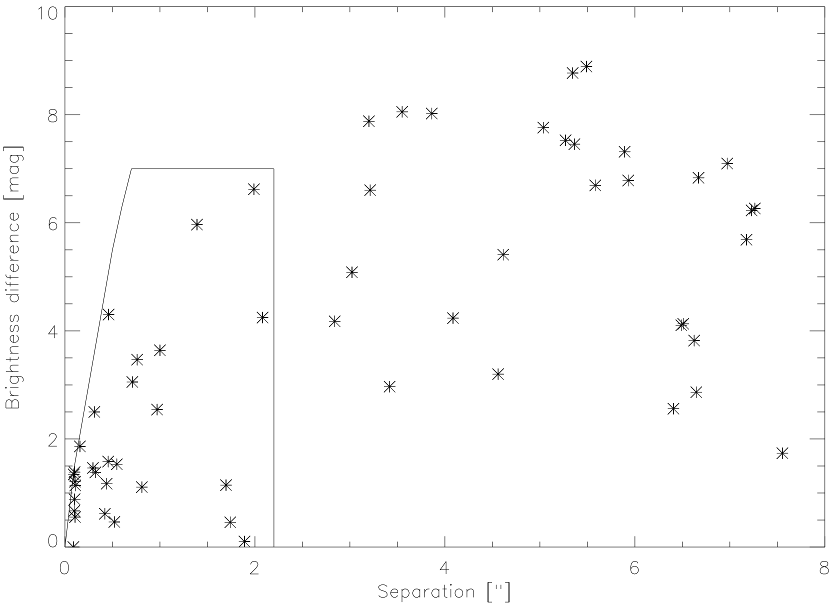

Figure 12.1: *The brightness cutoff for our sample. The left border is given by the detection limit, as upper limit we take the maximum detected brightness difference. The right border is defined by the change in the behavior of the stellar density with separation (see below).*

ground is less than this specified contrast. This means if we apply a too large value for the brightness contrast we will loose some of the targets because they are too faint.

This relative brightness criterion seems natural for this kind of observation because the electron gain of the camera was adapted to the brightness of the primary star such that every primary has approximately the same number of counts on the detector. This also means that the limiting magnitude changes according to the primary brightness. With this criterion we assure that the range of brightness differences is the same for every target. Thus, the range of mass ratios we can detect is also roughly the same for every target.

As cut-off for our sample we use the maximum contrast for that we do not loose targets due to their faintness. This brightness contrast numbers 7 mag (see Fig. 12.1).

Background stars are rejected by their spatial position only. To sort them out we have to use a probability criterion because the observations were performed in one band only. Spatially we limited the sample by the following criterion: from the total number of observations we derived the stellar density ρ in average for the target area. The probability p of two stars at separation d being a chance projection is then,

$$p = \pi d^2 \rho. \tag{12.6}$$

The probability of a star to be a physical companion is, thus, 1-p. For a sample of N observations the number n of chance projections for a given maximum separation between the companions can be derived from the criterion,

$$p^k (1-p)^{N-k} \binom{N}{k} = max. \tag{12.7}$$

For a given p the value of k is calculated from the condition above. This will usually lead to an exclusion of some of the companions as non-physical. These companions are taken to be the outermost companions in the sample because their probability of being fake companions is highest.

Fig. 12.2, left panel, displays the cumulative fraction of companions versus separation. For a better visibility we plotted the square root of the fraction of companions versus the distance rather than the fraction of companions versus area. There is a clear change in behavior around 2.″2 separation. This can be seen more clearly in the right panel that shows the slope of the curve at each separation. Clearly it becomes flat around this point. The position of this border is supported by the fact that if we plot the MFs for the stars outside a border of 1.″8 and 2.″6 the MF for the closer sample starts to become top-heavy. Fig. 12.3 shows the MF for stars further away than 1.″8 (crosses) and 2.″6 (asterisks). Over plotted is the theoretical Salpeter IMF. There is a clear difference between the two measured distributions and only the wider one matches the Salpeter IMF. Therefore, in the following we will use a limit at 2.″2 for a companion to be physical. This separation corresponds to a probability of 0.95 for a companion of a *single* observation to be physical. This means for every 20 possible companions we have to reject 1.

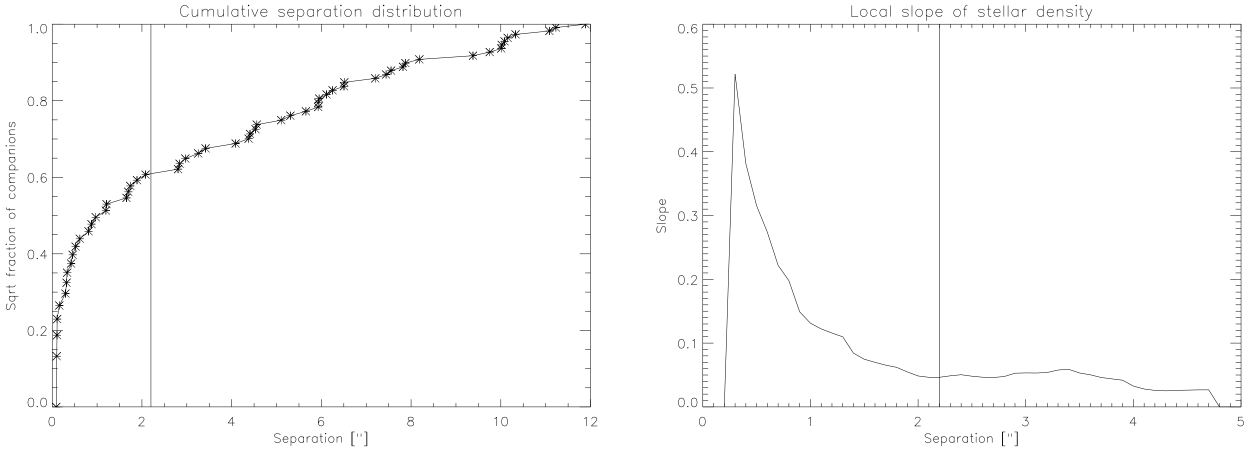

Figure 12.2: *Left: cumulative distribution of separations for a maximum magnitude difference of 7 mag for all possible companions. The behavior changes around 2.″2 (vertical line).*
Right: slope of the distribution.

We still have to account for projection effects: the binaries we can detect are no subject to tidal effects due to their large separations. Therefore, we assume that the orbital parameters are distributed randomly. The observed separation $d(\phi)$ is connected to the true orbital parameters (the semi major axis a, the eccentricity e, the longitude of the periastron ω and the inclination of the orbit i) as (van Albada 1968):

$$d(\phi) = \frac{a(1-e^2)}{1+e\cos(\phi)}[1 - sin^2(\phi+\omega)sin^2(i)]^{0.5} \tag{12.8}$$

from this expression the expectation value of the logarithm of the observed separation d over the semi major axis a can be derived to (van Albada 1968),

$$< ln\left(\frac{d}{a}\right) >= ln(1+\sqrt{1-e^2}) - \sqrt{1-e^2}. \tag{12.9}$$

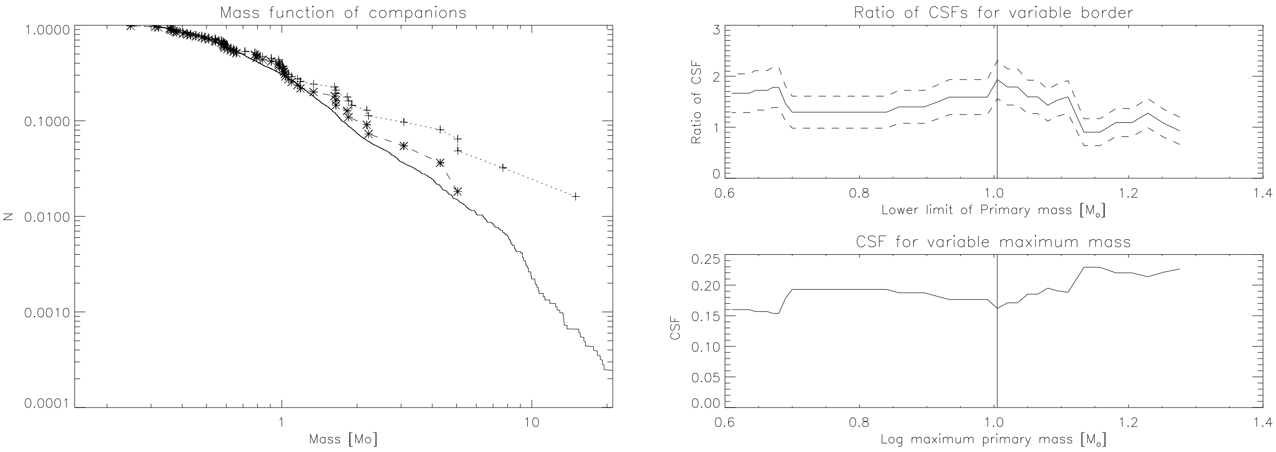

Figure 12.3: *Left: MF for two different maximum separations ($1''.8$ crosses, $2''.6$ asterisks). Over plotted is the theoretical Salpeter IMF. Obviously there is a change in behavior between $1''.8$ and $2''.6$.*
Right upper panel: the variation of the ratio of the CSF of part more massive than the mass border over the CSF of the less massive part.
Lower panel: the CSF up to the given mass border. The dashed lines in the upper plot mark the range of the error. The value of the peak is significantly different from the values at 7 or 14 $M_\odot$. The CSF shown in the lower plot starts to rise after this mass border.

If we assume the semi-minor axis to be randomly distributed the average eccentricity will be 0.5 with a variance of 0.09. This yields an expectation value $< ln\left(\frac{d}{a}\right) >$ of $-0.24^{+0.10}_{-0.06}$. Therefore, all separations must be corrected by a factor of $1.27^{+0.07}_{-0.13}$. In the following we will always use the corrected separations.
The minimum detectable separation is given by the resolution of the telescope in the observational wavelength. In our case this is $\approx 0''.08$. We will use this as inner spatial limit and accept that we have a separation dependent detection limit on our sample. This bias will be referred to as 'observational bias' and be discussed in Sec. 12.4.
Now we have to see if there is really a change in the binary parameters at some spectral type. If yes the mass where this change occurs will define the border between the two sub-samples i.e. high-mass stars and intermediate-mass stars. These samples will in the following be referred to as OB- and AB-stars respectively. To find an appropriate position for the border between the two mass regimes we plot the ratio of the CSF for the stars more massive than the mass border and that for the less massive stars dependence on the dividing mass limit. Fig. 12.1, right upper panel, shows the ratio of the CSF for the sample earlier than the border over the CSF later than the border versus the border mass. The range displayed lies between spectral type B9 (2.6 $M_\odot$) and B0 (20$M_\odot$). There is a clear local maximum around 10 $M_\odot$. The two dashed lines mark the error of the CSF ratio. As can be seen the maximum is significant. The lower panel of the figure displays the CSF for the stars less massive than the border. It clearly starts to rise at the limit we derived. We, thus, will use this border to distinguish between our sub-samples.
Interestingly this limit is consistent with the theoretical mass border around 10 $M_\odot$ between the stars with and without PMS phase. After the definition of the mass border we can counter-check the spatial separation we set as border between true companions and field stars. It turns

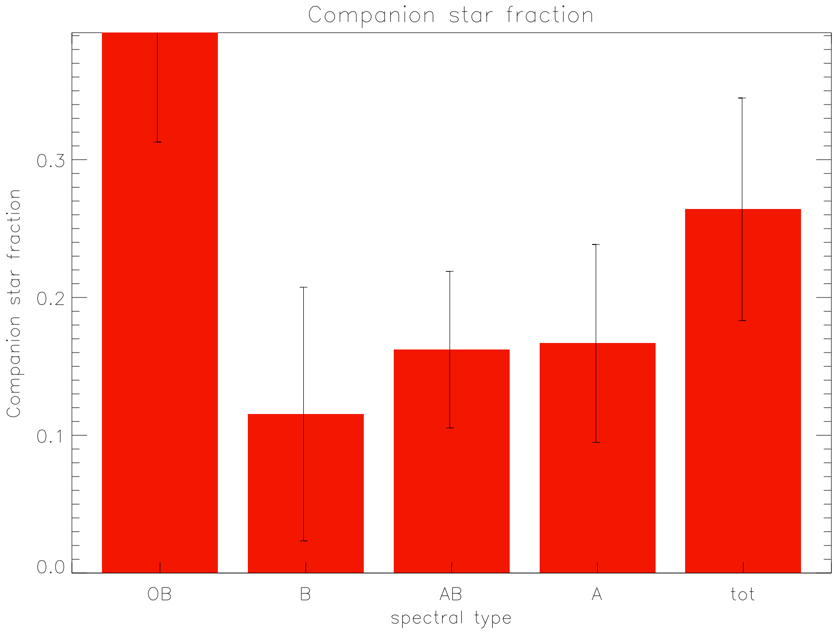

Figure 12.4: *Companion star fraction as a function of spectral type.*

out that for the massive sample there are several binaries with brightness contrast of 1.7 mag or less. The spatial border we defined above includes all the bright companions as physical companions. There is no object similarly bright outside this border. The bright companions outside the border in Fig. 12.1 all belong to intermediate-mass stars. This finding again supports our choice of the spatial border.

12.3 Investigation in the Binary Parameters

After this definition of the sample of physical companions we are ready to explore the parameters of the binary systems. This will be done for the raw data first. However we already discussed that the observations are subject to several biases. So in the end of this chapter we will make the attempt to estimate the number of companions we miss due to this bias and qualitatively discuss how the transition to the complete sample changes the binary parameters.

12.3.1 Companion Star Fraction

As a first step to find differences between OB-stars and AB-stars we present the companion star fraction (CSF): Fig. 12.4 shows the CSF as function of the spectral type of the primary star. It rises toward earlier spectral types yielding values of 0.39 ±0.08, 0.12±0.09, 0.16±0.05 and 0.17±0.07 for OB-, B- ,AB-, and A-type stars respectively. The values of the OB-sample and the AB-sample are significantly different. This is also true for the degree of multiplicity i.e. the number of companions over the number of multiple systems of the two samples. For the OB-sample this degree of multiplicity counts 1.4±0.1 or if we include potential companions also of

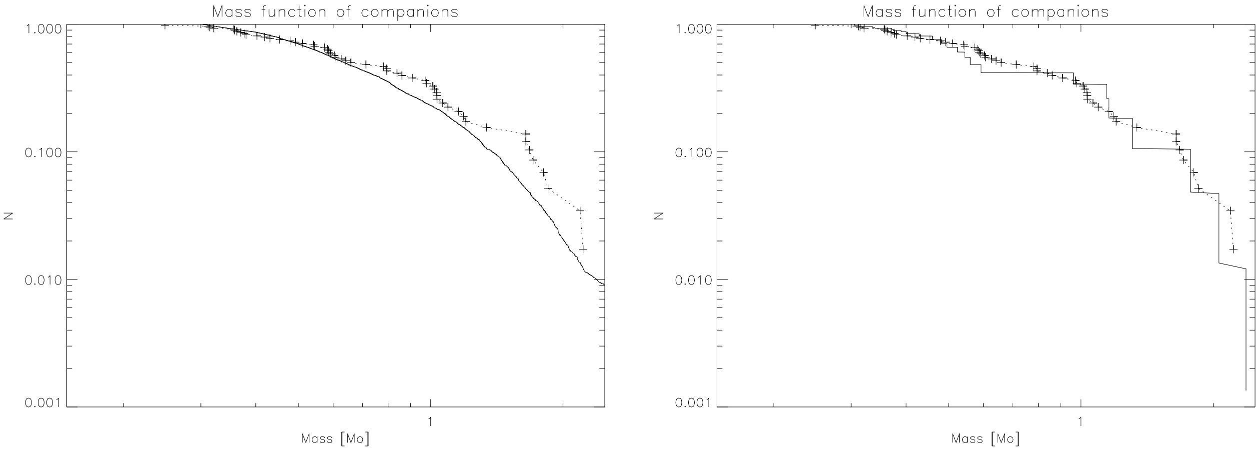

Figure 12.5: *Mass function of companion stars of the AB-sample compared to a Monte Carlo simulation of theoretical Salpeter IMF. Left: the MF seems to be slightly top-heavy wrt. the average Salpeter IMF, right: still the low number statistics allow for a fit between the sample and the Salpeter IMF.*

1.5±0.1. The AB-sample consists purely of binaries.

12.3.2 Mass Function of the Companion Stars

In Sec. 12.2 we used the contrast between primary and companion to define a brightness cutoff for our sample. Thus, for the OB-sample the companions will be in general more massive than those of the AB-sample. In the last section we showed that they are also more frequent within the OB-sample. Knowing that the field stars follow a Salpeter IMF the question is: does the MF of the companions of one or both samples follow the Salpeter IMF? To answer this we will compare the data to Monte Carlo simulations of the Salpeter IMF. To reduce the influence of the bias we will use the entire stellar population as sample. An overabundance of massive stars will still yield a significant difference to the Salpeter IMF.
The theoretical sample is constructed as follows: we simulate a theoretical MF with a minimum mass of 0.1 $M_{\odot}$, a maximum mass of 60 $M_{\odot}$ and a slope of Γ = -1.35. For every target star we apply the following constraints: the maximum detectable mass on the image is given by the mass of the target star itself and the minimum observable mass is given by the detection limit of 7 mag brightness contrast. From every image we construct an observed MF in this way and combine the single observed MFs to a global observed MF. This distribution is compared to the data.
We start with the distribution of the AB-stars. Fig. 12.5, left panel, presents the comparison of the data from the complete AB-sample with a typical MF from the model. The observed MF lies slightly above an averaged Salpeter IMF. Indeed a MF with an exponent Γ = -1.05 fits the distribution. Still the low number of targets can be responsible for the deviation as can be seen in the right panel of the same figure. Additionally if we use only a sample of companions with separations wider than 0.″3 the Salpeter IMF and the MF of companion stars fit well.

For the OB-stars things are different. Fig. 12.6 clearly shows that the OB-star MF is top-heavy for all samples with minimum separation less than 2″ . Let us assume for a moment this

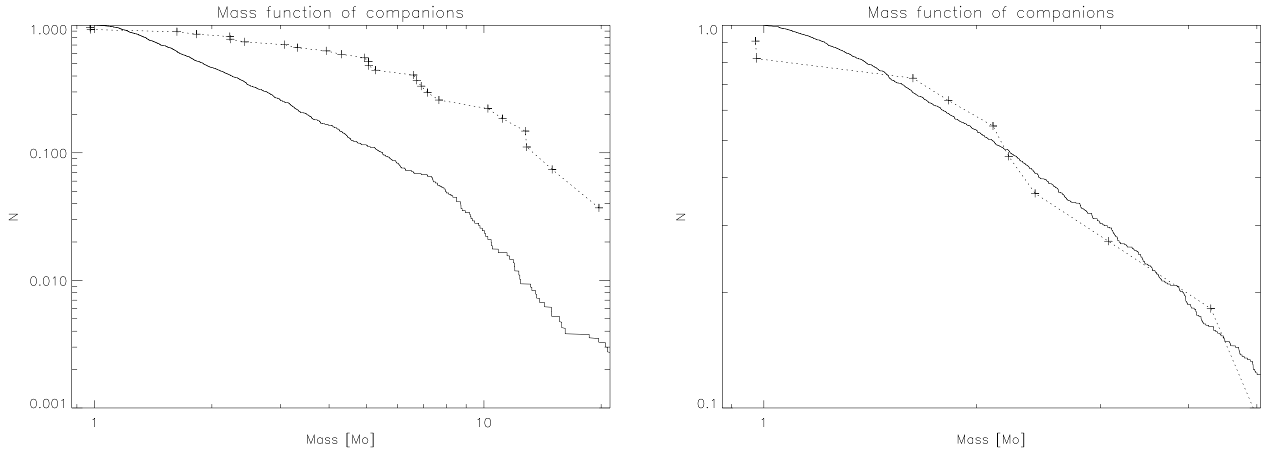

Figure 12.6: *Mass function of companion stars compared to the theoretical Salpeter IMF: left: the complete OB-star sample, right: the OB-star sample for separations larger than $2''$ fits with the Salpeter IMF.*

deviation from the Salpeter law was only due to the observational bias. Then a fit with the Salpeter IMF will provide us with the companions we miss due to our observational biases. This fit however yields more than 300 additional companions with a contrast between 0-7 mag to the primary and closer than $0''.8$. As we certainly did not miss that many stars within these ranges, we conclude that this deviation from the Salpeter distribution is real.

Still the MF of the OB-star sample can be modeled by a single power law. If we change

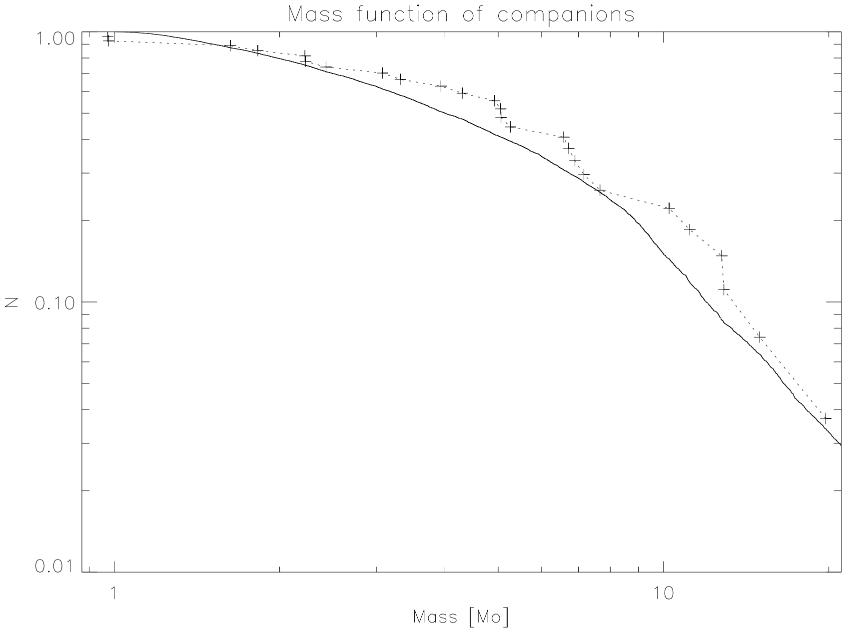

Figure 12.7: *Mass function of companion stars compared to the theoretical MF with an exponent Γ of -0.15.*

the exponent of the MF to Γ = -0.15 as seen in Fig. 12.7 we can reproduce the observed mass distribution of the companion stars.

So it turns out that massive stars have the tendency to harbor massive companions. We will investigate this finding a bit further by exploring exclusively the companions with a brightness contrast less than 1.7 mag to the primary (see Fig. 12.8). They account for approximately 60% of the sample.

12.3.3 The Sample of Bright Companions of the OB-stars

A quick look on Fig. 12.8 seems to indicate that there are three regimes of separations where bright companions to OB-type stars can be found. The question is: can these groups be explained by one single population? This would mean that the orbits probably have high eccentricity and high inclination angles. To investigate this question we assume that the maximum separation within this sample denotes the semi-major axis of the elliptical orbit. To derive the mean eccentricity of orbits around the primary we adapt the distribution f(e)=2e from Duquennoy & Mayor (1991). For ellipses with eccentricities between 0 and 1 the average eccentricity is 0.67±0.1. We assume that the eccentricity and the semi-major axis are the same for the orbit of every companion.

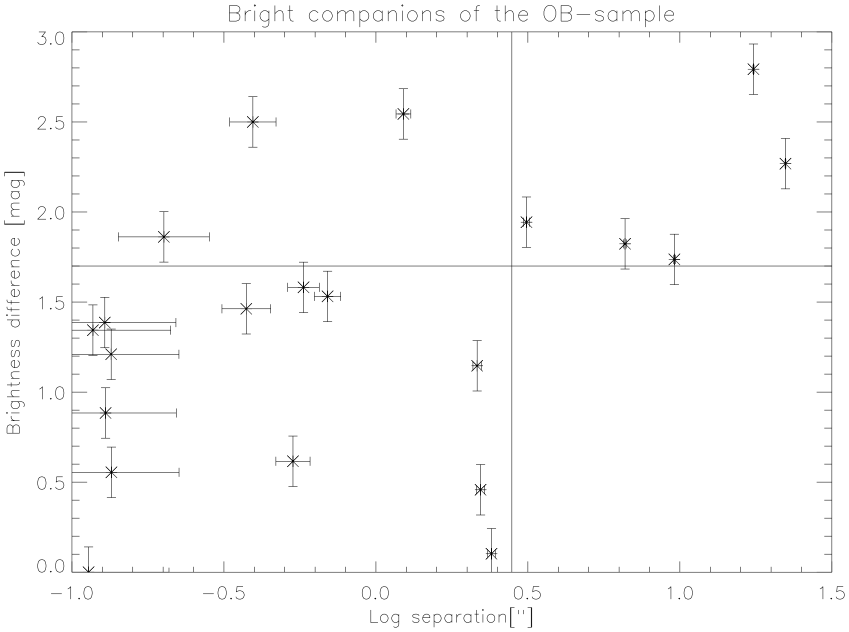

Figure 12.8: *The sample of bright companions to the OB-stars (lower left corner). There is no star with contrast less than 1.7 mag to the primary beyond the border. The three bright stars beyond the border of the sample belong to targets of spectral type B1-B2 i.e. the lower mass end of the sample.*

We will now estimate the probability that we observe the companion at the given distance or closer to the primary:
as first step we derive the average distance R from the primary from the observed separation with Eq. 12.9. As an estimate we further assume that the companions sit on circular orbits at this distance R. This means that the probability to find a companion on any point on the surface of the sphere with radius R around the primary is constant. We only need to calculate the probability that we detect this companion within the projected distance of r on our image. This

probability is just the ratio between the area of an intersection between the surface of the sphere with a cylinder of radius r and the total surface area of the sphere. If $r \ll R$ we can assume that the intersection is flat. The ratio then reads, $p = 2\pi r^2/4\pi R^2 = 0.5(r/R)^2$. The 2 in the denominator occurs because we have two intersections, one on the front and one on the back of the sphere. The error we make using the assumption of a flat intersection is at maximum a factor of 2. This can be seen if we set $r = R$. Then the probability should be 1 (compared to 0.5 as derived by our formula).

We will now test the probability of three samples of companions to have the same orbits: the companions at separations around $0\farcs13$ ($0\farcs11$-$0\farcs15$), at separations around $0\farcs5$ ($0\farcs35$-$0\farcs7$) and around $2\farcs3$ ($2\farcs2$-$2\farcs4$). For a companion at $0\farcs13$ from the primary the probability to have the same orbit as a wide companion at $2\farcs3$ separation is 0.2±0.1%. For a comparison between the companions around $0\farcs5$ and those around $2\farcs3$ we have $r \approx 1/4R$. So the approximation of a flat intersection seems dubious. Still we can estimate probability for these companion to sit on the same orbit to lie between ≈3±1% and ≈6±2%. For the companions around $0\farcs13$ and $0\farcs5$ the approximation of a flat intersection is also questionable. So we will again estimate an upper and a lower limit for the probability. These limits number 4±1% and 8±2% respectively.

We will, thus, state that we have definitely three independent regimes of separations of the companions: Spectroscopic companions, companions with separations up to $0\farcs7$ and wide companions at separations of $\approx 2\farcs3$. Potentially we could divide the sample of companions closer than $0\farcs7$ into two: One around $0\farcs13$ and one around $0\farcs5$. This division stands however on a weaker basis then that into one close and one wide sample.

A look at the degree of multiplicity of the close sample ($\leq 0\farcs7$) shows that it is high: 4 of the 9 companions belong to triple systems and, if we include suspected multiple systems also, this number rises to 7 of 11.

For the sample of stars with companions at separations of $\approx 2\farcs3$ the large gap ($\approx 1\farcs5$) between the inner sample of companions and the outer one makes a bit suspicious. One might suspect that the outer companions are foreground or background stars. However the probability that they are all three chance projections is 0.01% i.e. it is very improbable. Also the fact that there are no more stars as massive as they are further away from the target supports the idea that they are physically connected to the target star. In this sample at least 1 of the 3 systems is triple.

12.3.4 Correlations between Binary Parameters

After this excursion to the bright companions of the OB-sample we come back to the investigation of the entire sample. We have seen that the samples of companions to OB-stars and AB-stars differ significantly in the number and the mass of the companions. In this section we are going to explore how this difference compares with the correlations between the binary parameters discussed in the beginning of this chapter. Here the correlation between two parameters A and B with average values $\bar{A}$ and $\bar{B}$ will be characterized by the linear correlation coefficient x,

$$a = \frac{(A-\bar{A})(B-\bar{B})}{\sqrt{(A-\bar{A})^2}\sqrt{(B-\bar{B})^2}} \tag{12.10}$$

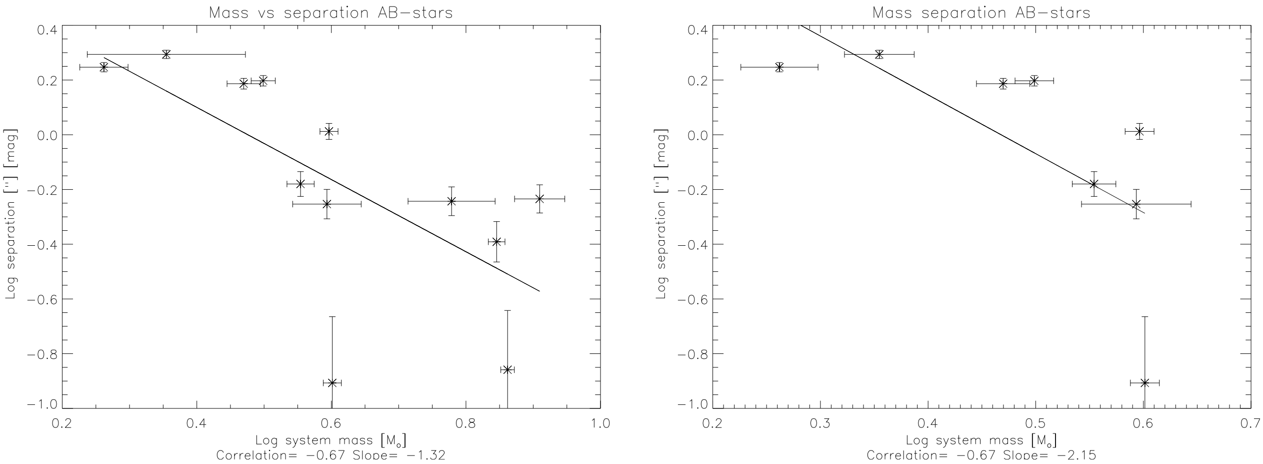

Figure 12.9: *Mass separation correlation for the AB-sample. Left: entire sample, right: targets with masses* $\leq 2.5\ M_\odot$

and the slope of the linear relationship between the two parameters.
To tackle the question if the stars evolve from a wide binary to a close one through accretion, by pure fragmentation of the pre-stellar core, by disc-fragmentation or via capture we will test the three correlations discussed in Sec. 12: the correlation between total system mass and binary separation, the correlation between mass ratio and binary separation and the correlation between system mass and mass ratio. Additionally we will test the correlation between primary and secondary mass because this is predicted to differ depending on the number of star into that a core fragments (Clarke 2001). This investigation will be done separately for the two samples.

The Sample of Intermediate-mass Stars

For the AB-sample it turns out that some correlations strongly differ between the sample of stars with lower masses ($\leq 2.5\ M_\odot$ i.e. pure A-type stars) and the total sample. This sample of lower mass stars is, besides 1 outlier, identical with the sample of systems with separations $\geq 0\farcs6$. So it is almost unaffected by the observational bias and can serve to confirm the correlations between the binary parameters. Due to this similarity between the two samples we will only show the sample of low-mass stars in addition to the total sample. The results of the findings will be summarized in a table at the end of this section.

Fig. 12.9 shows the correlation between system mass and separation for the sample of the AB-stars. The left panel shows the correlation for the entire sample, the right one that for the low-mass stars only.
The correlation between the two quantities for both samples is strong (-0.7). If we set a lower separation limit to $0\farcs6$ we reduce the influence of the observational bias. The strength of the correlation increases (-0.86/-0.74) and the slope changes to -1 for both samples. Thus, we will adapt this value of the slope. The fact that the correlation between mass and separation is preserved for the sample of wide companions indicates that it is no effect of the observational bias.
The correlation between mass ratio and separation for the AB-sample is shown in Fig. 12.10.

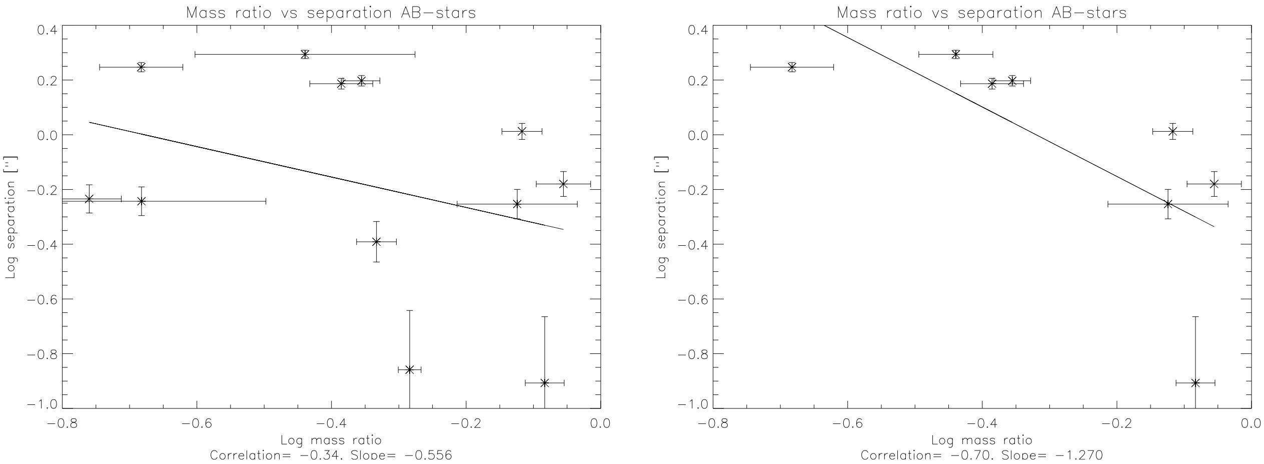

Figure 12.10: *Mass ratio separation correlation for the AB-stars. Left: entire sample, right: targets with masses $\leq$ 2.5 $M_\odot$*

For the entire sample the correlation is weak (-0.34) with a slope of -0.56. For the low-mass sample the correlation is stronger (-0.7) with a much steeper slope of -1.27. If we again only look at the wide companions the correlation for both samples is stronger (-0.86) with a slope of -0.67. So for the change from the wide to the close sample the effect is opposite as expected from the bias and we conclude that the correlation is real.

The correlation between system mass and mass ratio shows a strong difference between the two samples (see Fig. 12.11). For the entire sample of AB-stars we find no correlation between the two quantities. This is surprising because we found a strong anti-correlation between system mass and separation, as well as an anti-correlation between mass ratio and separation. So a strong correlation between these parameters was expected. This correlation exists only for the

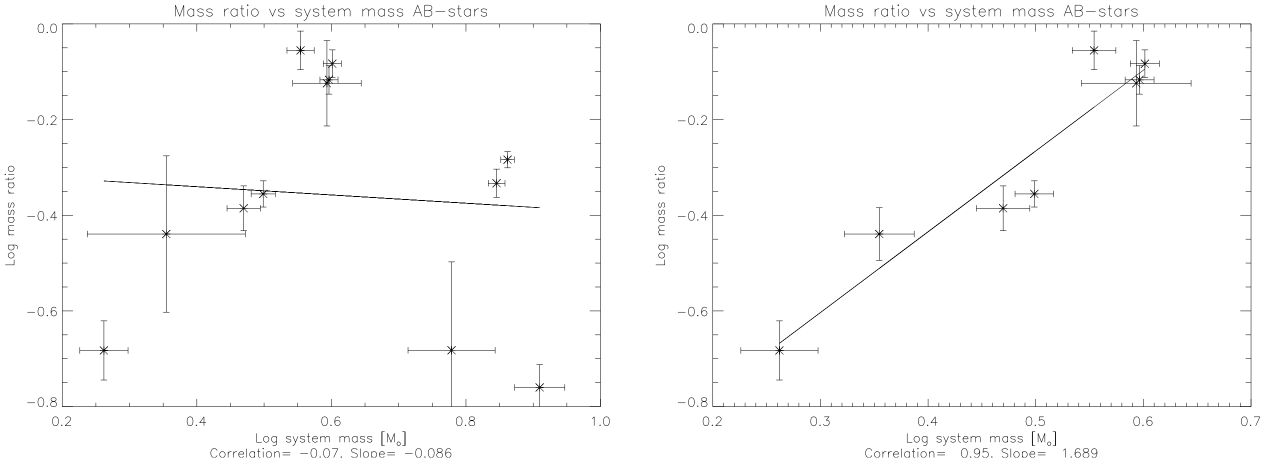

Figure 12.11: *Mass ratio system mass correlation for the AB-stars. Left: The entire sample, right: Targets with masses $\leq$ 2.5 $M_\odot$*

sample of targets with lower mass. For this sample we get the expected very strong correlation between the two parameters. As can be seen from the left panel of Fig. 12.11 a similar slope could be applied to the more massive targets (the four on the right side of the plot) also. These are the only targets with spectral type B. So there seems to be an additional potential border

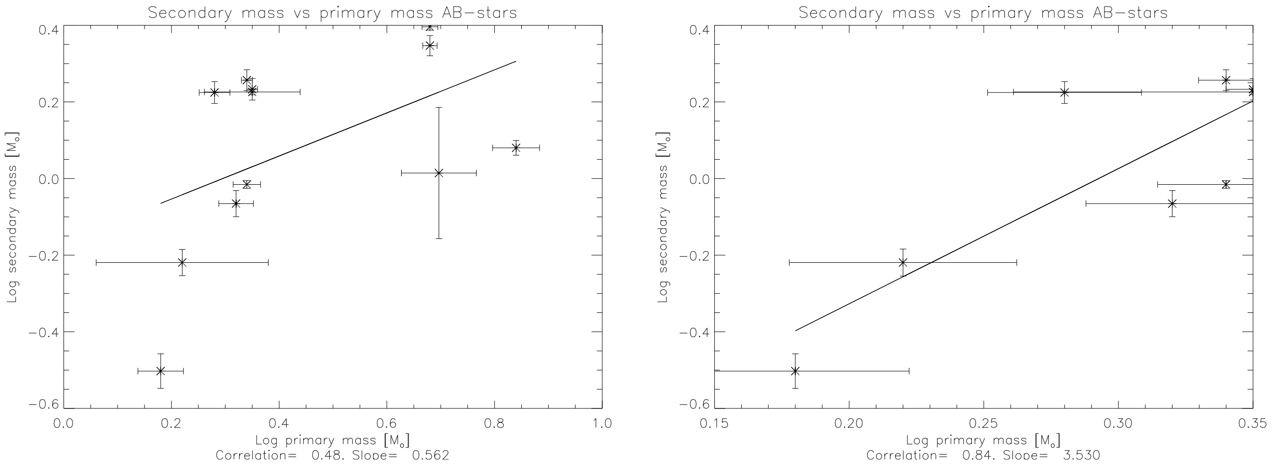

Figure 12.12: *Correlation between primary mass and secondary mass for the AB-stars. Left: The entire sample,*
right: Targets with masses ≤ 2.5 $M_\odot$

in the behavior between A- and B-type stars. Still the number of targets is definitely too low to draw conclusions on this. However it is interesting to note that this different behavior contradicts the expectation form the observational bias that would assign high mass ratios to the more massive stars.

The lack of correlation between system mass and mass ratio does not prevent a correlation between primary and secondary mass. This is shown in Fig. 12.12. For the entire sample of intermediate-mass stars we get a correlation (0.48) with a slope of 0.56. For the low-mass sample the correlation is much stronger (0.84) with a significantly steeper slope (3.53). For the wide sample the correlation and strength of the slope read 0.8 and 3.24 respectively. So there is a strong increase in secondary mass with primary mass. Table 12.3 summarizes the correlation parameters we derived. The first column shows the sample we are investigating. The other columns show the results for the various correlations. We always show if there is a correlation (Corr.) (Here 'y' means 'yes', 'n' means 'no', and 'py' means 'probably yes') and that sign the slope of it has: positive (pos.) or negative (neg.).

Table 12.3: *List of correlation parameters*

Sample	System mass vs Separation		System mass vs Mass ratio		Mass ratio vs Separation		Prim. Mass vs Sec. Mass	
	Corr.	Slope	Corr.	Slope	Corr.	Slope	Corr.	Slope
all targets	y	neg.	py	neg.	n[15]	0	py	pos.
M ≤ $2.5M_\odot$	y	neg.	y	neg.	y	pos	y	pos

15: see discussion to this subject in the text

The Sample of Massive Stars

We have seen that in the case of the massive stars the number of higher order systems especially those including spectroscopic companions is not negligible. In these systems dynamical interactions will play an important role during formation. These dynamical interactions potentially spoil the correlations between the binary parameters. Still we will not exclude the known multiple system from the investigation because we cannot quantify the effect of these interactions. But there are two other corrections to the sample we will perform. One is to exclude the widest companions. They are more than $1''$ further away from the target than the rest of the companions and seem to show a different behavior than the other companions (see Sec. 12.3.3). Additionally we will investigate the sample of B0-B2 stars only. This is because the true O-stars also seem to behave differently than these targets. A possible explanation is that O-stars in general harbor multiple systems with 2 or more companions (even if we cannot detect them) and, therefore, suffer more strongly from dynamical interactions. So in total we will investigate 4 samples. The entire sample, the sample cleared from wide companions, the sample cleared from pure OB-stars and the sample cleared from both the OB-stars and the wide companions. The criteria used for the exclusion of some of the targets will be again examined at the end of this chapter.

We will perform the investigation in the same order as for the AB-sample. Again the parameters for the different samples are summarized at the end of the section.

Fig. 12.13 shows the correlation between system mass and separation for the four samples. Each sample shows an anti-correlation between the two quantities. This correlation becomes stronger when we leave out the wide companions, as well as when we leave out the OB-stars. Consequently the strongest (anti-)correlation can be found for the B0-B2 stars with separations $\leq 2''$. As can be seen on the plot, there is no companion further away than $1''$ for this sample and it is open how much of this correlation is due to the observational bias.

If we try to reduce the influence of the observational bias and use a sample limited by separations of $0\overset{''}{.}5$ and $2.0''$ then we get a correlation rather than an anti-correlation for the sample including all primary masses. The sample of B0-B2 stars still shows an anti-correlation. However it numbers only 6 stars so the finding is on a rather weak basis. Still we did not include the spectroscopic binaries in the investigation. The majority of them belongs to stars of earlier spectral type and the companion is typically very massive as well. So the inclusion of the spectroscopic companion will probably increase the anti-correlation we find here. The conclusion is then that the reality of the anti-correlation we detected is probable.

In Fig. 12.14 we show the correlation between mass ratio and separation for the samples. Again the removal of the wide companions increases the strength of the anti-correlation and the slope of the relationship. The observational bias acts stronger on the samples of closer companions. However if we have a look on the companions with separations between $0\overset{''}{.}5$ and $2''$ there is still an anti-correlation between the two parameters. So we take this trend as real. Again the spectroscopic binaries will add close paires with high mass ratios i.e. support the correlation.

From Fig. 12.15 it is clear that there is always a correlation between mass ratio and system mass. For the B0-B2 this correlation is stronger for the entire sample than for the close sample. This fact indicates that the correlation must be real because the wider companions that increase

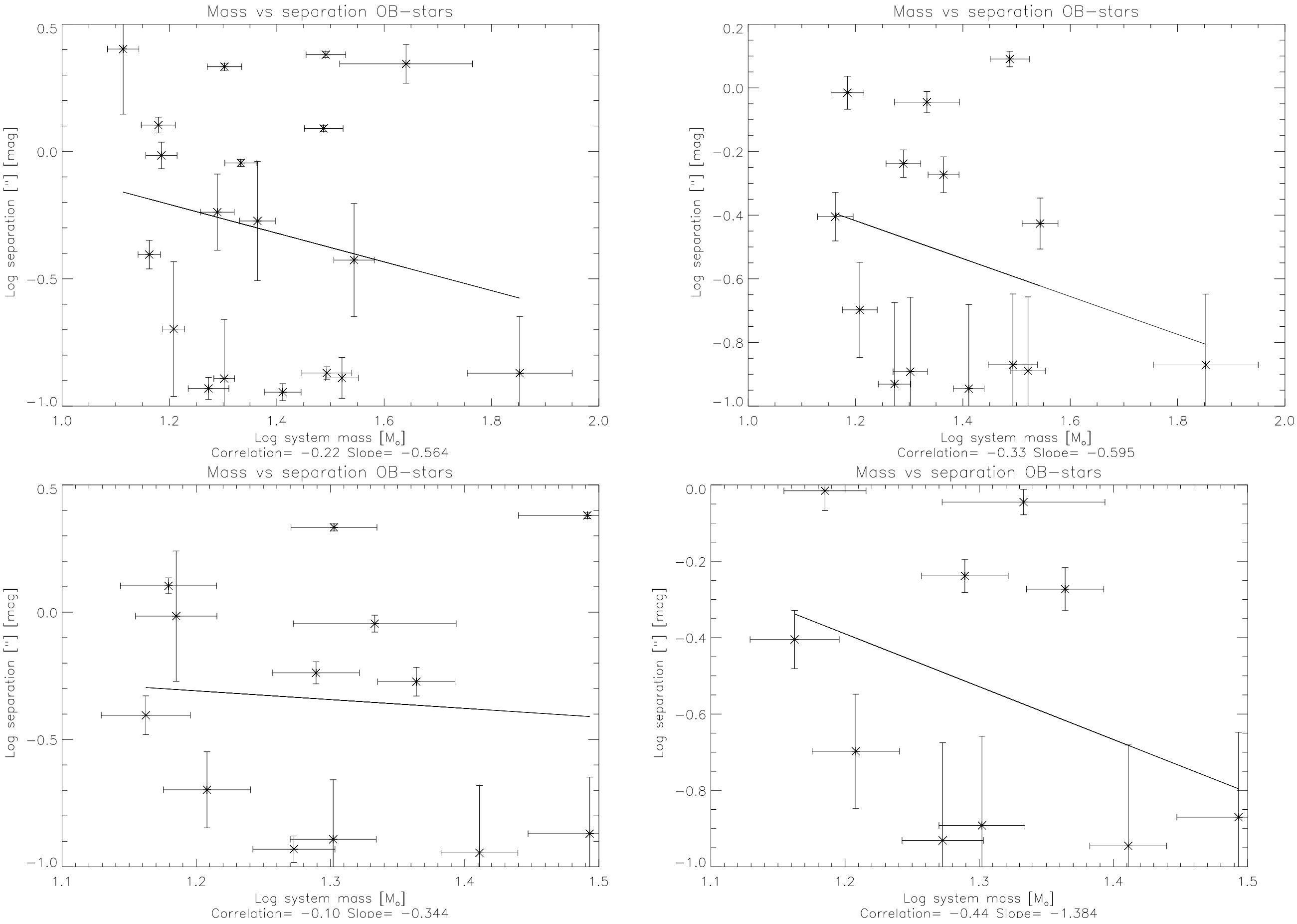

Figure 12.13: *Mass separation correlation for the OB-stars. Left: samples including the wide companions. Right: samples cleared from wide companions. Up: entire sample, down: B0-B2 stars only.*

the degree of correlation are no subject to the observational bias. If we have a look at the samples including all target masses the correlation is weak. This means it is greatly spoiled by the stars of masses greater than 20 $M_\odot$. Still as stated above thend of a correlation between the two parameters seems to be real.

The correlation between primary and secondary masses for the different samples is shown in Fig. 12.16. This correlation has always a positive slope but is mostly weak. Only for the samples including all primary masses the correlation has a significant value (0.6).

If we again use the sample of companions between separations of $0\farcs5$ and $2.0''$ to reduce the influence of the bias the correlation remains for the sample of OB-stars whereas it vanishes for the sample of B0-B2 stars. Still again this second sample numbers only six stars. So we will assume the correlation is real. So it seems that the wide companions, especially the bright ones, as well as the fact that the primary has a mass $\leq 20\ M_\odot$ plays a role for the outcome of the correlations. At least 2 of the 5 systems with companions at separations $\geq 2''$ are higher order multiple systems. One possibility to explain especially the bright stars at these large separations is of course that they by chance are close to the aphelion and, therefore, much further away than the average distance calculated by Eq. 12.9. Additionally the orbit of these companions could, due to dynamical interactions during formation, be highly eccentric. Still as argued in Sec.12.3.3 their

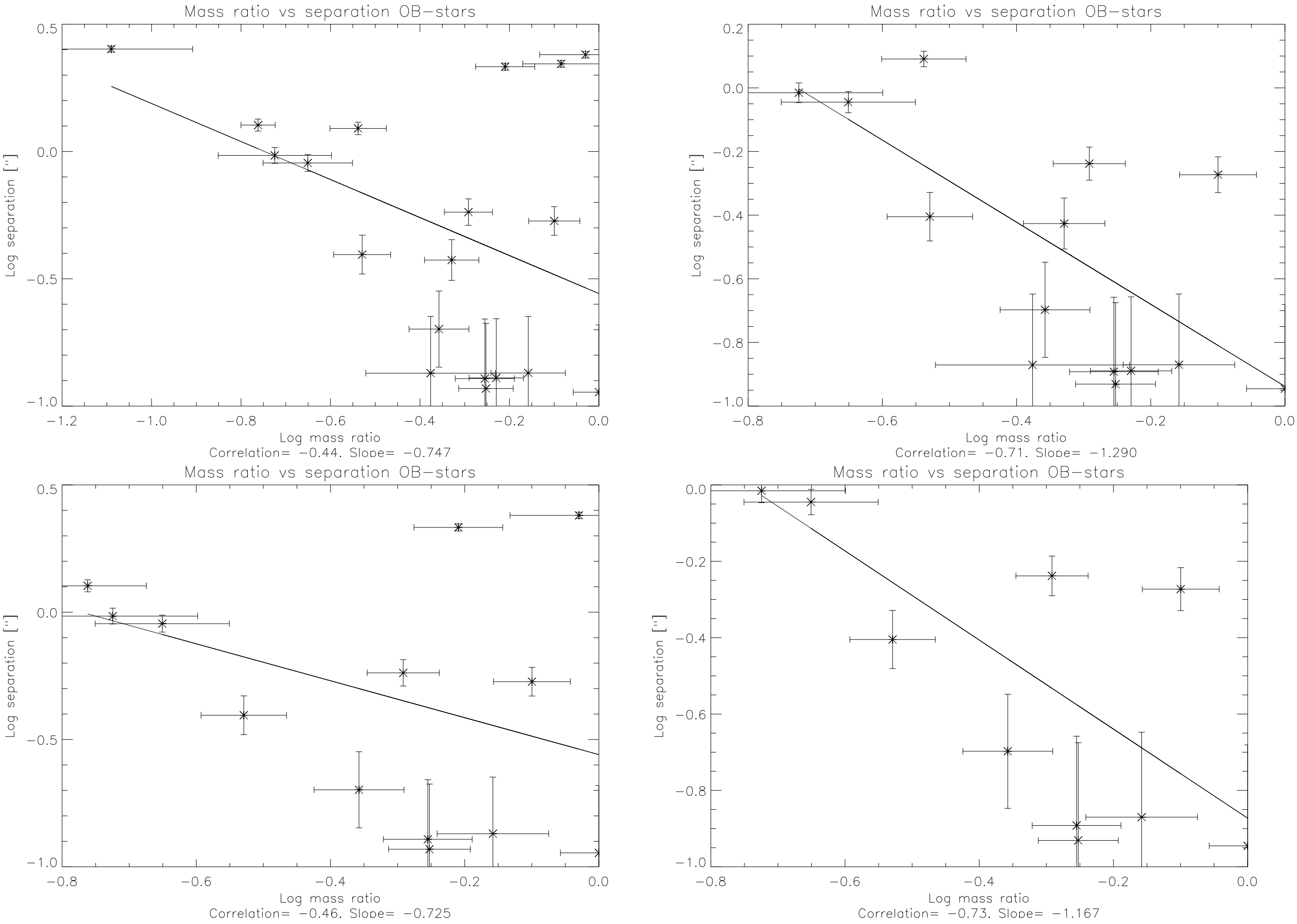

Figure 12.14: *Mass ratio separation correlation for the OB-stars. Left: samples including the wide companions. Right: samples cleared from wide companions. Up: entire sample, down: B0-B2 stars only.*

orbits are clearly different from those of the close companions.

The fact that the stars with spectral type earlier than B0 have such a strong effect on the correlations though they are only few supports the assumption that they harbor more than one companion and potentially went through a phase of strong dynamical interactions.

Indeed O-stars are known to harbor close companions compared to stars with lower mass. So a significant difference between the fraction of close companions of B0-B2 stars and pure O-stars will hint toward companions of the O-stars we miss.

We compare the fraction of close massive companions of the sample of B0-B2 stars with that of pure O stars. The CSF is 0.15 ±0.06 and 0.07±0.06 respectively and, thus, not significantly different. However the samples are too small to be conclusive.

Table 12.4 summarizes the correlation parameters we derived. As for the AB-sample the first column shows the sample we are investigating. The other columns show the results for the various correlations. We always show if there is a correlation (Corr.) (′y′ means ′yes′, ′n′ means ′no′, ′py′ means ′probably yes′, and ′pn′ means ′probably not′) and show that sign its slope: positive (pos.) or negative (neg.).

The final conclusion we draw is that with high probability all the (anti-)correlations we detected are real.

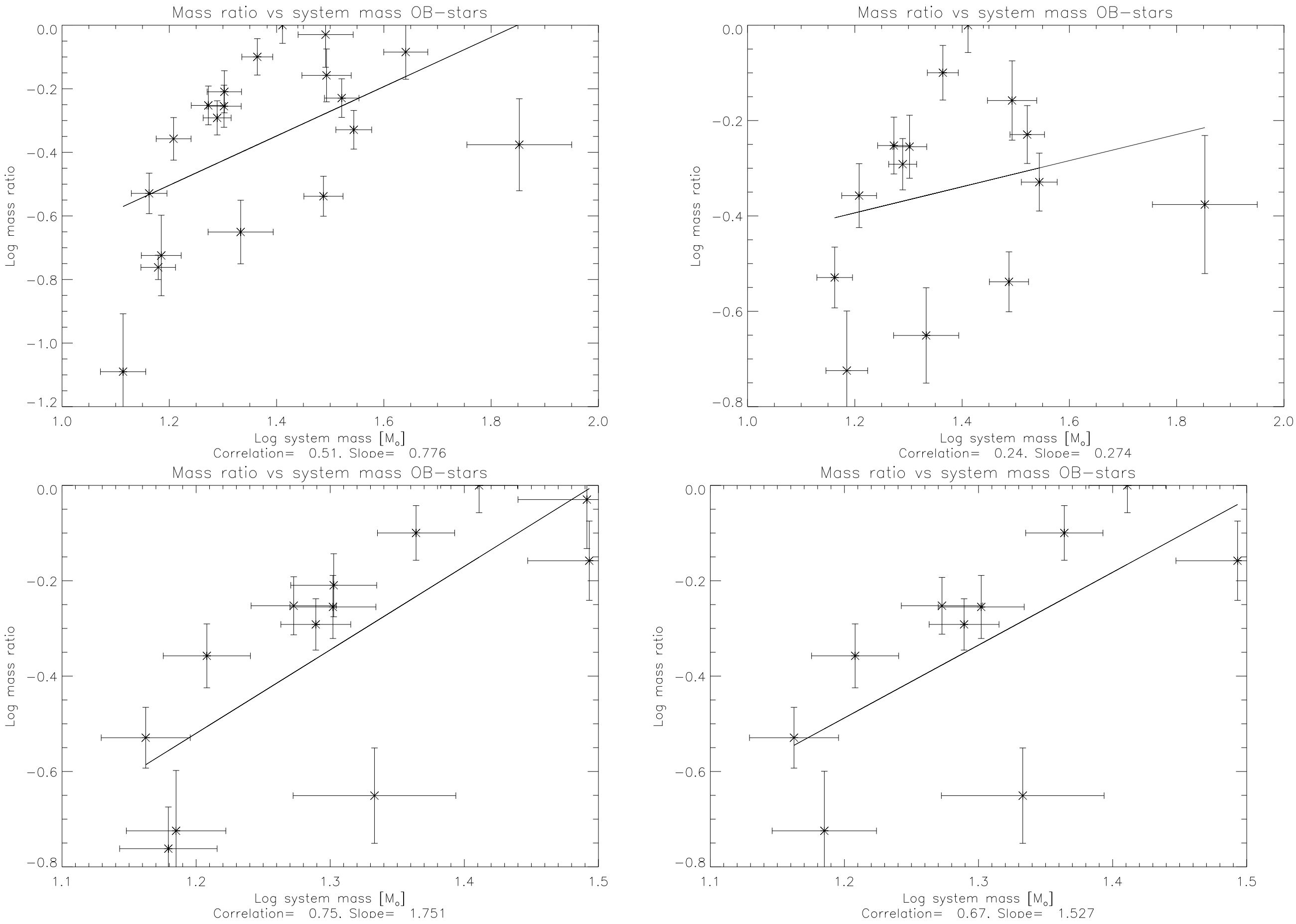

Figure 12.15: *Correlation between mass and system mass for the OB-stars. Left: samples including the wide companions. Right: samples cleared from wide companions. Up: entire sample, down: B0-B2 stars only.*

Table 12.4: *List of correlation parameters*

Sample		System mass vs Separation		System mass vs Mass ratio		Mass ratio vs Separation		Prim. mass vs Sec. mass	
		corr.	slope	corr.	slope	corr.	slope	corr.	slope
All SpecT.	all comp.	py	neg	y	neg	py	pos	y	pos
	Comp. $< 2''$	py	neg	y	neg	py	pos	y	pos
B0-B2	all comp.	py	neg	y	neg	y	pos	py	pos
	Comp. $< 2''$	py	neg	y	neg	y	pos	py	pos

12.3.5 Distribution of Mass Ratios

In Sec. 12.4 we will see that there is no significant difference between the separation-brightness distributions of OB- and AB-stars. Here we want to investigate if this is also true for the distribution of mass ratios. Fig. 12.17 shows the distribution of mass ratios for the AB-star sample.

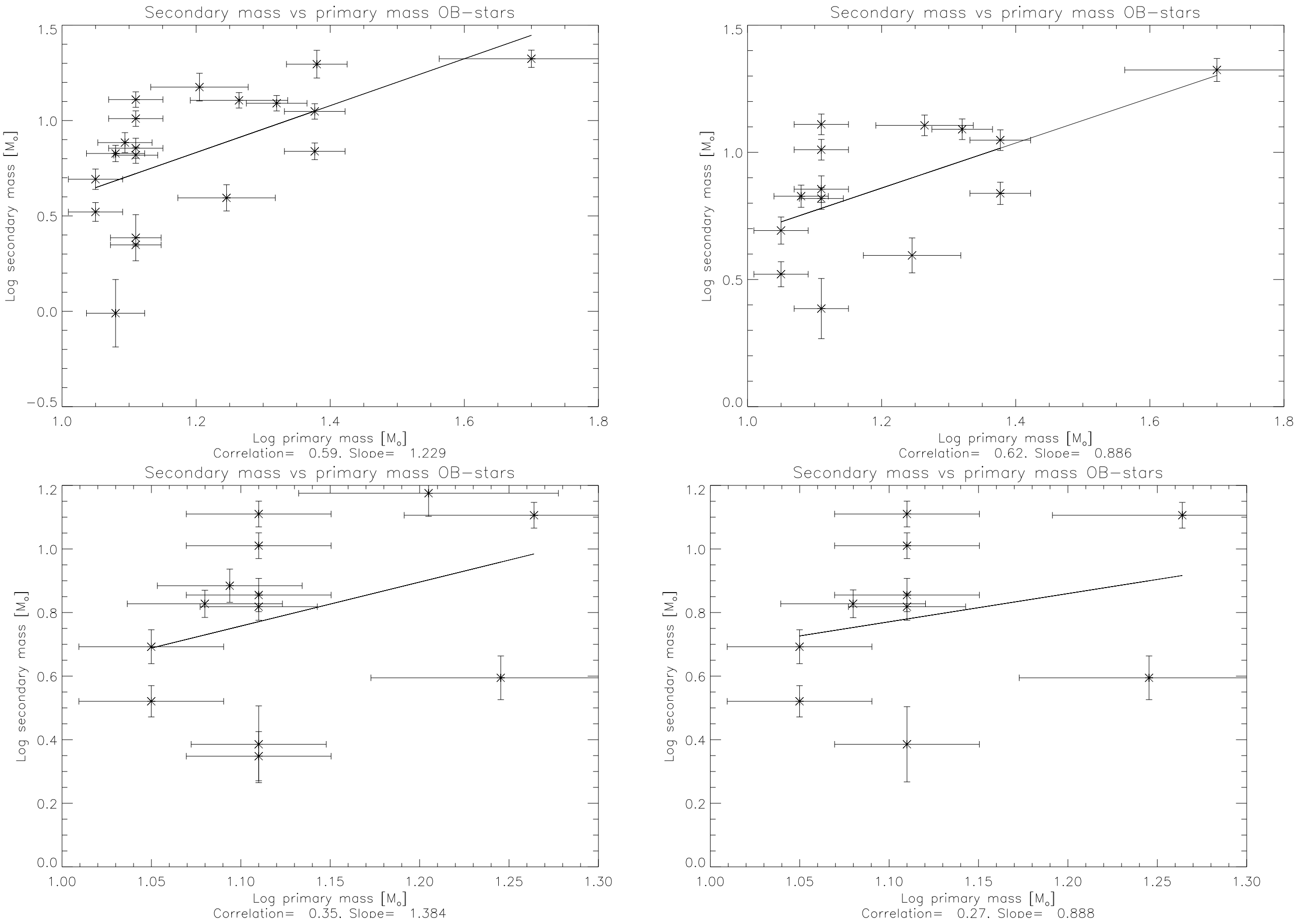

Figure 12.16: *Correlation between primary and secondary mass for the OB-stars. Left: samples including the wide companions. Right: samples cleared from wide companions. Up: entire sample, down: B0-B2 stars only.*

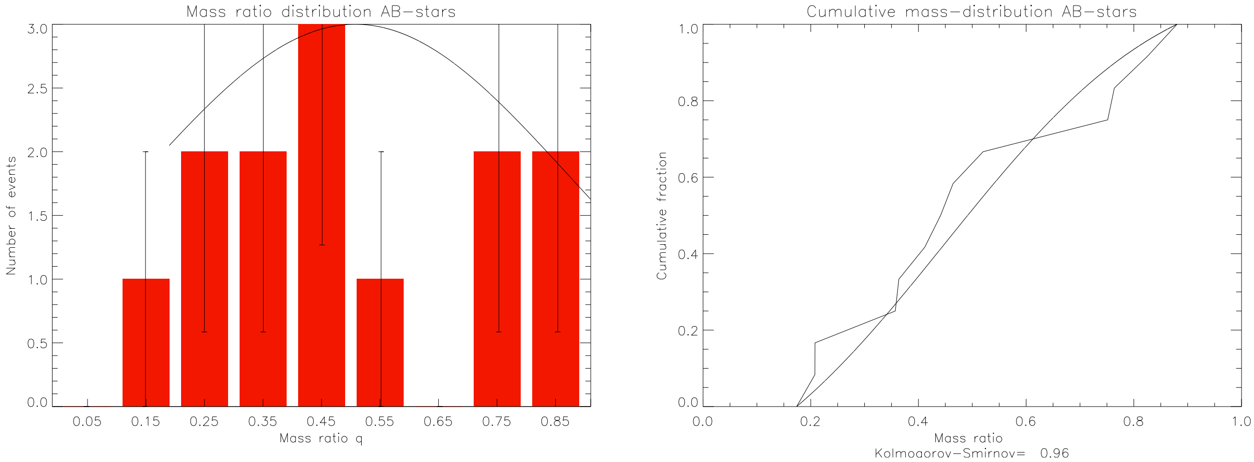

Figure 12.17: *Mass ratio distribution for AB-stars. Over plotted the Gaussian fit. Left: histogram, right: cumulative distribution.*

It is compatible with a Gaussian distribution with a peak at 0.45 and a width of 0.3, as well as with a flat distribution i.e the cumulative distribution has a probability of 0.98 to be drawn from a linear distribution.

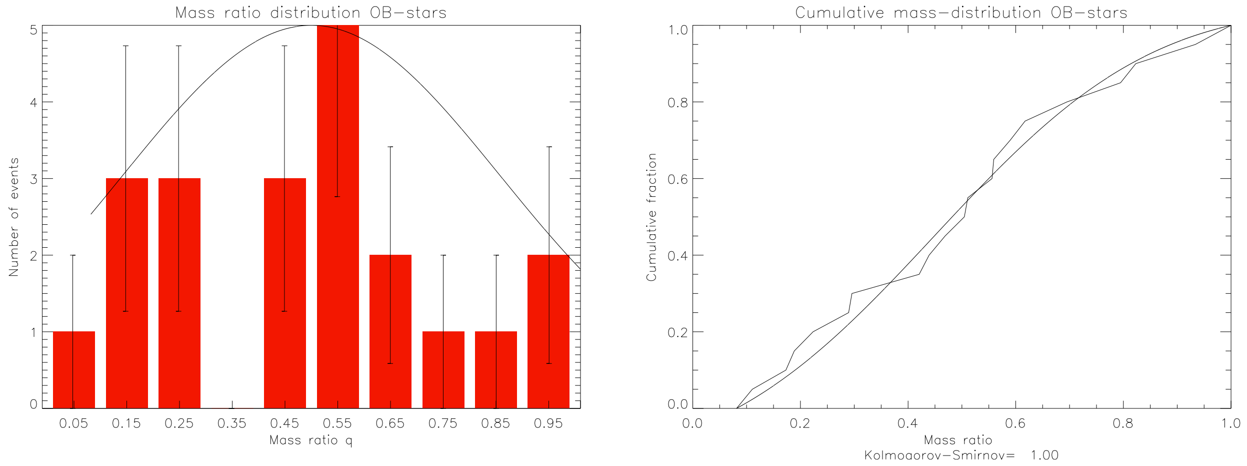

Figure 12.18: *Mass ratio distribution for the OB-star sample. Left: histogram of the distribution, right: cumulative distribution. Over-plotted is the Gaussian model derived from the cumulative distribution.*

The mass ratio distribution of the entire OB-star sample is similar. In fact the Gaussian fitted to the distribution is the same as for the AB-sample. However if we turn the attention to the companions further out than $0\farcs5$ in order to reduce the effect of the observational bias the distribution of the OB-sample tends toward lower mass ratios whereas for the AB-sample this does not occur.

12.4 Completion of the Distribution

Now we turn our attention to the effect of the correlation between separation and dynamical range of the observation. Fig. 12.20 shows the brightness difference versus the logarithm of the separations for OB-and AB-stars (left and right panel respectively). We will apply two different methods to get a rough estimate of the number of companions we miss due to the observational bias. The first method uses the densities in the areas surrounded by the straight lines in Fig. 12.20. The underlying assumption for this to work is that the ratio of densities does not change between two neighboring rows or columns i.e. that the brightness contrast and separation are truly independent.

If for example the closer stars have a clear tendency to be brighter then we will overestimate the effect of the bias. In Fig. 12.19 we show the separation versus brightness difference for the sample for OB-stars and for AB-stars (left panel and right panel respectively). To reduce the effect of the observational bias and still have a significant number of stars in the sample we set the minimum separation to $0\farcs4$. For the OB-sample there is no correlation between the two quantities. However for the AB stars there is a correlation with a linear correlation coefficient of 0.6 and a significant linear slope of 3.7. This means that a fit taken from the companions with separations larger than $0\farcs4$ and applied to the entire sample will overestimate the number of missing companions. In fact if we follow the red dashed line that represents the correlation between separation and contrast on Fig. 12.20 we see that we miss almost nothing.

For the second method we just assume the total density of points to be constant over the entire

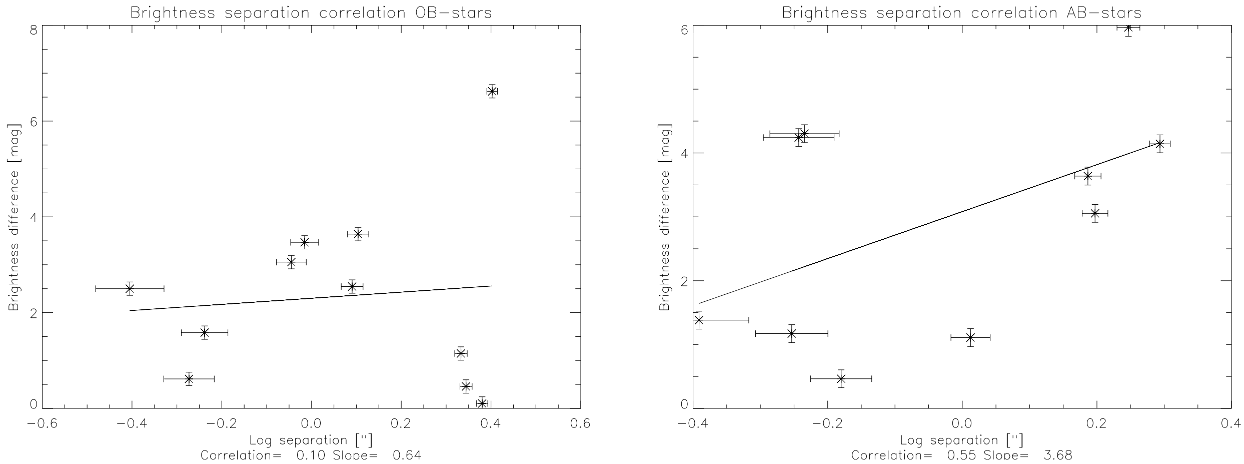

Figure 12.19: *Correlation between binary separation and brightness difference for binaries with separations larger than 0.″4. Left: OB-star sample. There is no correlation. Right: AB-stars. Obviously the brightness difference increases with separation*

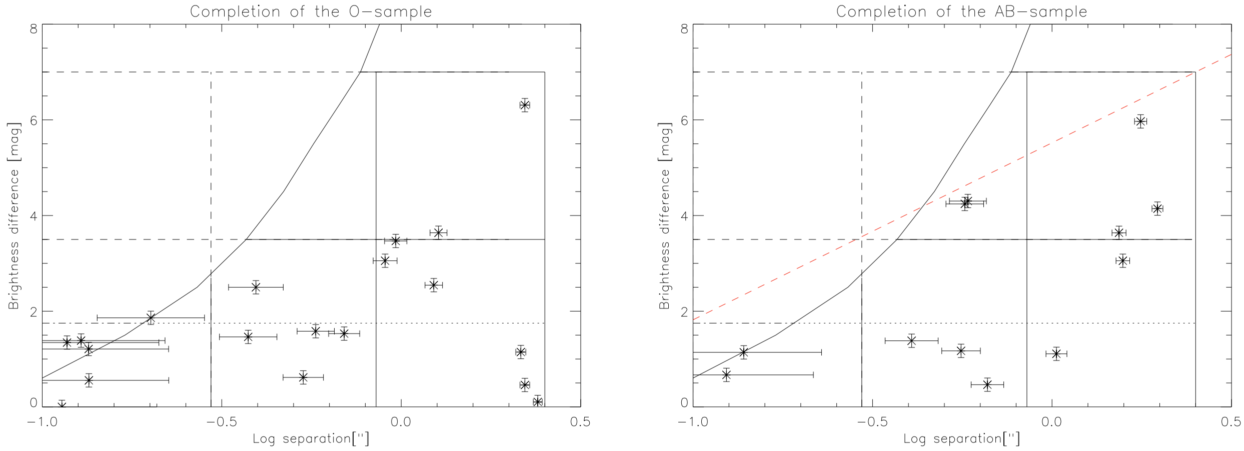

Figure 12.20: *Brightness difference versus separation for the different samples. Over plotted are the dynamic range (left border) and auxiliary lines framing areas of the same size in $\Delta m \Delta \log(r)$. Left: OB-stars, right: AB-stars. The red dashed line marks the slope of the correlation between brightness contrast and separation.*

area. As example we derive the completion of the AB-sample with the two methods. For the moment we will not take the correlation between brightness contrast and separation into account but rather try to get an upper limit of the number of companions. A lower limit will be derived later by taking the red dashed curve as true upper limit for the brightness contrast.
Method 1:
As basis for the completion we use the segments on the plot that lie (almost) fully within our detection range: the two on the right and the one in the lower middle. As first step we complete the segment in the upper middle. The number of missing companions can be derived by the assumption that the ratio of points between the upper segment in the middle and the lower one is the same as that between the two segments on the right i.e. 3:2. The ratio we measure in the middle is 2:3. So we have to add 2.5 stars in the upper part of the column in the middle to

raise the ratio to the desired 3:2. Next we complete the lower part of the column in the left. The part below the dotted line of the segment will be completed under the assumption of a constant density within the area. The corner we miss here has 19% of the total area. We calculate the number of missing companions to 0.38 within this corner. The part above the dotted line will be completed by the same method as before. To increase the number of points involved and, thus, decrease the influence of statistical errors we compare the average of values from the column in the middle and on the right (0:3, 1:1) to the ratio we find in the left column. This procedure yields a loss of 1.19 companions for the part above the dotted line. The ratio between the two segments of the column in the left must be the same as that between the two quadrants on the right i.e. 3:2. If we fulfill the requirement we get 5.4 companions there. Altogether this makes about 7 companions we miss. Due to the low number of targets this method suffers from large statistical uncertainties e.g. in the upper part of the column in the middle between 0 and 10 missing companions are consistent within the errors. So a confirmation by the second method will put the finding on a firmer basis. If we assume that the density of points within the plot is constant we get 6 ± 1.5 additional companions. Thus, both methods agree within the errors.

If we take the red line as upper limit of the brightness contrast the only companion we potentially miss lies in the upper half of the lower left segment.

For the OB-star sample the derivation is a bit more tricky and it is more uncertain if it can be applied because of the accumulation of bright close companions. Surprisingly we do not find a correlation between separation and brightness contrast. We will again use both methods to get a good guess of the number of the undetected companions.

The first procedure yields additional 11.7 companions. If we again assume a constant density of points we end up with 9.5 ± 2 additional companions. So again the methods agree and we take the 11.7 companions as number of companions we miss. If we take the accumulation more serious and assume that we do not have any star in the upper left segment we miss only 6.4 stars.

With the method above we tried to estimate the companions lost due to the varying dynamic range. We still have to complete the sample for the companions we miss due to the cut-off in contrast and separation we apply. To estimate the number of companions we loose due to the total brightness limit of 7 mag difference we fit a normal distribution to the distribution of brightness differences and estimate the area we miss. Fig. 12.21 and 12.22 display the distributions for OB- and AB-stars respectively. The fit was performed for a sample with separations larger than $0\farcs4$ to reduce the influence of the bias. A goodness of the fit is estimated by a Kolmogorov-Smirnov test between the model and the cumulative distributions (right panels). The probability that the fit and the data are drawn from the same original distribution is shown on the bottom of the image. As an additional constraint the area of the curve on the plot should account for the missing companions derived before. The Gaussian models have the following parameters: the center at 1.1 mag and a width of 3.2 mag in the case of the OB-sample and a center at 1.1 mag and a width of 2.7 mag for the AB-sample. So they are almost identical. We find that the percentage of companions missed for the OB- and AB-star distribution are 1.0% and 14.1% respectively.

The alternative model of a flat distribution for the OB- and AB-star sample has the probability

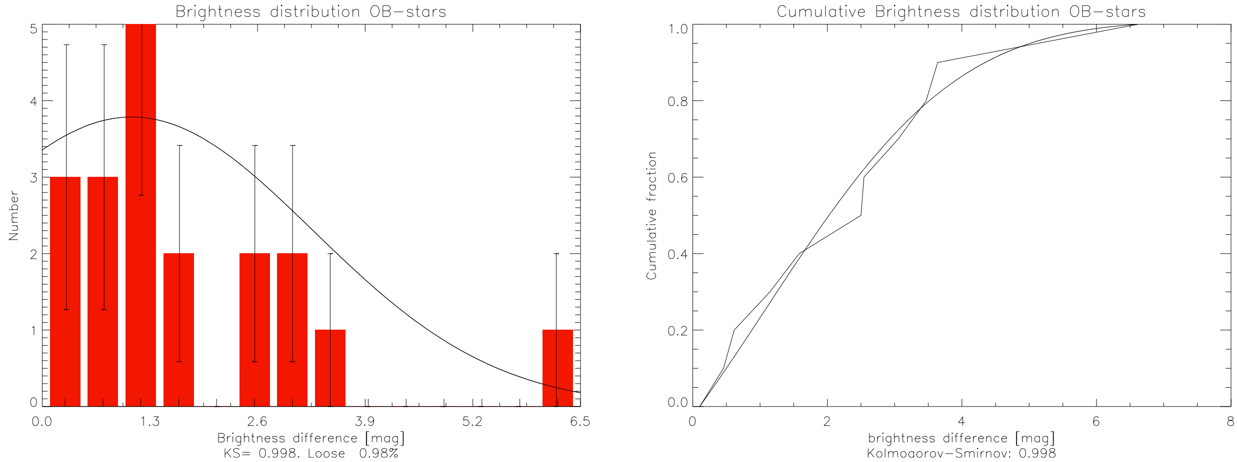

Figure 12.21: *Brightness distribution of the companion stars of the OB-star sample. Left: histogram of the distributions. Over plotted is the best-fit model. The probability and the percentage of lost companions are displayed on the bottom. Right: cumulative distribution of the brightness differences. This distribution is used to derive the best fit model (over plotted).*

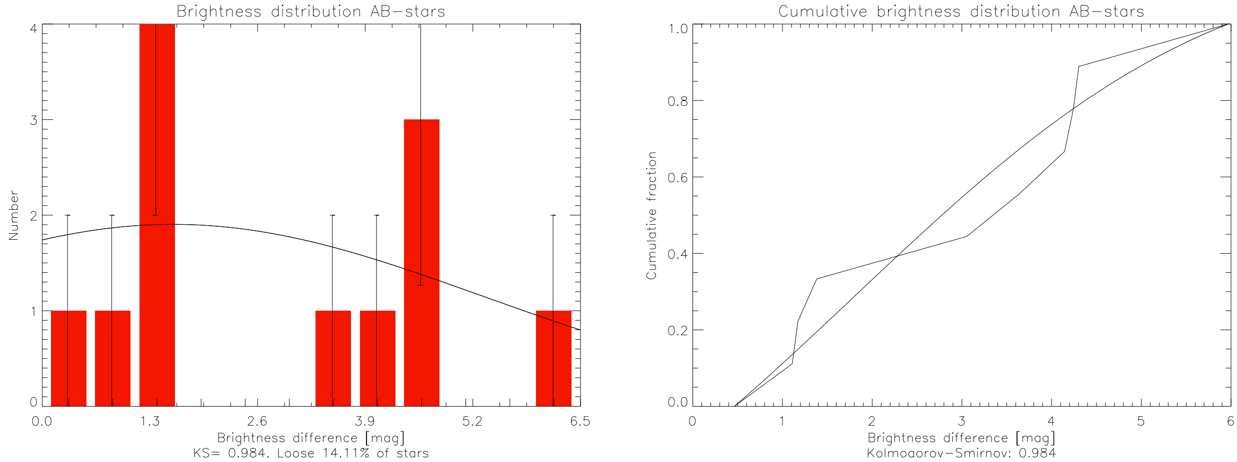

Figure 12.22: *Brightness distribution of the companion stars of the AB-star sample. Left: histogram of the distributions. Over plotted is the best-fit model. The probability and the percentage of lost companions are displayed on the bottom. Right: cumulative distribution of the brightness differences. This distribution is used to derive the best fit model (over plotted).*

of 0.81 and 0.97 respectively. So for the OB-star sample we use preferably the Gaussian distribution. In the case of the distribution of the AB-sample the agreement is good but we would need to set a cut off for the largest brightness difference. For this reason we also prefer to use the Gaussian that is relatively broad anyway.

To complete the distribution of separations for the companions we do not detect due to their large or close separations we assume a log-normal distribution of the separations as found for low-mass stars by Duquennoy & Mayor (1991). As will be seen in the plots this fits the true distribution for AB-stars quite well. In the case of the OB-star sample we need two distributions to describe the data. The fit will be performed for a sample with brightness difference lower than 3 mag to reduce the influence of the bias. To test the goodness of the fit we again perform

a Kolmogorov-Smirnov test between the data and the model.
For the AB-sample we have to take into account the correlation between brightness difference and separation.
Fig. 12.23 and 12.24 show the histogram of the distribution of separations for OB- and AB-stars respectively. Over-plotted are again the curves underlying the best fit to the cumulative distribution under the constraint that the total area on the plot must account for the missing companions derived before. For the OB-stars we use a combination of two Gaussians. One Gaussian is centered at log(r) = 0.2 with a width of 0.7 the other is centered at log(r) = -0.9 with a width of 0.1. Here we have the problem that the distribution peaks toward the inner cut-off and, therefore, we can complete the sample with any curve having a maximum at this position or toward closer separations. We used the fit with the minimum loss of companions that has the peak as far to the right as possible. Therefore, we get a lower limit of the companions we miss. The percentage of companions we miss for the two Gaussians numbers 47.2% and 38.7% for the outer and inner distribution respectively. For the AB-stars we fit a Gaussian with center at log(r) = 0.5 and width 0.6. From this fit we calculate 32.5% missing companions.

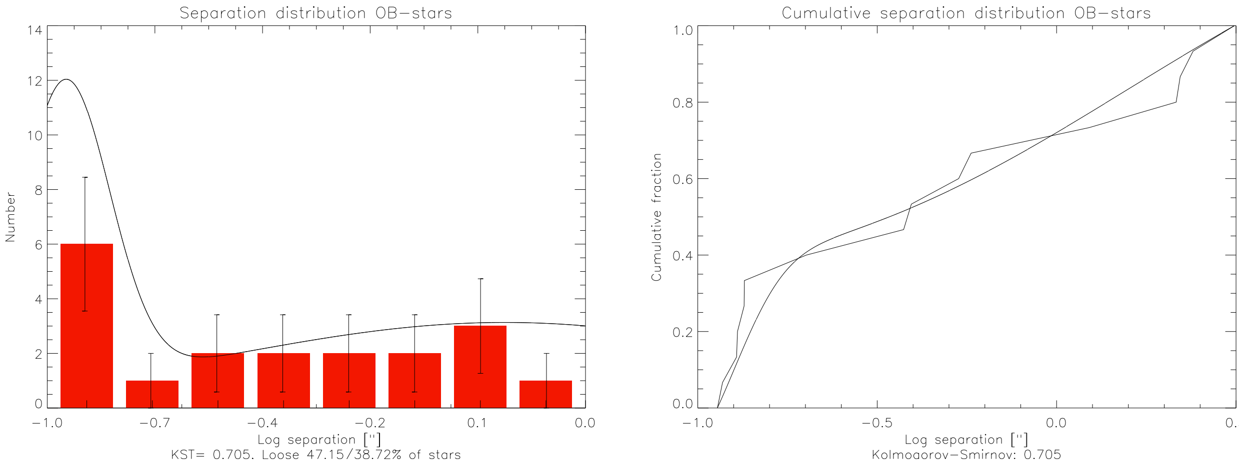

Figure 12.23: *Distribution of separations for the OB-star sample. Left: histogram of the separations. Over plotted is the best fit to the cumulative distribution. Right: cumulative distribution for systems with brightness differences less than 3 mag. The best fit model is over plotted.*

Again we also tried to fit a flat distribution. For the OB-star sample the goodness of the fit is 0.71. The steep increase for close separations seriously questions this model. For the AB-sample the flat distribution fits to 100%. But again the argument that we need some cutoff makes the Gaussian fit technically more preferable.
With the results from the last section we will now extrapolate from these numbers to discuss how the binary parameters will be affected by this completion of the sample.
First we will estimate the increase in the CSF if we account for the bias. For the OB-stars we loose 11.7 stars for the inner distribution of separations due to the bias. Due to the cut off at 7 mag we miss another 0.26 stars. Finally the limited range of separations yields another combined 16 stars on the inner and outer border. Altogether this yields a CSF of 0.90. We did not yet account for the spectroscopic binaries. If we include the 16 spectroscopic companions we found in the literature (for reference see Sec. 12.1) the CSF numbers 1.21. If we however assume

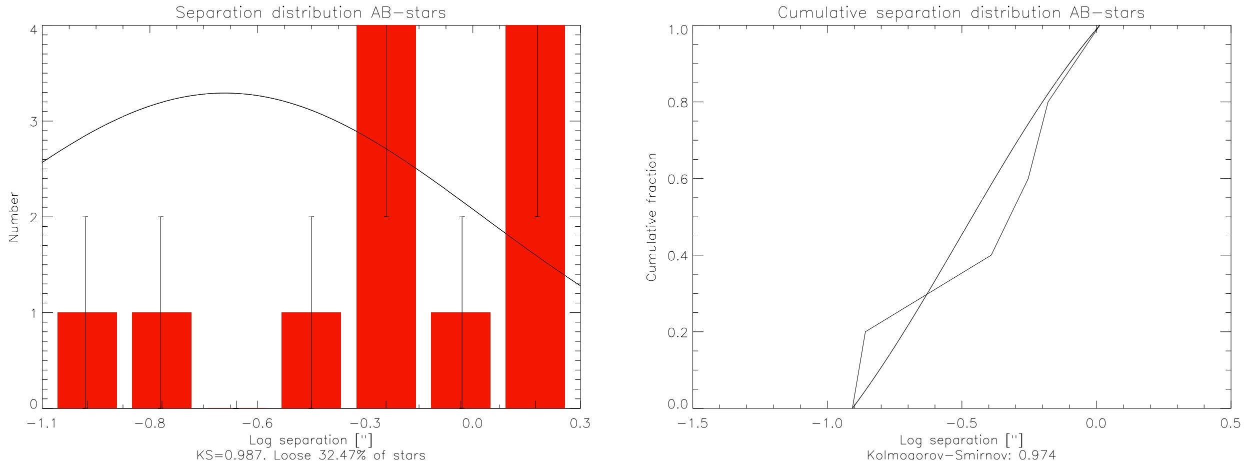

Figure 12.24: *Distribution of separations for the AB-star sample. Left: histogram of the separations. Over plotted is the best fit to the cumulative distribution. Right: Cumulative distribution for systems with brightness differences less than 3 mag. The best fit model is over plotted.*

that the close companions are massive have brightness differences of ≤ 1.75 mag then the CSF is reduced to 1.0. Still in Scorpius Kouwenhoven et al. (2007) detect at least one B2 star with a companion closer than our detection limit for that we could derive a brightness contrast of 2.8 mag in z'. Therefore, the CSF derived under the assumption that the close companions have a brightness contrast ≤ 1.7 mag is probably too low.

For the AB-stars we loose 7 companions due to the bias another 2.6 due to the detection limit at 7 mag and 8.2 at the inner and outer border. This yields a corrected CSF of 0.41 ± 0.06. However again Kouwenhoven et al. (2007) find a large overabundance of close binaries compared to the Gaussian distribution we assume. Therefore, the CSF we derive here is probably strongly underestimating the true CSF.

This finding by Kouwenhoven et al. (2007) also questions the applicability of the lower limit we set using the correlation between separation and brightness contrast. Therefore, we will take the value of 0.41 ± 0.06 as closer to the truth than the lower value we would get using the correlation.

The affect the completion has on the other binary parameters will be described in the following. The MF of the samples will be changed toward a steeper slope i.e. closer to the Salpeter IMF. However for the AB-sample the number of missing companions is low and will only increase the agreement between the MF and the Salpeter IMF. For the massive sample we already stated in Sec. 12.3.2 that 300 low-mass stars are necessary to make the distribution consistent with the Salpeter IMF. So the slope of the MF will be changed by the missing low-mass companions but still be very top-heavy.

We will now investigate how the potential close low-mass companions change the 4 correlations we derived between the binary parameters.

The sample of targets with masses $\leq 2.5\ M_{\odot}$ will hardly be affected because it is almost identical with the sample of wide companions. The entire sample will be changed as follows:

1. The correlation between system mass and separation:
   we have seen from the split of the sample into A-type and B-type stars that the more

massive primaries have the closer companions. But we have also seen in Fig. 12.10 that the mass ratio is much lower for the more massive stars. If we combine these two facts we see that at close separations the system mass is mostly given by the primary mass. So systems with lower mass companions will not strongly change the correlation.

2. The correlation between mass ratio and separation:
   this correlation is rather weak and lives mainly from the fact that there are no close companions with low mass ratios. Thus, the addition of targets with low mass ratios at close separations can reduce if not annihilate or even reverse the correlation.

3. The correlation between mass ratio and system mass:
   we do not find a correlation here. The completion will add systems with larger masses and low mass ratios This will entail a trend to an anti-correlation between mass ratio and system mass.

4. The correlation between primary and secondary mass:
   here the completion will add systems with large primary masses and low secondary masses. Thus, the correlation between primary mass and secondary mass will be reduced.

For th OB-sample the correction reads as follows:

1. The correlation between system mass and separation:
   This correlation is based on the under-abundance of systems with low masses and close separations, as well as on the under-abundance of systems with high masses and large separations. The first under-abundance will be changed if we add close low-mass companions. However the second one will remain. This means the correlation becomes weaker some of it will remain.

2. The correlation between mass ratio and separation:
   The addition of targets with low mass ratios at close separations will reduce the correlation. But the low number of wide companions with large mass ratios will keep some correlation.

3. The correlation between mass ratio and system mass:
   The additional low-mass companions will decrease the trend of the correlation between mass ratio and system mass. Still the low number of systems with low masses and high mass ratios will keep some of it.

4. The correlation between primary and secondary mass:
   The correlation between primary mass and secondary mass will be reduced. Again the low number of targets with low primary mass and high secondary mass will hinder a complete annihilation.

For the distribution of mass ratios the effect of the bias can be estimated as follows: we are biased toward higher mass ratios at least for about 50% of the sample area. For the AB-sample this however will not dramatically change the distribution because the stars we miss due to the varying dynamic range would add one companion with mass ratio of about 0.3 and 3 with a mass ratio below that. The very faint companions we miss are few and the completion toward larger and closer separation copies the brightness distribution i.e. equally adds members to every bin. Therefore, a flat distribution is a very good model for the mass ratio distribution of the AB-sample.

For the OB-sample the completion scheme would add about 2 companions with mass ratios between 0.4 and 0.65, 3 stars with mass ratios between 0.2 and 0.4, and 7 with mass ratios below 0.2. An estimate of the center of gravity from these values is around 0.4. Again the number of very faint stars is low and the completion for spatial losses just copies the distribution already derived. The wide one is only marginally affected by the observational bias that would only increase the overabundance of low mass ratios.

Thus, we can conclude that the distributions of wide companions of the OB-sample truly differs from that of AB-stars and the distribution of the entire OB-sample.

12.5 Summary of the Binary Parameters

To get an overview of the findings we conclude this chapter with a summary of the results.

From our sample of target stars we constructed two sub-samples divided by a mass border of $\approx 10\ M_\odot$ that corresponds to spectral type B2V. For these two samples we derived several multiplicity parameters and compared them:

1. The CSF of the two sub-samples is significantly different (0.39±0.09 and 0.17±0.06 respectively). After completion of the sample we estimate the CSF to be 1.2 and 0.41 for the OB-sample and AB-sample respectively.

2. The degree of multiplicity differs significantly between the OB-sample (1.4±0.1) and the AB-sample (1±0.1)

3. The correlation between separation and system mass is strong for the AB-stars with a slope of ≈ -1. For the OB-sample the correlation is also negative.

4. All samples exhibit a strong anti-correlation between separation and mass ratio.

5. For both samples there exists a strong correlation between system mass and mass ratio

6. For all samples there is a correlation between primary and secondary mass

7. The mass function of the companions for the AB-sample agrees with a Salpeter IMF whereas for the total sample of OB-star companions the exponent Γ is -0.15 rather than -1.35.

8. The distribution of mass ratios is remarkably similar for both samples. It can be fitted by a Gaussian with its peak at 0.45 and a width of 0.3, but also by a flat distribution. For the wide companions only the OB-sample tends toward lower mass ratios, the AB-sample not

9. The distribution of brightness differences is remarkably similar for both samples
10. For the AB-stars there is a correlation between separation and brightness difference, for the OB-stars not.
11. The distribution of separations for the AB-stars is a single log-normal distribution peaked at log(r)=0.07 whereas the distribution of the OB-sample is combined from a close one with maximum closer than log(r)=-0.9 and a maximum at log(r)=0.2.
12. the OB-stars exhibit at least 3 regimes where massive companions reside: spectroscopic companions, a separation of $\leq$ 80 AU and a separation of $\approx$ 1600 AU (and potentially there is a fourth region around 400 AU)
13. About 50% of the companions of the OB-sample 1.7 mag or less fainter than the primary belong to real or suspected triple systems. For the sub-sample with separations $\leq 0\overset{''}{.}2$ this value reaches 75%
14. The observational bias is potentially responsible for the correlations within the AB-sample. For the OB-sample it cannot fully explain the findings

Chapter 13

Discussion

In the last chapter we derived several binary parameters of the samples of OB-stars and AB-stars. In the following these parameters will be used to discuss the different formation channels of multiple systems and decide the origin of the companions. To put the discussion into a more general context in Sec. 13.3 we compare our results to findings in different star forming regions found in the literature.

So in a first step we will now discuss the predictions of binary parameters of the different formation channels. These predictions will afterward be compared to the measurements.

1. Capture scenario:

simulations of a pure capture scenario could produce a CSF of around 30% for Orion-like parameters (Moeckle & Bally 2007). This fraction will rise with increased stellar densities at the time of formation. Unfortunately we do only know proper motions of our target stars (Röser & Bastian 1988) and not the 3 dimensional velocities. Their finding implies that at least 40% of the stars with spectral type earlier than B5 could have had encounters with other stars at minimum separations of the order of $\leq 10^4$ AU. This implies maximum stellar densities of $\approx 5 \times 10^4 pc^{-3}$ that is higher than in the trapezium ($2 \times 10^4 pc^{-3}$ Hillenbrand & Hartmann 1998). So if we for the moment assume our value to be real we will get a higher CSF than derived in Moeckle & Bally (2007). Still we should keep in mind that the value we derived is an upper limit.

Due to the fact that during the many body interactions leading to a capture the two most massive stars involved will form the final system the MF of the companion stars is expected to be top-heavy. Still one would expect a distribution of secondary masses being rather randomly drawn from the IMF and without much correlation to the mass of the primary. The distribution of separations should also be rather random without any correlation to the involved primary and secondary masses. So we will not expect any correlation including separations. But there will be an anti-correlation between system mass and mass ratio. The reason is that the mass of the secondaries is rather randomly distributed the mass ratio will depend solely on the mass of the primary. So with increasing primary mass the mass ratio should shrink. This entails a potential difference between the distribution of mass ratios between stars with high and low masses. Also there will be a tendency toward low mass ratios because in the mass range we observe the number of stars strongly increases with decreasing mass.

We also might find a slight correlation between primary mass and secondary mass because usually the most massive stars of a many body interaction will form the resulting system.

2. Disc fragmentation:

first of all the companions (if they do not undergo evolution) produced by this mechanism should have very low masses (Kratter & Matzner 2006). Secondly the radii of discs around intermediate-mass stars and, thus, the maximum separation of the companion are expected to measure $\leq$ 200 AU ($0\farcs25$) (Kratter & Matzner 2006). An increase of the CSF with spectral type is expected because more massive discs are more likely subject to fragmentation. The upper cut-off of the MF however should be at a fraction of the primary mass M_{prim} (i.e. $\approx$ 0.1 M_{prim}). We would expect correlations between primary mass and secondary mass, as well as between system mass and mass ratio because more massive stars harbor more massive discs. But the more massive companions should sit at larger radii that means we have a correlation between system mass and separation, as well as a correlation between mass ratio and separation. The distribution of mass ratios should have a maximum around 0.1 M_{prim}.

Still if we assume larger radii for the disks and allow for some evolution of the binary due to accretion (see Krumholz 2006) then the parameters will change as we will discuss in more detail during the investigation of the (local) coalescence-scenario.

3. Fragmentation of the pre-stellar core:

for the fragmentation scenario we assume that each star is formed by its own fragment and has no access to any circumbinary matter (as in Krumholz 2006).

The rate of binaries and multiple systems is large within this scenario (see for example Clarke 2001). Additionally the models predict an increase of the CSF with primary mass. The fact that the two most massive fragments will form the out-coming binary will make the MF of the companion stars top-heavy. The correlation between system mass and binary separation is possible within this scenario when the density distribution of the core depends on the core mass M_{core}. If the average density $\bar{\rho}$ of the core rises with core mass the separation of the companions can decrease with system mass for this scenario. If $\bar{\rho} \propto M_{core}^4$ we get the observed $M \propto R^{-1}$ connection between system mass M and separation R. However, this strong increase of density with core mass is very unlikely and measurements by Kirk et al. (2005) and Bacmann et al. (2000) contradict this scenario. They find a density rather independent of the core mass or even potentially increasing with decreasing core mass.

Another possibility to explain a correlation is that during the collapse phase the density gradient at that fragmentation occurs depends on the core mass. This could also bring more mass into smaller regions. As example imagine two cores with radius R, one with a density $\rho \propto r^{-2}$ the other with a density $\rho \propto r^{-2.5}$. When we calculate the radius $R_{1/2}$ in that 50% of the mass of the core lies we get $R_{1/2} \approx 0.5$ for the first core and $R_{1/2} \approx 0.25$ for the second core. So a small change in the exponent entails a large change in the half mass radius. This dependence becomes even stronger for exponents with values between -2.5 and $>$ -3. An increase in the density gradient within the core is expected if it collapses inside out as proposed for example in Krumholz (2006). The question is why should there be a dependence between core mass and density gradient at the point of fragmentation? A possible explanation is that if the pressure P inside the core is correlated to the core mass then the Jeans mass M_J is larger and the density can be potentially higher before the core fragments. This correlation between core mass and pressure for cores at the same temperature means that the more massive the core the higher the turbulence. Such a correlation has been observed (Larson 1981; Caselli & Myers 1995). So the Jeans mass within a core is correlated to the core mass.

If the core now starts to collapse by an inside-out collapse the Jeans mass shrinks, as well as the Jeans radius. If we assume a combination of Jeans radius $R_J \propto P/\bar{\rho}$ and Jeans mass $M_J \propto P^{3/2}/\bar{\rho}^2$ to be the criterion for core fragmentation (this includes that one of the two is responsible alone) then the average density $\bar{\rho}$ of the fragment will increase with core mass. For similar core densities in the beginning this entails an increased density gradient for the more massive cores with respect to the less massive ones. If we assume for example the Jeans mass to be the criterion for the fragmentation we can calculate the relation between core mass and density gradient as follows:

Under the assumption that the core has one Jeans mass when it starts to collapse the relation between pressure P and core mass reads $M_{core} \propto P^{3/2}$. If we assume a density dependence $\rho(r)$ on the distance r from the center during collapse of $\rho(r) \propto M_{core}^{x/3}/r^x$ (the dependence of the density on the core mass is necessary to fulfill the boundary condition of a continuous behavior toward the interstellar medium) with $0 < x \leq 3$ then the Jeans mass depends on r and M_{core} like $M_J \propto M_{core}\left(m_{frag}/M_{core}\right)^{2x/3}$. Here m_{frag} is the mass of the fragment with radius r. For a fragmentation into a few parts only the ratio m_{frag}/M_{core} is approximately constant and necessarily smaller than 1. The Jeans mass can only be kept constant with increasing core mass if the exponent x increases at the same time. So the density gradient must depend on the mass of the core.

Cores with these steep density gradients i.e. gradients steeper than r^{-2} have been observed by Bacmann et al. (2000). An in depth study with ALMA can potentially provide sufficient data with high angular resolution to test the above relationship.

The anti-correlation between mass ratio and separation can also be explained within a fragmentation scenario. Imagine a sample of pre-stellar cores of the same mass. The radius of the volume out of that the primary is born is correlated to the mass of the primary. Additionally the matter left to form the companion is anti-correlated to the mass of the primary. So with increasing primary mass the secondary is further away and has lower mass.

If we assume a dependence of density gradient on core mass then the dependence of mass ratio on separation should become stronger with system mass.

A weak correlation between system mass and mass ratio also is consistent for a fragmentation scenario in that the core fragments into very few parts only. For such a scenario the mass of the companion is predicted to be correlated to the primary mass (Clarke 2001). Thus the mass ratio should be constant. An increase of the mass ratio with system mass is difficult to explain in this context. For a fragmentation of the core in a larger number of fragments one would rather expect an opposite behavior (see Clarke 2001). However, especially for massive stars there exists a possible explanation. If the most massive of the fragments as soon as it becomes a star starts to heat the core (see Krumholz 2006) then the other fragments must be necessarily more massive because the Jeans mass rises with temperature. The more massive the primary the earlier and stronger the heating and, thus, the more massive the companions. The luminosity L of the star depends on the mass M like $L \propto M^{3.5}$. This relation is measured for main sequence stars still there should be a strong increase of luminosity with mass for young stellar objects as well. Therefore the companion masses should increase more than proportionally with system mass.

For a fragmentation into a few parts only the distribution of mass ratios should be independent of primary mass (Clarke 2001), whereas for a fragmentation into a small cluster the MF should

be universal for all cores (Clarke 2001).
4. (Local) coalescence:
for details on this scenario see e.g. Bate (2000), Bonnell et al. (1998), Bonnell et al. (2005). Here we will merely repeat the outcome.
Under a (local) coalescence scenario we understand a scenario where the stars compete for the matter of the available reservoir. In the case of global coalescence this reservoir is the entire cluster. In the case of local coalescence it is the pre-stellar core that fragments. These scenarios need stellar densities of $\approx 10^6 pc^{-3}$ to work (Zinnecker & Yorke 2007). As mentioned above we expect the original stellar density of the associations to be below $10^5 pc^{-3}$. So a local scenario is more likely to work.
Regarding the predictions both cases have in common that the binary or multiple systems form as originally wide low-mass systems and undergo evolution during the accretion phase. This evolution strongly affects the binary parameters as we have seen in the beginning of chapter 12. The findings there can be summarized as follows:
within a scenario of accretion onto a wide binary anti-correlations between separation and system mass, and between separation and mass ratio are expected.
We further expect a correlation between system mass and mass ratio, as well as between primary and secondary mass. An increase of CSF with primary mass, as well as a top-heavy MF for massive stars is also expected.
So if our assumptions are right we cannot distinguish between the fragmentation of the pre-stellar core and the coalescence scenario. However, we will favor the channel that needs the least additional assumptions to explain the data.
After this presentation of the expectations of the various models we will compare them to the AB- and OB-samples separately.

13.1 The Sample of AB-stars

As starting point of the discussion we recapitulate the major findings for this sample. Remember that the observational bias can be responsible for some of the strength of the findings. However, the influence of this bias is known only qualitatively so we will assume strong correlations between parameters to 'survive' a correction for the bias.

1. The CSF of the completed sample numbers 0.41±0.06 but is likely to be higher

2. The systems are purely binaries

3. The mass function of the companions agrees well with a MF with exponent Γ= -1.05. But it is also consistent with the Salpeter IMF. The Salpeter IMF again agrees well with the MF of the field stars in our sample

4. There is a strong anti-correlation between system mass and separation

5. There is a potential anti-correlation between mass ratio and separation

6. There is no correlation between system mass and mass ratio for the entire sample. For the low-mass targets however the correlation is strong

7. Primary and secondary mass are correlated strongly

8. The distribution of mass ratios is compatible with a Gaussian distribution peaking around 0.45 or a flat distribution with the lowest value around 0.15

We will briefly discuss the findings in the context of the different formation channels and summarize the results in a table at the end of this section.
First of all we have to note that the low number of companions does not allow for definite conclusions but rather has to be taken as strong hint in favor or against a particular formation scenario.
The CSF agrees well with all scenarios (probably besides the disc fragmentation). For the capture scenario to work we need a stellar density at the time of formation slightly above that of Orion that is potentially in agreement with the data. A slightly flattened MF of the companions again agrees well with the capture, fragmentation, and coalescence scenarios. For all three models we can state that this agreement between MF and (flattened) Salpeter mass function is peculiar in the context of stellar evolution from pre-stellar cores to stars. Observations of pre-stellar cores (Alves et al. 2007, Beuther & Schilke 2004) seem to suggest that already at this evolutionary stage the mass function follows a Salpeter law with a shift in mass (Alves et al. 2007). However, these results have to be taken with care because the error bars on the data of Beuther & Schilke (2004) are large and in the case of Alves et al.(2007) it is questionable if the cores will give birth to stars.
If we for the moment assume the findings are real and we also take into account that the mass ratio does not strongly depend on system mass then the MF of the cores will be transcribed (with a tendency toward higher secondary masses as argued above) onto the MF of the primaries, as well as the secondaries what is consistent with our data.
If we take the increase of mass ratio with increasing system mass for real the resulting MF for the primaries should be steeper than that for the secondaries. This is easy to see from the ratio of primary mass over core mass. Imagine two cores, one with a mass of 11 $M_{\odot}$ and the other with a mass of 55 $M_{\odot}$. The mass ratio between the primaries born out of these cores is lower than the mass ratio of the cores themselves. Lets assume the masses of the primaries are $1M_{\odot}$ and $4M_{\odot}$, and the star formation efficiency is 10%. Then the secondaries have masses of $0.1M_{\odot}$ and $1.5M_{\odot}$ respectively. The MF of the primaries has the same decrease in number over a factor of 4 in mass as the MF of the secondaries over a factor of 15 in mass. Thus the MF of the secondaries must be flatter than that of the primaries. So we would expect a deviation from the Salpeter IMF. This might actually be seen in the reduced slope of our MF of the secondaries. However, as usually the small numbers make definite conclusions impossible. For three of the four models we can state that the flat slope of the MF of the secondaries in concert with an increase of mass ratio with system mass is consistent with a picture where the primary MF is the Salpeter IMF whereas the secondaries follow a different MF.
The disc-fragmentation is again excluded due to its prediction of low companion masses.

The correlations we find between the binary parameters all disagree with a pure capture scenario. For the scenario of disc fragmentation all correlations agree besides the anti-correlation between system mass and separation, and the (potential) anti-correlation between mass ratio and separation. Under the assumptions made above all the correlations fit well to both the fragmentation scenario, as well as the coalescence scenario. One particular case is the correlation between system mass and mass ratio. If we use the entire sample then the slope of the correlation between system mass and mass ratio is not consistent with the accretion onto a wide binary on first sight. However, if we assume that the sound speed is not insignificant in Eq. 12.4 then ratio between the increase in mass for the secondary and the primary can be lower and, thus, the correlation, as well as the slope can be weaker. However, if we only have a look onto the targets with primary masses $\leq 4.5\ M_{\odot}$ the slope is large that fits into the model.
The distribution of mass ratios does not fit to the capture scenario, as well as for the disc fragmentation because for both we would expect a tendency toward low mass ratios. The two other scenarios both are consistent with the findings.
The results are summarized in table 13.1. Column 1 states the theoretical formation channel of the binary, the other columns state the consistancy between the model and the data ('y': yes, 'n': no, 'pn': probably no) for the binary parameters: CSF, MF, the correlations between system mass and separation, between mass ratio and separation, between system mass and mass ratio, and between primary mass and secondary mass, and the mass ratio distribution.

Table 13.1: *Consistency between data and channel of binary formation AB-sample*

Formation channel	CSF	MF	Sys. mass Sep.	Mass rat. Sep.	Sys. mass Mass rat.	Prim. mass Sec. mass	Mass ratio distr.
Capture[16]	y	y	n	n	n	n	n
Disc-frag.[17]	pn	n	n	n	y	y	n
Frag. of pre-st. core[18]	y	y	y	y	y	y[19]	y
(local) coal.[20]	y	y	y	y	y	y	y

16: remember that the original stellar density is uncertain and might be too low to produce a sufficiently large CSF, 17: without further evolution of the fragment. Remember that the size of the disc is of the order of a few 100 AU. Further evolution will result in the predictions of the coalescence scenario but the predicted separations will become even smaller 18: under the assumptions of a correlation between the strength of the turbulence and the core mass, as well as a correlation between density gradient and core mass, 19: for a fragmentation into a few parts only, 20: preferably local coalescence because the global stellar density is unlikely to have reached values high enough for the coalescence to work on a global scale

So the conclusion is that the binaries form either by fragmentation of the pre-stellar core or by a local coalescence scenario. We will favor the second mechanism because for the fragmentation process the correlation between core mass and density distribution at the point of fragmentation to match the predictions is a weak point in the scenario. Additionally the potential correlation between system mass and mass ratio in the case of the intermediate-mass stars makes this scenario questionable.

13.2 The Sample of High-mass Stars

For the OB-star sample some of the parameters are different what we could expect from the already different multiplicity. The corner stones for the model read as follows:

1. The CSF of the completed sample numbers 1.21±0.16 but is likely to be higher
2. About 50% of the systems include more than one companion star
3. The MF for the companions of the massive sample can be fitted by a MF with an exponent of $\Gamma \approx$-0.15 in stead of Γ=-1.35
4. There is a potential anti-correlation between system mass and binary separation
5. There is an anti-correlation between mass ratio and separation
6. There is a correlation between mass ratio and system mass
7. There is a probable correlation between primary and secondary mass
8. The mass ratio distribution for the wide and close companions are Gaussian. The distribution for the wide companions favors low mass ratios whereas the distribution for the close companions is peaks around 0.5, falling down to $\ll$ 0.1 at the ratios of 1 and 0.1. The minimum ratio measured for the close sample is 0.3

We have seen that the correlations between the various parameters are strongly contaminated by spectroscopic and potential undetected companions. So the parameters derived have large errors. However, usually at least a general trend of the behavior of the parameters is visible.

Again we can exclude a pure capture and a disc fragmentation scenario with the same arguments as for the AB-sample. Most of the argumentation is similar to that for the AB-sample. So here we will discuss solely the differences to this sample.

Note however that during this argumentation we used the dependence of the Bondi-Hoyle accretion rate on the velocity of the star. But Bondi-Hoyle accretion does not work for massive stars due to the strong radiation pressure. Still the formation of massive stars by accretion is theoretically still possible. So if we assume the influence of the motion through the gas for the accretion scenario onto the massive star to be the same as for Bondi-Hoyle accretion we still can use the argument.

The fact that the CSF is higher than for the AB-sample is expected in all scenarios.

The same is true for the finding that the MF is more top-heavy than for the AB-sample.

Regarding the correlations between the binary parameters we can argue as we did for the AB-sample. The correlation between mass ratio and system mass is given for all samples. The lowest value (0.3) is consistent with the finding for the entire AB-sample whereas the smaller value from the reduced sample (1.7) is consistent with that for the low-mass stars only. For a fragmentation scenario this correlation is neither given for a N=2 fragmentation nor for a fragmentation into more parts (see Clarke 2001). If we take into account that more massive stars usually have a higher number of companions that we partly do not detect then we are underestimating the system mass especially for the most massive stars. As well the mass ratio will be reduced if we use the combined mass of the primary and the (undetected) companion as true primary mass. Both changes will result in a decrease in the correlation. So in the end the true correlation might be much lower than the one we measure.

For both models, fragmentation, and accretion onto a wide binary, we can state that the flat slope of the MF of the secondaries in concert with an increase of mass ratio with system mass is consistent with a picture where the primary MF is the Salpeter IMF whereas the secondaries follow a different MF. As a crude approximation we take the relationship between system mass M_{sys} and the ratio between primary mass M_1 and secondary mass M_2 as linear (for large masses this is of course wrong because at some mass the secondary would be more massive than the primary). This roughly complies with the value of the slope averaged over the four samples. If we then use the formulas $M_1 + M_2 = M_{sys}$ and $M_2/M_1 = aM_{sys}$ then $M2 = aM_{sys}^2/(1 + aM_{sys})$ and $M_1 = M_{sys}/(1 + aM_{sys})$. For a small value of aM_{sys} the secondary mass M_2 goes quadratically with system mass and M_1 linearly. If the system MF follows the Salpeter IMF then so does the primary MF. The secondary MF follows the distribution of $\approx \sqrt{M_{sys}}$ and has, thus, an exponent of α=-2.35/2 and, thus, for the cumulative distribution of $\approx \Gamma = -0.2$. This value is consistent with our measurement.

For the massive stars again the dependence of the density on core mass and the dependence of the mass ratio on system mass are weak points of the fragmentation scenario whereas the accretion scenario can easily be applied to the data and, thus, is more favorable to explain the formation of the stars. The high multiplicity of the massive targets also fits into this picture. Still we have to note that the entire argumentation, especially for the fragmentation of the pre-stellar core, is spoiled by the dynamical interactions within the systems with more than one

Table 13.2: *Consistency between data and channel of binary formation OB-sample*

Formation channel	CSF	MF	Sys. mass Sep.	Mass rat. Sep.	Sys. mass Mass rat.	Prim. mass Sec. mass	Mass ratio distribution
Capture[21]	n	n	n	n	n	n	n
Disc-frag.[22]	pn	n	n	n	n	n	n
Frag. of pre-st. core[23]	y	y	y	y	y	y[24]	y
(local) coal.[25]	py	y	y	y	y	y	y

21: the masses of the companions are much too large to be explained by pure capture, 22: without further evolution of the fragment. Remember that the size of the disc is of the order of a few 100 AU. Further evolution will result in the predictions of the coalescence scenario but the predicted separations will become even smaller 23: under the assumptions of a correlation between the strength of the turbulence and the core mass, as well as a correlation between density gradient and core mass, 24: for a fragmentation into a few parts only, 25: preferably local coalescence because the global stellar density is unlikely to have reached values high enough for the coalescence to work on a global scale

companion, that number potentially more than 50%. For the case of the coalescence scenario the rather qualitative argumentation we used is supported by simulations by Bonnell et al. (2005). The results are summed up in Table 13.2. Column 1 states the theoretical formation channel of the binary, the other columns state the consistancy between the model and the data ('y': yes, 'n': no, 'pn': probably no) for the binary parameters: CSF, MF, the correlations between system mass and separation, between mass ratio and separation, between system mass and mass ratio, and between primary mass and secondary mass, and the mass ratio distribution. To end the discussion we will turn our attention to a very peculiar system: HD216711. It has two companions, one at $0\farcs76$ and one at $1''$ with a combined mass larger than 0.3 times the primary mass *but* the primary is a spectroscopic binary i.e. more massive than would be deduced from its spectral type. This means for example the disc fragmentation scenario could still be applied. Also a scenario is possible where one star is moved to a wider orbit by dynamical interactions and the other is born out of the disc. Still the majority of the
targets cannot be modeled this way.

Again we will summarize the findings in a table. The entries have the same meaning as for the AB-sample.

So again we will favor a scenario of local coalescence to explain the data.

13.3 Comparison to Other Star Forming Regions

Various studies of the multiplicity of main sequence and TTauri stars are now available. This includes studies on F-type and B-type stars (Abt et al. 1990, Abt&Levy 1976), nearby G-dwarfs (Duquennoy & Mayor 1991), K-dwarfs (Mayor et al. 1992), M-dwarfs (Henry & McCarthy 1990, Tokovinin 1992, Fischer & Marcy 1992), TTauri stars (Leinert et al. 1993, Brandner et al. 1998, Ratzka et al. 2005, Ghez et al. 1997) and OB-samples (Duchene et al. 2001, Preibisch et al. 1998, Nelan et al. 2004). One can find a decrease in CSF with spectral type from $\geq$ 100% for OB-type stars to 50%-60% for F- and B-type stars to 45% for K-type stars and 42% for M-type stars. For the TTauri stars the CSF varies between different star forming regions. For Taurus itself there is high evidence for a CSF of 100% whereas in Scorpius and ρ- Ophiuchus the CSF seems not to differ significantly from that of main sequence low-mass stars.

Our findings confirm the trend of a decrease in the CSF toward stars of later spectral type.

To be more concrete in Table 13.3 we compare our CSF with that from the star forming regions found in the literature in the common regime of spatial separations. The name of the region and the targets under investigation are shown in column 1 and 2 respectively. For comparison we artificially place the region from the literature at the distance of Cep OB2/3 and apply our observational constraints to it. This yields the range of separations presented in column 3 of the table. The CSF from the literature shown in column 4 is then the CSF derived for this range of separations. As comparison we show the CSF of our OB-sample and AB-sample derived for the same range of separations in column 5 and 6 respectively.

The CSFs found from the literature in most regions agree. The two exceptions are Orion and Taurus. Both have an overly high CSF where Orion has by far the highest one.

For the AB-sample these two regions are also the only ones for that the CSF does not agree with

Table 13.3: *CSF for different star forming regions*

Region name	Type	separations [AU]	CSF	CSF-O	CSF-AB
solar neighborhood	G-type dwarfs	64-1600	0.15±0.03	0.40±0.08	0.16±0.06
Taurus	TTauri	64-1820	0.28±0.06	0.42±0.08	0.17 ±0.06
NGC6611	O/B-stars	200-3000	0.20±0.06	0.34±0.07	0.21±0.06
Chameleon	TTauri	120-500	0.13±0.03	0.12±0.05	0.07±0.04
Orion trapezium	OB-stars	64-500	0.38±0.14	0.24±0.06	0.10±0.05
ρ-Ophiuchus	TTauri	56-928	0.16±0.04	0.30±0.07	0.11±0.06
Upper Sco A	TTauri	64-450	0.15±0.05	0.22±0.06	0.13±0.07
Upper Sco B	TTauri	64-450	0.22±0.08	0.22±0.06	0.13±0.07
Lupus	TTauri	64-450	0.15±0.05	0.22±0.06	0.13±0.07

the CSF from the literature.

Besides this potential difference and consequences thereof the sample of AB-stars compares well with most findings in other star forming regions in the literature. Thus in the following the subject of the discussion will be exclusively the OB-star sample.

In the case of this sample the CSF agrees only with regions where the range of separations is relatively small. For samples with a larger regime of separations the CSF we find in Cepheus is usually larger than that found in the literature. The only exception is Orion where the CSF from the literature is comparable to the one we detect.

The fact that the CSF compares well to the regions where the spatial regime is small and not to those with a larger range of separations indicates that the spatial distribution of companions is important for a comparison.

The degree of multiplicity within this regions can be derived from the ratio of single stars (S) to binaries (B), triple systems (T) and quadruple or higher systems (Q). This ratio found in the literature for low-mass and TTauri stars is 57:38:4:1 and 60:39:3:2 respectively. If we apply our detection bias to the sample by Preibisch et al. in Orion we find a distribution for S:B:T:Q of 6:3:3:1.

For the regions mentioned above the degree of multiplicity is 1.14 ±0.06 for the G-star sample of Duquennoy and Mayor, 1.16±0.06 for the TTauri stars and 1.7 ± 0.26 for Orion. The value found in Orion differs significantly from those in the other regions. For our sample of massive stars we find a degree of multiplicity of 1.4 ±0.1 or if we include the potential companions also of 1.5±0.1. **Both values are consistent with Orion only**.

Preibisch et al. (1999) also find a significant difference of the CSF and the degree of multiplicity for stars earlier and later than a spectral type around B3. In our case we observe something similar with a cut around spectral type B2. The CSF is much higher for the earlier stars and the number of higher order systems significantly larger.

The distribution of separations can be compared to that found by Duquennoy & Mayor (1991) after a conversion from periods to AU. This has been adapted from the paper by Leinert et al. 1993. They find a log-normal distribution with a maximum at 31 AU ($0\farcs04$) and a width of $\sigma[log(P)]$ =2.3. Our distributions of the OB-star sample has also a tendency toward close separations but with a maximum at $\approx$ 80 AU. It also seems to have a second peak around 1267 AU.

A similar increase of the distribution toward close separations has been observed by Kouwenhoven et al. (2007). They observed a distribution of separations for members of the Sco OB2 association that rises toward the inner border of their separations. The peak lies between 0 and 280 AU. The distribution then decreases toward 1960 AU.

Brandner & Köhler (1998) find a distribution that steeply rises toward their detection limit of 70 AU falling down to 238 AU similar to our OB-star distribution. There also seems to be an additional small peak at 350 AU. They correlate these two peaks to two different distributions, the closer one effected by the presence of massive stars, the wider one not. This explanation cannot be applied to our sample. Also a discrimination between O-star primaries and B-star primaries in our sample to mimic their argument does not support their hypothesis. Still their distribution of separations is the only distribution with a form similar to the distribution of our OB-star sample. The CSF they derive (0.22) is comparable to that in Taurus in the same regime of separations. Therefore if we follow the discussion for the Taurus sample we again will end up with a similarly high CSF for the complete sample.

Our brightness distributions of OB- and AB-stars are remarkably similar. They are also conform with that found by Kouwenhoven et al. (2007). Their distribution, if binned in 0.5 mag bins, is also rather flat. This finding is confirmed by Ratzka et al. (2005) in ρ-Ophiochus. They also detect an overabundance of large brightness contrasts between primary and secondary for wide pairs. This tendency to low mass ratios for wide pairs is also consistent with the data from NGC6611. As well we see this effect for our OB-sample.

The samples in Orion and in the solar neighborhood also have a tendency toward low mass ratios. These samples however include a large number of close binaries and are, therefore, not compatible with our findings.

In contrast to these findings stands the observation by Brandner et al. (1996). Their distribution of brightness differences derived from several low-mass star forming regions has a large overabundance of equally bright pairs.

The MF of the companion stars changes between our two samples with values of Γ= -1.35 for the AB-sample and Γ= -0.15 for the OB-sample. A similar flattening has been observed in the center of massive young clusters in our galaxy (Figer et al. 1999, Stolte et al. 2002). There values of Γ between -0.65 and -0.8 are measured. Portegies Zwart et al. (2002) argued that this difference to the Salpeter law can be explained by *dynamical* mass segregation. This mass segregation scenario can be potentially applied in our case because proper motion data by Röser & Bastian (1988) implies that at least 40% of the stars with spectral type earlier than B5 could have had encounters with other stars at minimum separations of the order of $\leq 10^4$ AU. The time of closest apparent separation is either at 4 Myr ago or a few 10^5 years. We do not know the velocity in radial direction of the objects. So the true separations might be significantly larger and the reason for the top-heavy MF could be another one: the Γ values found in these regions fit with our mass function if we assume that the masses of our primary stars are distributed like a Salpeter IMF and the companions have a MF with the slope detected here. The observed value would then result from a mixture of the two slopes yielding a value intermediate between -0.15 and -1.35. We, therefore, favor the model that the high multiplicity and tendency for equal companion mass is intrinsic to massive stars and increases the slope of the IMF especially in

regions harboring numerous massive stars. This includes that the multiplicity of massive stars does not strongly depend on the density of the surrounding cluster/association or initial conditions. Thus the IMF found in the galactic clusters is strongly contaminated by binary stars.
The distribution of mass ratios of AB-stars we find is flat with a slight increase around 0.45. This behavior is compatible with values from the literature (i.e. Duquennoy & Mayor 1991) that show a peak around 0.2-0.3 but in general are rather flat. In other regions like NGC6611 (Duchene et al. 2001) or Scorpius (Kouwenhoven et al. 2007) there is an overabundance of low mass ratios that we cannot confirm.
These distributions however are comparable to that of our OB-sample. There we also have an overabundance of low mass ratios wrt. high mass ratios for the wide companions. Our closer sample is well fitted by a Gaussian with peak at 0.45. Kouwenhoven et al. (2007) also detect a peak of the distribution around this value for their companions closer than 280 AU. However, they still have a larger number of companions with low mass ratios at separations closer than $0''.3$ (42 AU) that are too close to be detected in our survey. So we can summarize the comparison in the following tables (13.4 and 13.3):

Table 13.4: *Comparison between the AB-sample ad other regions*

Region	CSF	Degree of mult.	Sep. dist	Brightness dist
Solar neigh.	py	n	n	n
Taurus	n	n	n	py
NGC6611	y	-	-	pn
Chameleon	y	-	n	n
Orion trapezium	n	n	-	n
ρ-Oph	y	-	n	y
upper Sco A	y	-	n	y
Upper Sco B	y	-	n	y
Lupus	y	-	n	n

Table 13.5: *Comparison between the OB-sample and other regions*

Region	CSF	Degree of mult.	Sep. dist	Brightness dist
Solar neigh.	n	n	py	n
Taurus	y	n	py	py
NGC6611	**py**	**-**	**-**	**py**
Chameleon	n	-	py	y
Orion trapezium	**y**	**y**	**-**	**n**
ρ-Oph	n	-	n	y
upper Sco A	n	-	py	y
Upper Sco B	n	-	py	y
Lupus	n	-	n	y

In these tables we compare our binary parameters with those found in other star forming regions. For this comparison we artificially placed the regions at the distance of Cep OB2/3 and applied our observational biases. The parameters compared are CSF, degree of multiplicity, the distribution of separations and the distribution of brightness differences which is close to the mass ratio distribution. 'y' shows an agreement with our sample, 'n' a definit non-agreement, 'py' a probable agreement, 'pn' a probable non-agreement and '-' means that there is no data available on this parameter.

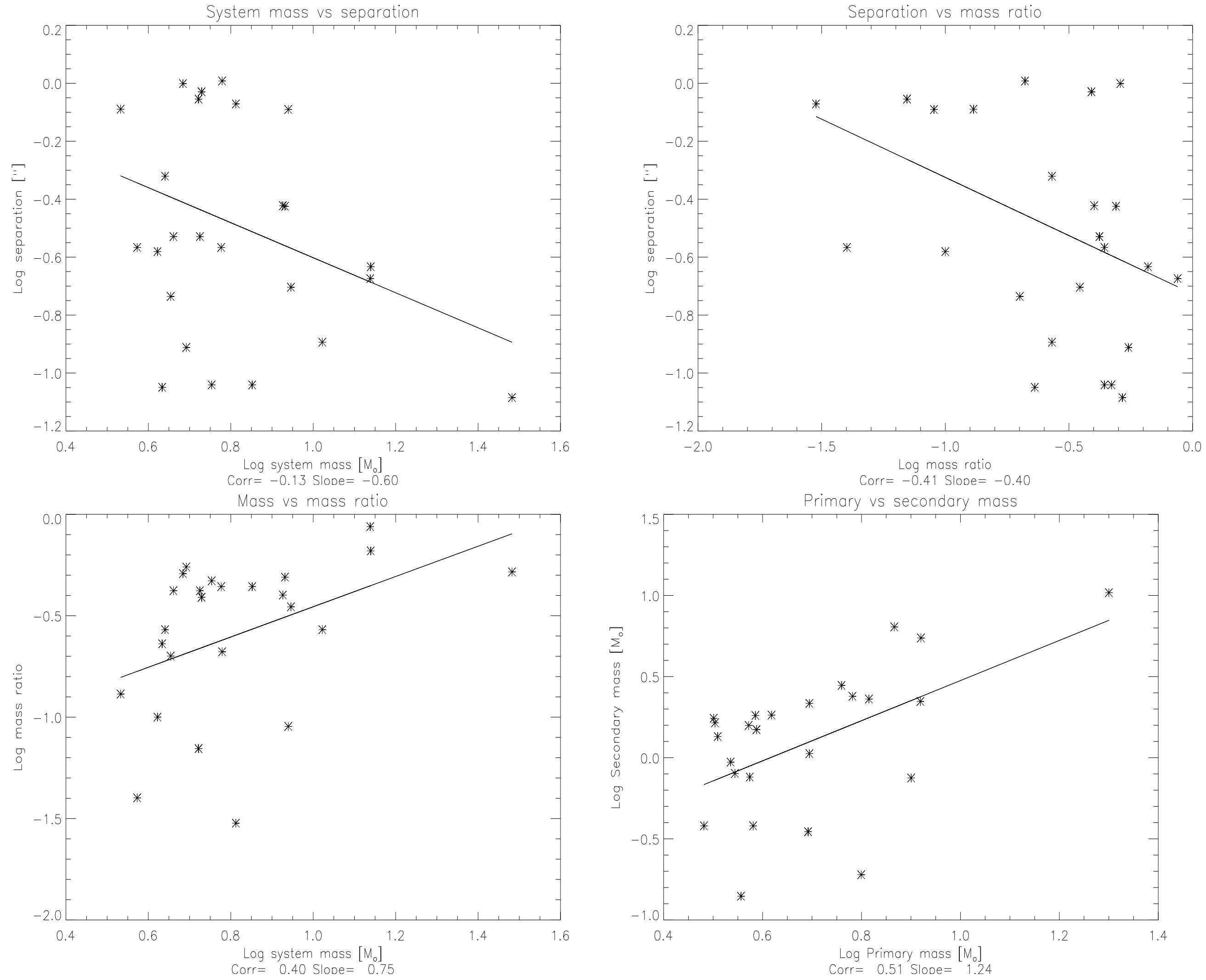

Figure 13.1: *Correlations for the targets with masses > 3 $M_\odot$ of the Sco OB2 sample by Kouwenhoven et al. (2007). Upper left: system mass versus separation, upper right: mass ratio versus separation, lower left: mass ratio versus system mass and lower right: primary mass versus secondary mass.*

So we see that the AB-sample besides the separation distribution agrees well with findings in other low-mass stars forming regions. The main exception is that we do not detect a large number of close companions. This, however, might be largely caused by the biases of our observation especially the absolute detection limit at 0.″8.
The OB-sample can confirm the **multiplicity found in Orion** and the tendency for lower mass ratios for the wide companions as detected in NGC 6611. The existence of a peak of the distribution of separations closer than ≈ 80 AU is also confirmed.

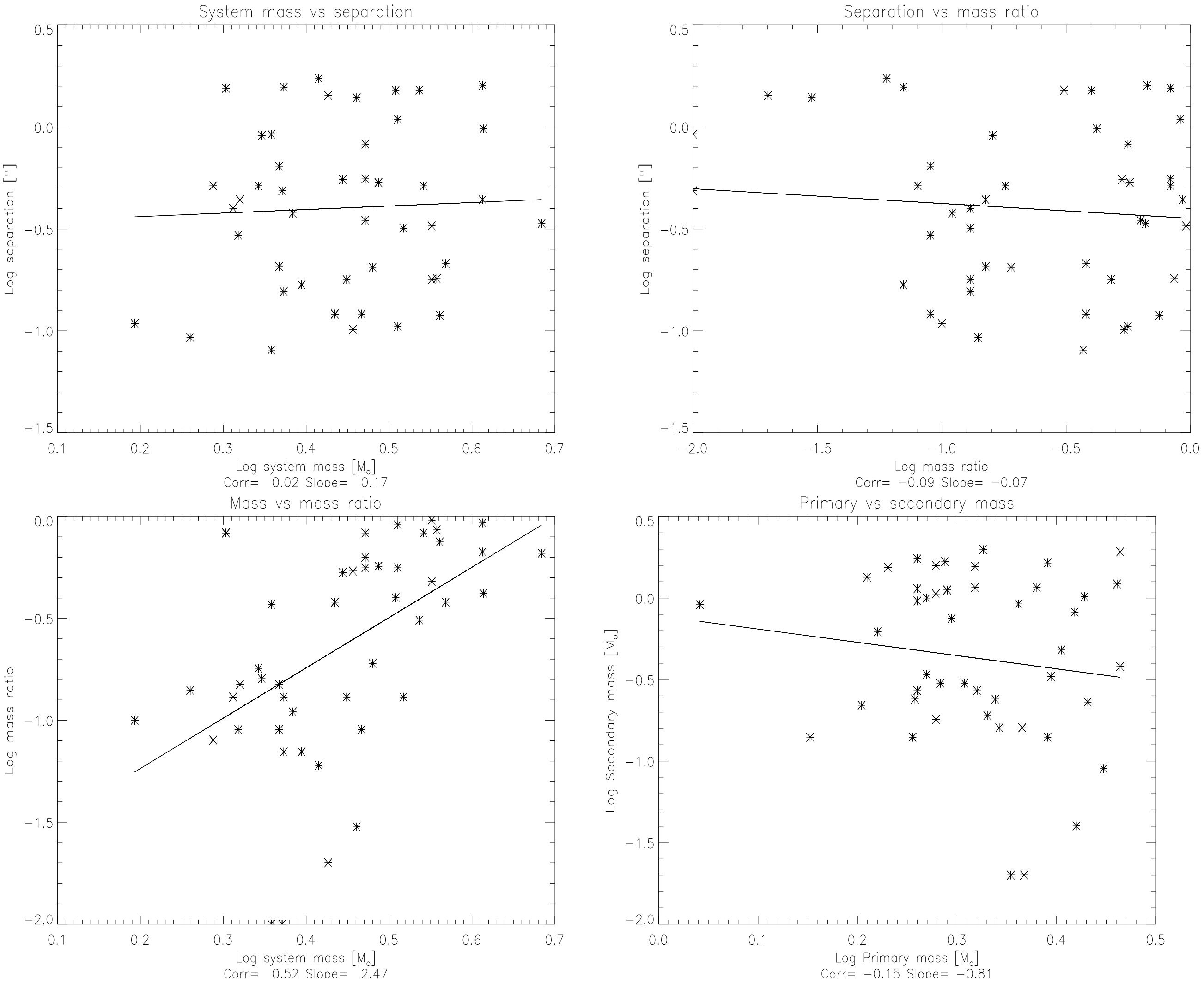

Figure 13.2: *Correlations for the targets with masses $< 3\ M_\odot$ of the Sco OB2 sample by Kouwenhoven et al. (2007). Upper left: system mass versus separation, upper right: mass ratio versus separation, lower left: mass ratio versus system mass and lower right: primary mass versus secondary mass.*

The correlations between the binary parameters can be compared to the data Kouwenhoven et al. (2007). Note that this comparison also allows to estimate the effect of the observational bias because their target is much closer ($\approx$ 140 pc). This means the data for a sample with the physical separations we probe is much less affected by an observational bias.
Unfortunately they do only have one target with a mass above 15 $M_\odot$ and with a companion within our detection limits. Therefore we extend the sample of 'massive' stars down to 3 $M_\odot$ to have a significant number of targets.
We find the same correlations for the sample 'massive' subsample of their data as for ours (see Fig. 13.1). The strength of the correlation gets larger if we artificially apply the observational bias. So does the slope of the correlation. But obviously the correlation is not completely generated by the bias. so we take this as confirmation that our findings are real and not entirely produced by a bias.

For the stars with masses below $3 M_\odot$ the only correlation is between system mass and mass ratio (see Fig. 13.2). This, however, is strong (0.54) with a slope of 2.7.

So for the stars with masses greater than 3 $M_\odot$ (earlier than A0) the formation scenario seems to be rather universal whereas the stars with masses below 3 $M_\odot$ only the correlation between mass and mass ratio is present. Note that if we artificially apply our observational bias the findings do not change significantly. So we conclude:

1. The CSF and the degree of multiplicity of our OB-sample compare well with the findings in Orion
2. The CSF for the AB-stars agrees well to that in other low-mass star forming regions besides Taurus. The dearth of multiple systems with more than one companion does not agree with the findings in any other region
3. The mass limit attached to the change in the CSF and the degree of multiplicity is in the same range as found in Orion and also agrees with the theoretical border between stars with and without PMS-phase
4. The mass function of the companions for the AB-sample agrees with a (potentially slightly flattened) Salpeter IMF whereas for the OB-star companions the exponent is -0.15 rather than -1.35. This value can explain the flattened IMF found in the centers of massive clusters as a combination of a Salpeter IMF for the primaries and a strongly flattened MF for the companions rather than dynamical mass segregation.
5. The rise toward close separations in the distribution of separations in our OB-sample compares well with results found in other star forming regions
6. The flat distribution of separations of the AB-sample is unique. It might, however, be largely caused by the observational bias
7. The distribution of brightness differences for the AB- and OB-star sample compares well to the distributions found in most other star forming regions
8. The tendency of wide companions of the OB-sample to be less massive compares well with the findings in NGC6611 and ρ-Oph
9. The model of binary evolution due to accretion we support with our data is also applicable for the B-stars in the sample by Kouwenhoven et al. (2007) in the Sco OB2 association. For the stars with lower masses only the correlation between system mass and mass ratio remains
10. An artificial application of our observational bias to the data by Kouwenhoven et al. (2007) does not result in an dramatic change of the correlations between the binary parameters. This supports the assumption that our data comes close to the truth

Chapter 14

Summary and Conclusions

We performed a z' band multiplicity-survey of massive and intermediate-mass stars in the Cep OB2/3 association. Physical companions were determined by a probability argument.

We divided our sample of 126 target members of the association into two subsamples of stars. One subsample includes all primaries with spectral types earlier than B2 the other those stars with later spectral type. This border fits well with the theoretical border between the stars with and without PMS-phase. This mass border also divides regimes of a different CSF, as well as degree of multiplicity and compares well to the border detected by Preibisch et al. (1999) in Orion.

The CSF of the sample of intermediate-mass stars was measured to number 17±6%. A completion for missing companions due to observational biases shows that the CSF of AB-stars is compatible with values ≥ 0.41. This agrees well with measurements on TTauri stars and G-type stars in other star forming regions. However there is evidence that we underestimate the true CSF.

No multiple systems of higher degree are detected for this sample.The distribution of brightnesses and mass ratios both compare well with the literature. The mass function of the companions is potentially slightly top-heavy but still in agreement with the Salpeter IMF.

The (uncorrected) CSF for the massive subsample including spectroscopic binaries found in the literature was measured to number 69±9%. A completion for missing companions due to observational biases shows that the CSF of massive stars is compatible with values ≥ 1.21. This value compares well with values detected for massive stars in different star forming regions especially Orion. The degree of multiplicity of 1.4-1.5 of our OB-sample also compares well to the ratios found in Orion and differs significantly from the values found in other star forming regions.

The mass function of the companion stars fits well with a MF with slope Γ= -0.15. This can explain the findings of a flattened mass function with a slope of Γ =-0.6 to -0.8 in the center of young galactic clusters.

The distribution of separations of the massive sample increases toward our lower detection limit of $0\farcs08$ and shows a weak maximum at $1\farcs6$. This increase toward lower separations compares well to the findings in most other star forming regions. In Scorpio A Brandner et al. (1998) find an additional peak of the distribution as we do for the OB-star sample but at the closer separation of 350 AU ($0\farcs4$ at the distance of Cep OB2/3).

The distribution of mass ratios is peaked around 0.45 and compares well to other star forming regions. For the wider sample we detect an overabundance of low mass ratios (around 0.1).

This compares well with the findings in NGC6611 (Duchene et al. 2001) and ρ-Oph (Ratzka et al. 2005).

More than 60% of the companions of this massive sample have a cbrightness contrast to the primary of ≤ 1.7 mag. Thes massive companions apparently have four regions where they reside: spectroscopic, around a separation of 80 AU, 400 AU and 1600 AU. These different regions seem not to result from projection effects. This observation needs to be further confirmed and if so will be a challenge to any model of massive star formation. A possible explanation is that the wide companions reside on highly eccentric orbits. This is confirmed by the fact that they are to about 50% members of real or suspected triple systems. It would be interesting to re-observe these targets with larger telescopes and interferometers to possibly detect these close companions. Additionally an observation with GAIA at least for the companions with intermediate separation ($\approx 0\overset{''}{.}8$) could test the hypothesis of eccentricity.

The findings confirm that massive stars tend to form in multiple systems. Dynamical interactions play an important role during the formation.

The correlations between system mass, binary separation mass ratio, and between primary and secondary mass all agree well with a scenario of the formation of a close binary via accretion onto an originally wide one. A scenario of fragmentation of the pre-stellar core to explaine the data needs a fine-tuning of the correlation between core mass and density gradient, and is less favorable. A survey of pre-stellar cores with ALMA can test this correlation. All the correlations found agree well with the data found in Scorpius OB2 by Kouwenhoven et al. (2007). This implies that the mechanism of binary formation is universal at least for OB-associations.

So we conclude that a coalescence scenario can explaine our data of the intermediate-mass and massive stars best. However, a proper motion study of the region indicates that the stellar density in our region has never been high enough for a coalescence scenario to work on a global scale. Thus, it seems that the reason for the multiplicity of the stars is intrinsic to their formation and a local effect i.e. does not depend on the properties of the surrounding cluster or association.

So for the formation of multiple systems in the Cep OB2/3 associations we favor a scenario where the pre-stellar core fragments into a few parts only and the fragments undergo an evolution determined by a coalescence scenario. The number of fragments rises with the core mass from two for istars with spectral types later than B2V to three or more for more massive stars.

Chapter 15

Summary of the Thesis

In this work we aimed to constrain the formation mechanism of massive stars. The two scenarios of massive star formation, i.e. the modified accretion scenario and the coalescence scenario were tested by observations of massive and intermediate-mass stars in the Cep OB2/3 associations looking for companions.

To gain sufficient angular resolution to perform this task the pyramid infrared wavefront sensor PYRAMIR has been developed. This system, mounted on the 3.5m telescope of the Centro Astronómico Hispano Alemán on Calar Alto, can measure the wavefront aberrations in J, H, and K band with a frame rate up to 300 Hz. From a series of laboratory measurements we tested the response of the system under various conditions. This test lead to the construction of a model of the on-sky performance of the system.

This model was verified in a series of on-sky measurements under various conditions. The system was running even under bad sky conditions. Under good atmospheric conditions (seeing in K $0\farcs6$, wind speed $4ms^{-1}$) PYRAMIR can achieve Strehl ratios of $\geq$ 60% . We found a good agreement between our model, observations, and theory.

A comparison of the model, extrapolated to an 8m class telescope, with NACO showed a superiority of the Pyramid wavefront sensor over the Shack-Hartmann sensor for Signal to noise ratios between $\approx$ 2 and $\approx$ 4. We further extrapolated the model to the regime of ELTs to use the sensor as an auxiliary wavefront sensor for a laser guide star AO-system. Here the auxiliary wavefront sensor measures the first 7 radial orders using a natural guide star and the laser radial order 8 to 41. For this setup the pyramid sensor showed a gain of 0.7 mag in the regime of signal to noise mentioned above.

Due to peculiarities of the system the sensor could unfortunately not be used during the observational campaign. Instead we observed 148 targets in z' band in the Cep OB2/3 associations with the Lucky Imaging camera AstraLux mounted on the 2.2m telescope on Calar Alto. The angular resolution of $0\farcs08$ leads to a physical resolution of 64 AU at the distance of the associations (800 pc).

Physical companions were determined by a probability argument. The sample was divided at a mass of $\approx$ 10 $M_\odot$ into massive and intermediate-mass stars. For both samples various binary parameters were derived. The raw companion star fraction of the two samples was significantly different 17±6% and 39±9% for the intermediate-mass sample and the massive sample respectively. A completion of the samples for observational biases lead to a CSF of $\geq$41% and $\geq$ 121% for the two samples. For the massive stars we find a large fraction of triple or quadruple systems whereas the intermediate-mass systems seem to be purely binary stars.

This finding confirms a similar detection by Preibisch et al.(1999) in Orion. They detected a border around spectral type B3 where the multiplicity properties dramatically change.

The distribution of separations of the companions suggests that there exist 4 regimes of separations where massive companions lurk, one at a few AU (spectroscopic companions), one around a separation of $\leq$ 80 AU, around a separation of $\approx$ 640 AU and a separation of $\approx$ 1600 AU. A confirmation of this finding will strongly constrain any theory of massive star formation. The companions at wide separations are suspected to have highly eccentric orbits. If so this hints to undetected close companions. Indeed about 1/3 of these systems have a known third companion. Future observations of these companions with GAIA will reveal the orbital parameters. Observations with higher angular resolution than ours, i.e. with AO on an 8m class telescope or with interferometry, might lead to the detection of the suspected companions.

The accumulation of companions toward separations $\leq$ 80 AU is consistent with findings in other star forming regions. Also a distribution with an additional peak at larger separations exists in the region of Upper Scorpius (Brandner et al. 1998). However, this peak is at closer separations (350 AU) than ours of 1600 AU. They explain the existence of this second peak with the absence of massive stars in the region of the sample that of course cannot applied in our case. The binary parameters derived from our data favor a formation scenario of multiple systems (for both intermediate-mass stars, as well as massive stars) by local coalescence i.e. a fragmentation of a pre-stellar core and a further evolution according to a coalescence scenario.

Appendix A

Target List

The following table contains all targets we observed. The different columns contain the following parameters: Column 1 the name of the target. Most names are either from the Henry Draper Catalog, the 'Bonner Durchmusterung' or from Sicilia-Aguilar(2007). Column 2 and 3 give the right ascension and declination with equinox 2000. Column 4 shows the spectral type adapted in this work. in column 5 we list the separation of the companion at a maximum separation of 3". Any companion further out is not shown. The position angle is shown in column 6. Column7 presents the magnitude difference between primary and secondary. The membership of the target to the association is shown in column 8. The spectral types found in the literature are then given in column 9. The footnotes in the table denote the following: 26: Röser & Bastian (1988), 27: Simonson (1968), 28: Garrison (1970), 29: Contreras et al. (2002), 30: Morgan et al. (1955), 31: Blaauw (1959), 32: Garrison (1976), 33: Walborn (1971), 34: Jaschek et al. (1964), 35: Sicilia-Aguilar et al. (2005), 36: Hiltner & Johnson (1956), 37: Melikian et al. (1988), 38: Skiff (2007), 39: Kharchenko (2001), 40: Garmany & Stenzel (1992), 41: Morgan et al. (1953), 42: Mendoza (1958)

Table 1: *Target list of AstraLux Observations*

name	RA(2000)	Dec(2000)	SpT	sep[″]	PA[deg]	q[mag]	Mem	Ref
BHJ5	22 50 36.0	+62 27 48	A0V	0.39	254	2.0	n[31]	A0V[31],B5Ib[34]
BD+57 2355	21 38 29.2	+57 41 23	A4	0.49	256	0.5	y[35]	A4[29],[38],[35]
BD+57 2356	21 38 30.3	+57 46 26	A7	-	-	-	n[29]	A7[29],[38]
BD+57 2362	21 40 17.5	+57 57 19	A1	-	-	-	y[18]	A1[29],[38],[35]
BD+612213	21 53 26.5	+62 35 13	B3V	-	-	-	y[27]	B8[26],B3V+B5V[27]
BD+61 2214	21 53 29.6	+62 35 54	B3V	-	-	-	y[27]	B3V[27],B8[26],B1IV[34],B5V[38]
BD+61 2215	21 53 34.1	+62 35 55	B3V	-	-	-	y[27]	B3V[27],B8[26],B1IV[34]
BD+61 2218	21 54 01.7	+62 37 10	B3V	0.46	94	4.3	y[27]	B3V[27],B1IV[34],B5V[38]
BD+61 2350	22 49 36.4	+62 19 58	B0.5-1V	-	-	-	y[31]	B1V[28],B5[26],B0.5V[34],B0.5-1V[31]
BD+61 2353	22 50 09.7	+61 56 53	A2IV	-	-	-	n[31]	A2IV[28],A5[26],B8-A0[31],[38]
BD+61 2355	22 52 29.2	+62 41 10	B7IV	0.35	127	3.0	n[28]	B7IV[28],B8[26],B8III/A0[34],B7[31]
				0.89	355	3.11		
BD +61 2357	22 52 33.7	+62 18 48	B0.5-1V	0.09?	44?	1.4?	y[28]	B1V[28],B8[26],B0.5V[34],B2[31]
BD+61 2365	22 54 18.0	+62 39 55	B0.5-1V	-	-	-	y[28]	B1V[28],B5[26],B0.5V/B0[34],B1[31]
BD+61 2366	22 54 36.4	+62 36 45	B0.5-1V	-	-	-	y[28]	B1V[28],B5[26],B0.5V/B0[34],B1[31]
BD+61 2369	22 55 34.1	+62 20 10	B9V	-	-	-	n[28]	A1V[28],A0[26],[31],B9V/A0[34]
BD+61 2380	22 59 22.3	+61 58 23	B9V	-	-	-	n[28]	B9V[28] ,A0[26],B9/A0[31]
BD+61 2382	23 01 29.4	+62 05 22	A1V	-	-	-	n[28]	A1V[28],A0[26]
BD+61 2396	23 07 56.2	+62 39 33	A1V	-	-	-	n[28]	A1V[28] ,A0[26],[31]
BD+61 2397	23 08 10.0	+62 35 57	B9.5V	0.16	9.4	0.4	n[28]	B9.5V[28],A0[26],B9/A0[31]
BD+62 2078	22 25 33.6	+63 25 03	O7-7.5V	2.1	101	4.2	y[40]	O7[27],[34],[38]
BD+62 2125	22 52 50.2	+63 24 48	B1-1.5V	0.1	22	1.3	y[28]	B1.5V[28],B5[26],B1V[34]
				2.0	91	6.6		
BD+62 2127	22 53 41.4	+63 25 05	B2IV-V	0.08?	15?	2.0?	y[40]	B2IV-V[28],B1V[34]
				0.77	193	2.7		
BD+62 2133	22 55 53.0	+62 50 12	A1V	-	-	-	n[28]	A1V[28],B8[26],B8V[34],A0[31]
BD+62 2136A	22 56 36.0	+62 52 00	B0.5V	1.89	347	0.1	y[31]	B0.5Vn[31],B0V[34],[32]
BD+62 2137	22 56 32.9	+63 14 31	A7V	-	-	-	n[28]	A7V[28],A2[26]
BD+62 2142	22 58 03.9	+63 21 45	B3V	-	-	-	y[28]	B8[26],[39],B3V[28],[34],[31]

Table 2: *Target list of AstraLux Observations cont.*

name	RA(2000)	Dec(2000)	SpT	sep[″]	PA[deg]	q[mag]	Mem	Ref
BD +62 2148	22 58 44.9	+63 10 09	A0V	-	-	-	n[28]	A0V[28]
BD +62 2151	22 59 14.9	+62 48 42	B8V	-	-	-	n[28]	A2p[28],B8V[34],A0[31]
BD +62 2153	22 58 44.9	+63 10 09	A0V	-	-	-	n[28]	B9.5V[28],B9V-A0V[34],[31]
BD +62 2154	23 00 32.2	+63 30 59	B1V	-	-	-	y[28]	B1V[28],[34],B5[26],B1V/B7[31]
BD+62 2155	23 00 54.6	+62 52 54	B2IV	1.69	342	1.15	y[28]	B2IV[28],B2[31]
BD +62 2158	23 02 12.8	+62 49 33	B9V	-	-	-	n[28]	B9V[28] ,A0/B9[31]
BD+62 2166	23 04 45.4	+63 21 05	B1V	2.46	17	1.9	y[28]	B1V[28],[34],B5[26],B1V-B2[31]
BD+63 1889	22 48 50.3	+63 45 15	B8III	-	-	-	n[28]	A0III[28],B8III[34],B9[31]
BD+63 1911	22 59 40.5	+63 48 04	B5V	-	-	-	n[28]	A7V[28],B5V[34],A0[31]
Cl* NGC 7160 DG 382	21 51 31.4	+62 28 46	A6.5	-	-	-	pm[35]	A6.5[35]
Cl* NGC 7160 DG 39	21 53 27.8	+62 35 19	A0	-	-	-	y[35]	A0[35]
Cl* NGC 7160 DG 398	21 51 42.3	+62 33 15	A6	-	-	-	y[35]	A6[35]
Cl* NGC 7160 DG 409	21 51 45.7	+62 42 58	A5.5	-	-	-	y[35]	A5.5[35]
Cl* NGC 7160 DG 42	21 53 36.8	+62 32 49	A6	-	-	-	y[35]	A6[35],A5V[38]
Cl* NGC 7160 DG 45	21 53 45.5	+62 40 57	A3	1.64	169	4.2	y[35]	A3[35],[38]
Cl* NGC 7160 DG 460	21 52 11.5	+62 38 46	A0	-	-	-	y[35]	A0[35]
Cl* NGC 7160 DG 47	21 53 55.6	+62 36 18	A5	-	-	-	y[35]	A5[35]
Cl* NGC 7160 DG 481	21 52 21.1	+62 45 03	A7	-	-	-	y[35]	A7[35]
Cl* NGC 7160 DG 49	21 53 51.9	+62 33 25	A8	-	-	-	y[35]	A8[35],A7V[38]
Cl* NGC 7160 DG 526	21 52 38.6	+62 45 52	A7	-	-	-	y[35]	A7[35]
Cl* NGC 7160 DG 529	21 52 39.3	+62 44 49	A2	-	-	-	pm[35]	A2[35]
Cl* NGC 7160 DG 531	21 52 39.3	+62 46 58	A8	-	-	-	pm[35]	A8[35]
Cl* NGC 7160 DG 65	21 54 36.8	+62 34 00	A7	2.6	15	5.8	pm[35]	A7[35]
Cl* NGC 7160 DG 67	21 52 59.8	+62 42 06	A4	-	-	-	y[35]	A4[35]
Cl* NGC 7160 DG 682	21 53 45.1	+62 36 55	A2	1.21	291	3.6	y[35]	A2[35]
Cl* NGC 7160 DG 685	21 53 45.4	+62 45 25	A6.5	-	-	-	y[35]	A6.5[35]
Cl* NGC 7160 DG 687	21 53 46.2	+62 46 35	A5	-	-	-	y[35]	A5[35]
Cl* NGC 7160 DG 720	21 54 02.9	+62 26 35	A0	-	-	-	y[35]	A0[35]
Cl* NGC 7160 DG 725	21 54 05.4	+62 43 43	A8.5	-	-	-	y[35]	A8.5[35]
Cl* NGC 7160 DG 794	21 54 33.5	+62 47 53	A8	-	-	-	y[35]	A8[35]

Table 3: *Target list of AstraLux Observations cont.*

name	RA(2000)	Dec(2000)	SpT	sep[″]	PA[deg]	q[mag]	Mem	Ref
Cl* NGC 7160 DG 853	21 55 07.1	+62 43 34	A2.5	-	-	-	y[35]	A2.5[35]
Cl* NGC 7160 DG 899	21 55 38.4	+62 45 53	A9	-	-	-	y[35]	A9[35]
Cl* NGC 7160 DG 907	21 55 43.1	+62 42 29	A7	-	-	-	y[35]	A7[35]
Cl* NGC 7160 DG 920	21 55 54.9	+62 44 34	A4.5	-	-	-	y[35]	A4.5[35]
Cl* NGC 7160 DG 934	21 56 03.6	+62 38 55	A2.5	-	-	-	y[35]	A2.5[35]
Cl* NGC 7160 DG 946	21 56 10.8	+62 34 55	A5.5	-	-	-	pm[35]	A5.5[35],A5[26]
HD198895	20 51 10.0	+55 29 19	B1-2Ve	-	-	-	pm[41]	B1V[27],[30],[39]
HD199308	20 53 52.2	+56 21 47	B1.5-2IV-V	-	-	-	pn[27]	B2V[27],B3[26],B2IV-V[33],B1.5V[38]
HD199661	20 56 17.0	+56 53 15	B2.5-3IV	-	-	-	pn[27]	B3V[27],B3[26],[38],B2.5IV[39]
HD200857	21 03 52.9	+55 13 49	B3III/B2II	-	-	-	pm[41]	B3III[41],B2[26],B3III[34],[27],[30],B2II[38]
HD203025	21 17 18.8	+58 36 41	B2III	0.08	271	0.6	pm[41]	B2V[27],B3[26],[38],B2III[34],[30]
HD203374	21 19 07.4	+61 51 30	B0IV	0.3	298	1.5	y[40]	B0V[27],B0[26],B0IV[34],[30],B0[38]
HD204116	21 24 30.3	+55 22 00	B1Ve	-	-	-	pm[41]	B1V[27],[34],[30],B0[26],[38],B1.5IV[33]
HD204150	21 24 14.1	+60 47 50	B2V	-	-	-	pm[27]	B2V[27],[38],B3[26]
HD204827	21 28 57.8	+58 44 23	O9.5-B0V	0.09	180	0.9	y[40]	B0V[27],[34],[30],B3[26],O9.5V[32],B4III[38]
HD205139	21 30 59.3	+60 27 34	B1II	-	-	-	y[40]	B1II[27],[34],[30],B0[26],B1.5V[32],B1[38]
HD205196	21 31 38.4	+57 30 09	B0Ib	-	-	-	y[40]	B0Ib[27],[34],[30],[32],B0[26],B0Ia[38]
HD205329	21 32 20.7	+59 34 21	B5V	0.11	12	1.1	pm[27]	B4[27],B8[26],B1.5V[39],B5[38]
HD205510	21 33 41.7	+58 11 45	A3p	-	-	-	pn[27]	B3V[27] A3p[34],A2[26],A3[38]
HD205686	21 34 32.3	+62 18 28	B0.5V	-	-	-	pm[27]	B1.5[27],B9[26],B0.5V[38]
HD206183	21 38 42.0	+56 58 14	B0-O9.5V	-	-	-	y[40]	B0V[27],[30],B9[26],O9-B0V[34],O9.5V[32],B0[38]
HD206267	21 38 57.6	+57 29 21	O6	0.11	225	1.2	y[40]	O6[27],[36],[29],[38],O5[26],O6V[32]
				1.74	320	6.3		
HD206773	21 42 24.2	+57 44 10	B0V:pe	-	-	-	y[40]	B1V[27],A2[26],B0V:pe[34],B0V[30],[32],B0e[38]
HD207198	21 44 53.3	+62 27 38	O9IIe	-	-	-	y[40]	O9.5II[27],B0[26],O9II[34],[30],OI[38],O9.5Ib-II[40]
HD207538	21 47 39.8	+59 42 01	B0-O9V	0.07	194	2.1	y[40]	B0V[27],[34],[30],[38],B2[26],O9.5V[32]
HD207951	21 50 40.6	+61 48 11	B2V	-	-	-	y[40]	B2V[27],B8[26],B2[38]
HD208095	21 52 01.0	+55 47 48	B6IV-V	-	-	-	pn[27]	B3[26],B8V+A0[27],B6IV-V[38]
HD208106	21 51 47.6	+61 56 34	B2-3V	-	-	-	pn[27]	B3V[27],B3[26],B2V[33],[38]
HD208392	21 53 48.1	+62 36 52	B0.5-1V	0.1	212	1.4	y[35],[40]	B1V[27],B3[26],[38],B1IV[34],[30],B0[42]

Table 4: *Target list of AstraLux Observations cont.*

name	RA(2000)	Dec(2000)	SpT	sep[″]	PA[deg]	q[mag]	Mem	Ref
HD208761	21 56 16.0	+62 53 41	B3V	-	-	-	y[27]	B3V[27],B3[26],B2III[38]
HD208905	21 57 17.7	+61 17 43	B1-2V	0.42	170	0.6	y[40]	B1V[27],[38],B3[26]
HD209339	22 00 39.3	+62 29 16	B0IV	0.97	224	2.5	y[40]	B0IV[27],[34],B0[26],B1[38]
HD209481	22 02 04.6	+58 00 01	O9V	-	-	-	y[40]	O9V[27],[30],[40],B0[26],O9[34],B2[38]
HD209744	22 03 53.9	+59 48 52	B1-2V	0.3	242	2.5	pm[41]	B1V[27],[34],B5[26],B2II/V[38]
HD209975	22 05 08.8	+62 16 47	O9Ib	-	-	-	y[40]	O9.5b[27],O5[26],O9/O9.5IB[34],O9/B0,[38]
HD210386	22 08 00.3	+63 44 08	B1.5II-III	-	-	-	pm[27]	B5[26],B1[27],B1.5II-III[33],[38]
HD210478	22 08 45.6	+61 01 21	B1-2V	-	-	-	pm[27]	B1V[27],[34],[30],B8[26],B2[38]
HD210839	22 11 30.6	+59 24 52	O6Iab	-	-	-	y[40]	O6f[27],[34],[30],[38],O4[26]
HD211880	22 18 27.8	+63 13 22	B0.5V	-	-	-	pm[27]	B0.5V[27],[34],[30],[38],B8[26]
HD213023	22 26 52.4	+63 43 05	O9V	1.74	345	0.5	y[40]	B2[26],O9V[34],[30],[38],B3[27]
HD216532	22 52 30.6	+62 26 26	O8-8.5V	-	-	-	y[28]	O8V[28],B3[26],O8[34],[30],[31],O8.5V[33],[40]
HD216629	22 53 15.6	+62 08 45	B2-3IV-V	-	-	-	y[28]	B2IV-V[28],B2,B0[34],B2[31],B3e[38]
HD216658	22 53 30.8	+62 08 06	B0-0.5V	0.71	60	3.1	y[28]	B0V[27],[34],[30],[38],B0.5V[28],B0V/B1[31]
HD216711	22 53 54.0	+62 35 48	B1V	0.76	41	3.5	y[28]	B1V[28],[34],[30],B5[26],B1V/B0[31],B4V[38]
				1.00	194	3.6		
HD216926	22 55 52.6	+63 28 23	B9III	-	-	-	n[28]	B9V[28],A0[26],[31],B9III[34]
HD217061	22 56 42.6	+62 37 30	B1Vn	0.08	324	0.0	y[28]	B1Vn[28],B1V[34],[30],[31],[38]
HD217086	22 56 47.2	+62 43 38	O7V	2.84	355	4.2	y[40]	O7V[28],[33],B0[26],O5-7/O6[30],O5/O7/B0[31],O7[38]
HD217174	22 57 32.9	+62 21 28	A1V	0.98	290	1.5	n[31]	A2[26],[39],A0[31]
HD217297	22 58 33.3	+63 42 24	B1.5V	0.16	284	1.9	y[28]	B1.5V[28],[30],B5[26],B1-1.5V[34],B1V/B0[31],B2II[38]
HD217463	22 59 42.9	+62 46 38	B1.5-2V	0.55	14	1.5	y[28]	B1.5V[28],[33],[38],B2[26],[31],B2V[34]
HD217966	23 03 21.1	+62 38 33	B7V	0.78	243	5.8	n[28]	B7V[28],A0[26],B8-A0/B7[31]
HD218066	23 04 02.2	+63 23 49	B0-1V	0.46	246	1.6	y[28]	B1.5V[28],B5[26],B1V[30],[38],B1V/B3[31]
HD218229	23 05 21.3	+62 21 19	B8III	-	-	-	n[28]	B8III[28],B8[26],B8-A0[31],B9II-III[38]
HD218450	23 07 13.2	+62 40 37	B9Vn	-	-	-	n[28]	B9Vn[28],A0[26],[31]
HD218537	23 07 47.8	+63 38 00	B3V	0.2	320	0.5	n[31]	B2.5V[28],B3[26],[31],[38]
HD239581	21 08 27.7	+56 02 43	B2V	0.15	343	3.3	pn[27]	B2V[27]
HD239595	21 10 57.7	+60 13 16	B8	-	-	-	pm[27]	B8[26],[38]
HD239618	21 14 45.5	+59 45 40	B2Ve	-	-	-	pn[27]	B2Ve[27],[38],B0[26]

Table 5: *Target list of AstraLux Observations cont.*

name	RA(2000)	Dec(2000)	SpT	sep	PA[deg]	q[mag]	Mem	Ref
HD239626	21 17 33.5	+60 06 02	B0V	-	-	-	pn^{27}	B0V^{27},B0^{26},B0.5^{38}
HD239649	21 23 34.6	+59 51 05	B3	0.45	328	4.2	y^{40}	B2V^{40},B3^{26},B8^{38}
HD239671	21 27 13.4	+56 12 30	B2V	-	-	-	pm^{27}	B2V^{27},B0^{26}
HD239675	21 27 17.0	+59 53 30	B5	0.32	54	1.4	y^{27}	B3V^{27},B5^{26},B8^{38}
HD239676	21 27 32.6	+59 17 41	B2V	-	-	-	y^{40}	B1V^{40},B2^{26},B5^{38}
HD239681	21 28 26.8	+60 14 56	B1II	-	-	-	y^{40}	B0V^{40},B5^{26},^{38}
HD239683	21 29 53.5	+57 48 57	B3IV	-	-	-	pm^{27}	B3IV^{32},B5^{26},^{38}
HD239689	21 30 45.9	+57 12 00	B1.5-2V	-	-	-	pn^{27}	B2^{26},B1.5V^{39}
HD239693	21 31 25.9	+57 53 57	B3V	-	-	-	y^{27}	B3V^{27},B3^{26},B5^{38}
HD239710	21 36 41.0	+57 30 08	B3V	-	-	-	y^{40}	B2.5IV^{40},^{32},B3V^{27},B3^{26},B5^{38}
HD239742	21 42 52.1	+57 01 01	B2-3V	-	-	-	pn^{27}	B3^{26},B5^{38},B2V^{39}
HD239758	21 44 34.0	+59 03 26	B2III:nn	-	-	-	y^{40}	B2V^{40},^{27},B0^{26},B2III^{34},B5ne^{38}
HD239767	21 46 22.6	+56 55 02	B0.5V	-	-	-	y^{40}	B0.5V^{40},^{27},^{34},B0^{26}
HD239789	21 53 05.1	+58 21 37	B2	-	-	-	pm^{27}	B2^{26}
Cl* Trumpler 37 KUN 197	21 40 15.2	+57 37 16	A2	-	-	-	pm^{29}	A2^{29},F2^{38}
Cl* Trumpler 37 KUN 318	21 37 26.0	+57 36 02	A1	-	-	-	pm^{29}	A1^{29},^{38}
Cl* Trumpler 37 KUN 89	21 39 46.2	+57 26 10	A8	-	-	-	pm^{29}	A8^{29},F5^{38}
Cl* Trumpler 37 MVA 164	21 37 20.1	+57 25 14	A3	-	-	-	y^{35}	A3^{29},^{38}
Cl* Trumpler 37 MVA 169	21 37 24.0	+57 28 17	A4	-	-	-	y^{35}	A4^{29},A2^{38}
Cl* Trumpler 37 MVA 224e	21 38 01.0	+57 38 07	A7	1.53	118	4.1	pm^{35}	A7^{29},^{38}
Cl* Trumpler 37 MVA 258	21 37 56.1	+57 42 21	A2	-	-	-	pm^{35}	A2^{29},^{38}
Cl* Trumpler 37 MVA 463	21 39 12.0	+57 29 57	A0	-	-	-	pm^{35}	A0^{29},^{38}
Cl* Trumpler 37 MVA 472	21 38 19.2	+57 31 57	A8	-	-	-	pm^{35}	A8^{29},^{38}
Cl* Trumpler 37 MVA 497	21 39 22.3	+57 31 49	A1	1.24	42	3.1	y^{35}	A1^{29},^{38}
Cl* Trumpler 37 MVA 545	21 38 17.2	+57 40 02	A7	-	-	-	y^{35}	A7^{29},^{38}
Cl* Trumpler 37 MVA 564	21 39 07.9	+57 42 09	A9	1.39	218	6.0	y^{35}	A9^{29},^{38}
Cl* Trumpler 37 MVA 566	21 39 18.9	+57 42 29	A1	-	-	-	y^{35}	A1^{29},^{38}
Cl* Trumpler 37 MVA 640	21 39 46.7	+57 32 53	A7	-	-	-	y^{35}	A7^{29},^{38}
Cl* Trumpler 37 MVA 660	21 39 40.9	+57 35 09	A2	-	-	-	y^{35}	A2^{29},^{38}
Cl* Trumpler 37 MVA 81	21 36 23.8	+57 38 05	A0	0.44	191	1.2	y^{35}	A0^{29},^{38}

Table 6: *Target list of AstraLux Observations cont.*

name	RA(2000)	Dec(2000)	SpT	sep[″]	PA[deg]	q[mag]	Mem	Ref
Cl* IC 1396 SBZ 2-46	21 37 18.4	+57 31 21	A0	0.81	76	1.1	y[35]	A0[29],[38]
Cl Trumpler 37 185	21 40 30.4	+57 13 26	A1	0.08	15	0.7	pm[29]	A1[29],[38]
TYC 4282-488-1	22 55 17.4	+62 41 07	B9-A0V	-	-	-	n[28]	A0V[28],B9V[34],[31]
V374 Cep	23 05 07.5	+62 15 37	B2-3Ve	-	-	-		B2-3[37],[38]

Bibliography

Abraham et al. 1993, A& A, 268, 230
Abt, H.A. et al. 1990, ApJS, 74, 551
Abt, H.A. & Levy, S.G. 1976, BAAS, 8, 521
Alves, J. et al. 2007, A&A, 462, 17
Apai, D. et al. 2007, ApJ, 655, 484
Assousa, G.E. et al. 1977, ApJ, 218, 13
Babcock, H.W. 1953, PASP, 65, 229
Bacmann, A. et al. 2000, A&A, 361, 555
Baines, D. et al. 2006, MNRAS, 367,737
Balazs, L.G. & Kun, M. 1989, Astronomische Nachrichten, 310, 385
Bate, M.R. 2000, MNRAS, 314, 33
Bate, M.R. et al. 2002, MNRAS, 336, 705
Batten, A.H. et al. 1978, Publ. Dom. Astrophys. Obs., 15, 121
Beuther, H. & Schilke, P. 2004, Sci, 303, 1167
Blaauw, A. et al. 1959, AJ, 130, 69
Blaauw, A. 1964, ARA& A 1964, 2, 213
Blaauw, A. 1991, psfe.conf., NATO ASI Series C, 342, 125
Bodenheimer, P. & Burkert, A. 2001, IAUS, 200, 346
Bonnell, I.A. et al. 1998, MNRAS, 298, 93
Bonnell, I.A. et al. 2005, MNRAS 362, 915
Bonnell ,I.A. 2008, ASPC, 390, 26
Brandner et al. 1996, A& A 307, 121
Brandner, W. & Koehler, R. 1998, ApJ, 499, L79
Brandner, W. et al. 2002, The Messenger, 107, 1
Brown, A.G.A. et al. 1997, MNRAS, 285, 479
Burvall, A. et al. 2006, OPEX, 14, 11925
Campbell, H.I. & Greenaway, A.H. 2006, EASP, 22, 165
Caselli, P. & Myers, P.C. 1995, ApJ, 446, 665
Clarke, C. J. 2001, IAUS, 200, 346
Clenet, Y., 2004 , SPIE, 5490, 107
Cochren, W.D. & Hatzres, A.P. 1996, Ap&SS, 241, 43
Comeron, F. et al. 2006, A& A, 457, 553
Conan, J.-M. et al. 1995, JOSA, 12, 1559
Contreras, M.E. et al. 2002, AJ, 124, 1585
Costa, J. 2003, PhD thesis, Ruprecht-Karls-Universiät, Heidelberg
deVegt, C. 1966, ZA, 64, 268
Dierickx, P. 2001, ESO Conf. Proc., 58, 65
Dommanget, J. & Nys, O., 2002, Observations et Travaux 54, 5 (Vizier online Catalogue I/274)
Doremus, C. 1970, PASP, 82, 745
Dorner, B. 2006, Diploma thesis, Ruprecht-Karls-Universiät, Heidelberg
Duchene, G. et al. 2001, A& A, 379, 147
Duquennoy, A. & Mayor, M. 1991, A& A, 248, 484
Elmegreen, B.G. & Lada, C.J., ApJ, 214, 725

Esposito, S. & Riccardi, A. 2001, AAP, 369, L9
Fabricius, C. et al. 2002, A& A, 384, 180 (Vizier online Catalogue I/276)
Figer, D.F. et al. 1999, ASPC, 186, 329
Fischer, D.A., Marcy, G.W. 1992, ApJ, 396, 178
Fried, D.L. 1966, JOSA, 56, 1372
Fried, D.L., 1990, JOSA A, 7, 1224
Garmany, C.D. 1973 AJ, 78, 185
Garmany, C.D. & Stenzel, R.E. 1992, AAS, 94, 211
Garrison, R.F. 1970, AJ, 75, 1001 and 1081
Garrison, R.F. & Kormendy, J. 1976, PASP, 88, 865
Ghedina, A. et al. 2003, SPIE, 4839, 869
Ghez, A.M. et al. 1997, ApJ, 481, 378
Gies, D.R. 2003, IAUS, 212, 91
Greenwood, D.P. 1977, JOSA, 67, 390
Guyon, O. et al. 2008, PASP, 120, 655
Hardy, J.W. et al. 1977, JOSA, 67, 360
Hardy, J.W. 1998, Oxford University Press, New York
Henry, T.J. & McCarthy, D.W., Jr. 1990, ApJ, 350, 334
Hilditch, R.W. et al. 2005, MNRAS, 357, 304
Hill, G. 1967, APJS, 14, 301
Hillenbrand, L.A. & Hartmann, L.W. 1998, ApJ, 492, 540
Hillwig, T.C. et al. 2006, ApJ, 639, 1069
Hiltner, W.A. & Johnson, H.L. 1956, AJ, 124, 367
Horwitz, B.A. 1994, SPIE, 2201, 496
Jaschek, C. et al. 1964, Serie Astronomica, La Plata (Vizier online Catalogue III/18B)
Jijina, J. & Adams, F.C. 1996, ApJ,462, 874
Jordi, C. et al. 1996, A&A, 312, 499
Kasper, M. 2000, PhD thesis, Ruprecht-Karls-Universiät, Heidelberg
Kharchenko, N.V. 2001, KFNT, 17, 409 (Vizier online Catalogue I/280A/ascc01)
Kirk, J.M. et al. 2005, MNRAS, 360, 1506
Koehler, R. & Leinert, C. 1998, A&A, 331, 977
Koehler R. et al. 2006, A& A, 458, 461
Kolmogorov, A. 1941, Dokl. Akad. Nauk SSSR 30, 301
Kouwenhoven, M.B.N. et al. 2007, A& A, 474, 77
Kratter, K.M.& Matzner, C.D. 2006, MNRAS, 373, 1563
Kraus, S. et al. 2007, A& A, 466, 649
Krumholz, M.R. 2006, astro.ph, 7429
Krumholz, M.R. 2008, ASPC, 390, 16
Krumholz, M.R. & Thompson, T.A. 2007, ApJ, 661, 1034
Larson, R.B. 1981, MNRAS, 194, 809
Launhardt, R. 2004, IAUS 221
Leinert, C. et al. 1993, A&A, 278, 129
Linfoot, E. H. 1948, MNRAS, 108, 428
Mackay, C.D. et al. 2001, SPIE, 4306, 289
Mason, B.D. et al. 1998, AJ, 11, 821

Mayor, M. et al. 1992, ASPC,32, 73
McAlister, H.A. 2007, IAU, 240, 35
McKee, C.F. and Tan, J.F. 2002, Nature, 416, 59
McKee, C.F. and Tan, J.F. 2003, ApJ, 585, 850
Meader, A. & Behrend, R. 2002, ASPC, 267, 179
Melikian, N.D. et al. 1988, IBVS, 3187, 1
Mendoza, V. 1958, ApJ, 128, 207
Moeckel, N. & Bally, J. 2007, ApJ, 656, 275
Moreno-Corral, M.A. et al. 1993, A&A, 273, 619
Morgan, W.W. et al. 1953, ApJ, 118, 318
Morgan, W.W. et al. , ApJS, 2, 41
Nakano, T. et al. 2000, ApJ, 534, 976
Nelan, E. et al. 2004, AJ, 128, 323
Oudmaijer, R.D. et al. 2006, ASPC, 355, 99
Patel, N.A. et al. 1994, ASPC, 65, 81
Patel, N.A. et al. 1995, AJ, 447, 721
Patel, N.A. et al. 1998, ApJ, 507, 241
Perryman, M. A. C., ESA SP Series vol no: 1200, Noordwijk
Peter, D. et al. 2006, SPIE, 6272, 67
Peter, D. et al. 2008, PASP(in press)
Portegies Zwart, S.F. et al. 2002, ApJ, 565, 265
Pourbaix, D. et al. 2004, A& A, 424, 727 (Vizier online Catalogue B/sb9)
Preibisch, Th. et al. 1999, New Astronomy, 7, 531
Pugh, W.N. et al. 1995, SPIE, 2534, 312
Ragazzoni, R. 1996, J.Mod.Opt. 43, 289
Ragazzoni, R. et al. 1999, AAP, 350, L23
Ratzka, T. et al. 2005, A&A, 437, 611
Rigaut,F. & Gendron E. 1992, A&A, 261, 677
Roberts, L.C. Jr et al. 2007, AJ, 133, 545
Roddier, N. 1990, SPIE, 1237, 668
Roddier, F. 1999, Cambridge University Press
Röser, S. & Bastian, U. 1988 A& AS, 74, 449 (Vizier online Catalogue I/146)
Samus, N.N. et al. 2004, yCat, 2250, 0S (Vizier online Catalogue II/250)
Sana, H. et al. 2007, arXiv 0707.2847
Sargent, A.I. 1979, ApJ, 233, 163
Schertl, D. et al. 2003, A& A, 402, 267
Shu, F.H. et al. 1987, ARA&A, 25, 23
Sicilia-Aguilar, A. et al. 2004, AJ, 128, 805
Sicilia-Aguilar, A. et al. 2005, AJ, 130, 188 (Vizier online Catalogue J/AJ/130/188/table5)
Simonson, S.C.,III 1968, APJ, 154, 923
Simonson, S.C.,III & van Someren Greve, H.W. 1976, A& A, 49, 343
Skiff, B.A. 2007, yCat2277, 0, (Vizier online Catalogue B/mk)
Smith, J.A. et al. 2002, AJ, 123, 2121
Stickland, D.J. 1995, The Observatory, 115, 180
Stolte, A. et al. 2002, A&A, 394, 459

Straizys, V. 1992, Pachart Publishing House, Tucson
Tokovinin, A.A. 1992, A&A, 256, 121
Trullols, E. et al. 1997, ESA SP, 402, 299
Turner, N. et al. 2008, arXiv0805.3162
Verinaud, C. 2004, Opt.Comm., 233, 27
Walborn 1971, ApJS, 23, 257
Wilson, R.G. 1975, AO, 14, 2286
Wolfire, M.G. & Cassinelli, J.P. 1987, ApJ, 319, 850
Yorke, H.W. & Bodenheimer, P. 1999, ApJ, 525, 330
Yorke, H.W. & Sonnhalter, C. 2002, ApJ, 569, 846
Yorke, H.W. 2002, ASPC, 267, 165
Zinnecker, H. & Yorke, H.W. 2007, ARA&A, 45, 481

Acknowledgements

During the work on this thesis i had help and support of many people.
Especially I want to thank:

Prof. Dr. Thomas Henning for the opportunity to work on this project

Markus Feldt for supervision, support, and fruitful discussions

Sebastian Egner, for explaining AO-systems so well

Stefan Hippler, for his help during the PYRAMIR project, and his comments on the thesis

Wolfgang Gässler, for helping with advice and good ideas

Bernhard Dorner for a good time during the PYRAMIR runs

Miwa Goto for helping me to see things from a different perspective

Christoph Leinert, Hendrik Linz, Dimitrios Gouliermis, Wolfgang Brandner, Ralf Launhardt, Rainer Köhler and Hendrik Beuther for their time to discuss the subject on binarity, pre-stellar cores, and massive star formation

The members of the PYRAMIR team especially Clmens Storz, Peter Bizenberger, Harald Baumeister, Karl 'Sam' Wagner and Udo Neumann for their great support during the PYRAMIR project

Felix Hormuth for spending several nights to observe my target stars in Cepheus

Jesus Aceituno and Luzma Montoya for their support and help during the PYRAMIR runs on the 3.5 m telescope on Calar Alto

The staff of Calar Alto especially Jens Helmling for helping with the ALFA and PYRAMIR setup.

The people from the mechanics and electronics departments for spending time to get PYRAMIR in shape